Graduate School ETD Form 9
(Revised 12/07)

PURDUE UNIVERSITY
GRADUATE SCHOOL
Thesis/Dissertation Acceptance

This is to certify that the thesis/dissertation prepared

By Dionysios Antypas

Entitled

Measurement of a weak transition moment using coherent control

For the degree of Doctor of Philosophy

Is approved by the final examining committee:

Daniel S. Elliott
Chair

Ephraim Fischbach

David D. Nolte

Sergei Savikhin

To the best of my knowledge and as understood by the student in the *Research Integrity and Copyright Disclaimer (Graduate School Form 20)*, this thesis/dissertation adheres to the provisions of Purdue University's "Policy on Integrity in Research" and the use of copyrighted material.

Approved by Major Professor(s): Daniel S. Elliott

Approved by: Andrew S. Hirsch 11/13/2013
Head of the Graduate Program Date

MEASUREMENT OF A WEAK TRANSITION MOMENT USING COHERENT CONTROL

A Dissertation

Submitted to the Faculty

of

Purdue University

by

Dionysios Antypas

In Partial Fulfillment of the

Requirements for the Degree

of

Doctor of Philosophy

December 2013

Purdue University

West Lafayette, Indiana

To my family.

ACKNOWLEDGEMENTS

The people who have contributed either directly or indirectly to the work presented in this Thesis are way too many for me to acknowledge individually. These include (but are not limited to) all of my mentors, my teachers, my Ph.D. committee members, faculty at other Institutions, my fellow graduate students and lab mates, many undergraduates, family members and relatives, friends, and many staff members at Purdue. Here I can only acknowledge a few of them, the ones who – even in a broad sense - have contributed the most.

First, I am grateful to my adviser Dr. Elliott, for his mentorship and support all these years. Aside from being a great mentor, Dr. Elliott is also a very patient adviser. I figured this when I recently realized that he never told me "I am busy right now" on any of my 250 or so un-notified visits to his office. I suspect however that he may have been *a bit* busy at least a few of those times.

Although I worked mostly on my own, I had the chance to interact with the other graduate students in the lab and benefit from their experiences and expertise. John Lorenz, the more senior student in our group, helped me with my first steps in the lab. Adeel Altaf, put together the Raman laser I used in my work. And Sourav Dutta, taught me how to build stable diode lasers, which made data acquisition a very uneventful process. Sourav also assisted with our vacuum chamber design. I thank all of them for their technical contributions as well as for all of our useful (and our fun but least useful) interactions.

As a graduate student I had the privilege (as I now realize) of working with undergraduates, a few of whom have contributed to this Thesis. Of the roughly one dozen that I supervised in various projects, I would like to mention Roger Ding for designing printed circuit boards for my lasers, the extremely patient (with both me and the job) Carlos Vargas who helped with making magnetic field coils, and Andrew Loveless for his Labview programming and electric field simulations.

I owe a big thanks to Tom Miller from PRIME lab, for repeatedly agreeing to leak-test my vacuum chamber and other components of my system. I might have asked Tom for help as many as ten times. His (often amusing) enthusiasm about helping out really tells something about the meaning of voluntary work. I also thank Chuck Harrington, the ECE machinist, for constructing my vacuum chamber and other components of the apparatus, and for all the help and suggestions he provided. Finally, I have to mention Dave Aspell from the ECE instrument shop for "lending" us so many instruments and never reminding us that we have to return them.

I am more than obliged to my uncle, Prof. G.A. Kourouklis and to the late Prof. C. Aliprantis for persuading me to come to the US for a Ph.D., and for all the guidance and support they both provided in order to make this happen. Their instigation has been the start of a wonderful journey.

Last but not least, I thank my family members for their support during my Ph.D. years, as well as for being happy with all of my career decisions (regardless of their implications)!

TABLE OF CONTENTS

Page

Page

ABSTRACT

Antypas, Dionysios. Ph.D., Purdue University, December 2013. Measurement of a weak transition moment using Coherent Control. Major Professor: Daniel S. Elliot.

We have developed a two-pathway Coherent Control technique for measurements of weak optical transition moments. We demonstrate this technique through a measurement of the transition moment of the highly-forbidden magnetic dipole transition between the $6s^2S_{1/2}$ and $7s^2S_{1/2}$ states in atomic Cesium. The experimental principle is based on a two-pathway excitation, using two phase-coherent laser fields, a fundamental field at 1079 nm and its second harmonic at 539.5 nm. The IR field induces a strong two-photon transition, while the 539.5 nm field drives a pair of weak one-photon transitions: a Stark-induced transition of controllable strength as well as the magnetic dipole transition. Observations of the interference between these transitions for different Stark-induced transition amplitudes, allow a measurement of the ratio of the magnetic dipole to the Stark-induced moment. The interference between the transitions is controlled by modulation of the phase-delay between the two optical fields. Our determination of the magnetic dipole moment is at the 0.4% level and in good agreement with previous measurements, and serves as a benchmark for our technique and apparatus. We anticipate that with further improvement of the apparatus detection sensitivity, the demonstrated scheme can be used for measurements of the very weak Parity Violation transition moment on the Cesium $6s^2S_{1/2}\rightarrow 7s^2S_{1/2}$ transition.

1. INTRODUCTION

1.1 Motivation for this work

The use of two-pathway Coherent Control as a means to detect a weak atomic transition was demonstrated in our lab a few years ago [1,2], in an experiment carried out in Cesium, where amplification and detection of the signal of a weak atomic transition was achieved. In that work, a measurement of the weak transition amplitude depended on experimental parameters that are difficult to calibrate, such as laser intensities, optical beam overlap conditions, etc. An extension in the analysis of the experimental principle that followed, suggested that with a proper selection of the experimental conditions, it should be possible to employ the two-Pathway Coherent Control scheme for making measurements of weak transition moment ratios, therefore removing the need for careful calibration of nearly all of the factors involved in measuring a single weak moment. This possibility is of interest to the field of Atomic Parity-Non-Conservation, in which experimenters attempt to measure the amplitude of an extremely weak Parity-Violation transition that occurs between atomic states of the same parity. The measurement is always calibrated against another (known) transition moment. These experiments are never easy and almost always limited in measurement precision by the various systematic contributions to the extremely weak PNC signal. Out of more than a dozen PNC measurements performed to date, using one of two weak signal amplification techniques, only a few have reached the level of precision necessary to test Physics Models. The possibility of making PNC measurements with a new technique, that involves different (and potentially smaller) sensitivities to systematic errors, is a very interesting one.

In the work presented in this thesis, we demonstrate the applicability of the two-pathway Coherent Control scheme for weak transition moment measurements, through a precision measurement of the moment of the highly-forbidden magnetic dipole transition

(M_1) in the Cesium $6S_{1/2}\rightarrow 7S_{1/2}$ transition. The size of the M_1 moment is not as small as the size of a PNC moment, but the project will ultimately be headed towards a PNC measurement, and in this developmental stage of our scheme and apparatus, the M_1 measurement serves as an important intermediate benchmark. We selected to work with the $6S_{1/2}\rightarrow 7S_{1/2}$ transition in Cesium, because our group aims at performing a PNC measurement on the same transition.

1.2 Overview of Parity Non Conservation in atoms

Parity Non Conservation (PNC) experiments in atoms are low energy tabletop experiments, complementary to high energy experiments. They attempt to measure the strength of the weak interaction between the electron and the atomic nucleus, an interaction mediated by the weak neutral boson Z_0 and described by the Standard Model of particles [3]. These measurements are sensitive tests of the Standard Model, as well as tests of potential extensions of the Standard Model. Although the weak interaction takes place inside the nucleus, it can be probed outside of it in atomic physics experiments, because it is responsible for slight perturbations to atomic eigenstates. These perturbations correspond to mixing of opposite parity eigenstates into electronic states of a particular parity. As a result, an optical transition between two atomic states of the same parity (e.g. the $6S_{1/2}$ and $7S_{1/2}$ states in Cesium), that is forbidden by selection rules, can become weakly allowed due to PNC-induced mixing. Figure 1.1 illustrates this mixing for the case of the $6S_{1/2}$ and $7S_{1/2}$ states. A measurement of the extremely small Parity-Violation-induced transition moment E_{PNC} between these states provides information about the weak interaction. The Hamiltonian of the interaction has a large contribution that is nuclear spin-independent and characterized by the so-called weak charge of the nucleus Q_w, and a smaller contribution that depends on spin, which is largely due to the nuclear anapole moment κ [4]. This Hamiltonian is given by:

$$H_w = -\frac{G}{\sqrt{8}}\rho(\mathrm{r})\,\mathrm{Q_w}\,\gamma_5 + \frac{G}{\sqrt{8}}\rho(\mathrm{r})\kappa\vec{\alpha}\cdot\vec{I} \qquad (1.1)$$

where G is the Fermi constant, ρ(r) is the nuclear density, γ_5 is a Dirac matrix, $\alpha_i = \gamma_0\gamma_i$ is a product of Dirac matrices, and $\vec{I}$ is the nuclear spin.

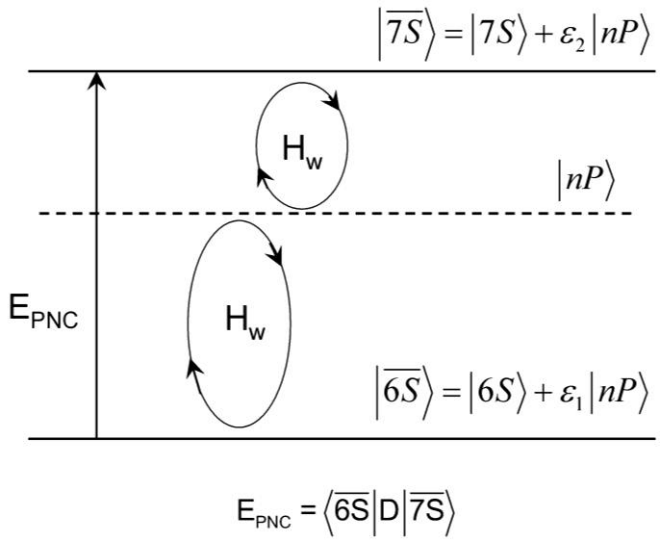

Figure 1.1: Mixing of an nP state into the 6S and 7S states in Cesium, occurring due to the weak Hamiltonian H_w. The perturbation is responsible for a small transition dipole moment E_{PNC} between the same parity eigenstates.

A laboratory determination of the transition moment E_{PNC}, combined with precision atomic structure calculations, provides an overall determination for the weak charge Q_w. $E_{PNC} = kQ_w$, where k is a form factor, that needs to be precisely calculated to obtain Q_w. The Standard Model has a prediction for the weak charge and a comparison between the two values serves as a test of the Standard Model. Potential deviations would suggest the existence of higher order effects, referred to as Physics beyond the Standard Model. In addition, a determination of the nuclear-spin dependent PNC effect, due to the nuclear anapole moment, provides important constraints to weak meson coupling constants of the Standard Model, which are currently far from being reliably established [4].

The size of the E_{PNC} transition moment is too small to be directly measured. For Cs it is on the order of 10^{-11} $e \cdot \alpha_B$, where e is the electron charge and α_B is the Bohr radius. In comparison, the electric dipole moment of an allowed transition is ~ 1 $e \cdot \alpha_B$. Measurements of E_{PNC} are possible using transition amplitude interference techniques, in which the weak transition amplitude is interfered with the amplitude of a much stronger transition. A detection of the interference term results in an effective amplification of the

PNC signal. So far, PNC experiments have been performed using two types of interference techniques. In one of these, the PNC amplitude is interfered with the amplitude of an allowed magnetic-dipole transition (M_1). The experiment takes place in an atomic vapor, and the measured quantity is optical rotation of linearly polarized light passing through the vapor. The left-right asymmetry due to the PNC effect causes the left and right circularly polarized components of light to be absorbed differently by the atoms, inducing the optical rotation. The rotation angle is proportional to the ratio E_{PNC}/M_1, i.e. the experiment yields ratios of transition moments. An independent determination of M_1 is required in order to extract E_{PNC} from the measurement. In the other interference technique, the PNC interaction interferes with a much stronger-Stark-induced interaction. The experiment takes place in a region of crossed electric and magnetic fields that define the handedness of the coordinate system. A change in this handedness (usually done by an electric or magnetic field reversal, or change in the sense of ellipticity of the optical field driving the transition) causes the Stark-PNC interference signal to modulate. A measurement of the amplitude of this modulation, normalized to the much stronger signal due to the Stark-induced transition, yields the ratio E_{PNC}/E_{Stark}, where E_{Stark} is the Stark-induced electric dipole transition moment. As in the optical rotation experiments, the Stark-PNC interference scheme too measures ratios of moments. In this thesis, we demonstrate a third, alternative transition amplitude interference technique for determining weak transition moments, also through measurements of moment ratios, based on two-pathway Coherent Control.

Over the last three decades several atomic PNC measurements have been performed in the following elements: Bismuth, Lead, Thallium, Cesium, Dysprosium and Ytterbium. The PNC effect in Bi, Pb and Tl was measured through optical rotation experiments, while the Cs, Dy and Yb measurements were carried out using the PNC-Stark interference technique. Table 1.1 lists all atomic PNC experiments with an accuracy < 5%, along with the corresponding accuracy level in most precise theoretical calculations available for the form factor $k=E_{PNC}/Q_w$. As it can be seen, the overall accuracy in the weak charge determination (excluding Cesium, where both measurement and theoretical accuracy at the sub-1% level), is limited by the precision of theoretical

calculations. Of all the PNC experiments, the latest Cesium experiment [5] is the only in which the experimental precision reached the necessary level to the measure small spin-dependent effect due to the nuclear anapole moment. The simple electronic structure of Cs (one valence electron outside a closed core) allows for very precise calculations of its wavefunctions, which permitted a sub-1% determination of the weak charge Q_w. We also note that an upper bound for the anapole moment of Thallium was placed by the Seattle group [6].

Table 1.1: Atomic PNC experiments with an accuracy < 5% in the measured ratio of transition moments. The associated uncertainty of the most precise theoretical calculations for $k=E_{PNC}/Q_w$ is also listed. Data taken from ref. [3].

Atom	Transition	Group	Year	Transition moment ratio accuracy (%)	Atomic structure precision(%)
^{209}Bi	$^4S_{3/2} - {}^2D_{3/2}$	Oxford, ref[7]	1991	2	11.5
^{208}Pb	$^3P_0 - {}^3P_1$	Seattle, ref[8]	1993	1.2	7.1
		Oxford, ref[9]	1996	3.4	
^{205}Tl	$6P_{1/2} - 6P_{3/2}$	Oxford, ref [10]	1995	2.9	3
		Seattle, ref[6]	1995	1.2	
^{133}Cs	$6S_{1/2} - 7S_{1/2}$	Boulder, ref[11]	1988	2.2	0.27
		Boulder, ref[5]	1997	0.35	

1.3 Why a new PNC measurement in Cs is interesting

Of all the PNC measurements to date the one in Cs, carried out by the Boulder group, has been the most successful. The measurements yielded a 0.35% determination of the PNC moment, which, combined with theoretical calculations, provides a value for

the electroweak charge Q_w which is in very good agreement with the Standard Model prediction. The precision the experimenters reached allowed a measurement of the anapole moment of the Cs nucleus, a 14% determination. Though this was the first observation of an anapole moment, its value was much larger than predicted and in disagreement with weak meson coupling constants measurements performed in various high energy scattering experiments. This disagreement has generated a long lasting puzzle within the nuclear physics community. An Effective Field Theory [12] was developed a few years after the Cs Boulder experiment, as an effort to fit the Cs anapole moment within the existing model of nuclear forces. new measurement of Parity Violation, which will be based on the weak measurement moment scheme we demonstrate, will serve primarily as a check of the Boulder group anapole moment result. Since our Coherent Control technique will involve different systematics, an agreement with the Boulder measurement will further enhance the confidence in the anapole moment magnitude.

A major advantage of the Cs atom as a candidate for a PNC experiment over other atoms, is its simple atomic structure (single valence electron). This has allowed for precise calculations of its wavefunctions which over the years have kept increasing in accuracy and which, in conjunction with PNC measurements, have resulted in increasingly more accurate determinations of Q_w. In a recent work [13], the theoretical uncertainty reached 0.27%, which is below the 0.35% experimental uncertainty. This result provided a new, improved determination for the weak charge Q_w, which is in excellent agreement with the Standard Model. Since the determination of Q_w is now limited by the experimental uncertainty, the possibility of an improved determination of the Q_w through new laboratory measurement of the PNC amplitude would serve as a new and more precise test for the Standard Model.

1.4 Using Coherent Control for weak signal amplification

The field of Coherent Control, as developed in the last two decades, has found various applications with regard to the manipulation of the quantum dynamics in atomic and molecular systems. One of these applications is the ability to coherently control the

excitation rate in an atomic transition, by employing multiple excitation pathways for the transition, with each of these being driven by a different laser field. The inherent coherence of transition amplitudes, when combined with mutual phase-coherence for the optical fields driving the different pathways, results in quantum mechanical amplitude interference present in the net excitation rate that can be modulated by controlling the relative phase between the different optical fields. This was first shown by Chen and Elliott [14] in a one-photon vs. three-photon ionization experiment in Mercury, where modulation of the ionization rate of the atom was demonstrated by controlling the phase-difference between the one-photon and three-photon fields. This work followed a proposal by Brumer and Shapiro [15], that suggested exploiting the quantum interference of multiple excitation pathways as a means to control product ratios in molecular reactions

Aside from its use as a method to control the transition rate in an atomic system, multiple pathway excitation using coherent fields can also be employed for the amplification and detection of a weak transition amplitude. This is possible in a two-pathway excitation scheme, by taking advantage of the ability to modulate the excitation rate, which is accomplished by coherently controlling the amplitude of the interference between the two pathways of the transition. This amplitude is essentially the product of the two pathway amplitudes, and it is therefore larger in magnitude than the contribution of the weak pathway to the overall transition rate. In this sense, the amplification is similar to the Stark-PNC or M_1-PNC interference techniques, described in section 1.2. In what follows we introduce the experimental principle of the two-pathway scheme for amplifying a weak one-photon transition.

Let's assume that we seek to detect the amplitude A_w of a weak one-photon interaction between states $|i\rangle$ and $|f\rangle$, for which the excitation rate is so low that direct detection is unpractical. This could be for instance an electric-dipole forbidden transition. In order to amplify the weak amplitude, we introduce another, strong two-photon transition pathway between the same states, with amplitude A_{2P}. The two transition pathways are shown in Figure 1.2.

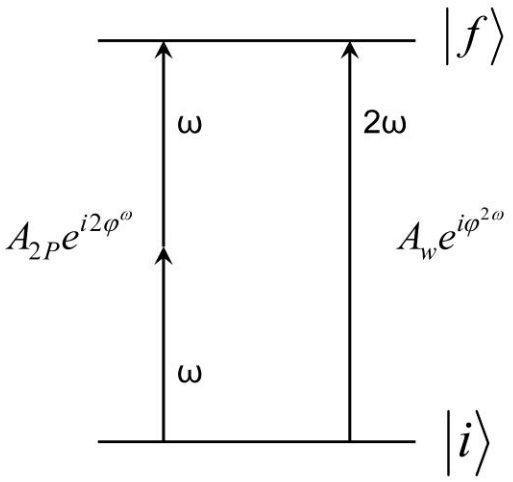

Figure 1.2: One photon vs. two-photon excitation of an atomic transition between the same initial and final state.

The amplitudes for the one-photon and two-photon pathways have the form:

$$A_{2P} = \mu^{\omega}\left(\varepsilon^{\omega}\right)^2 \tag{1.2}$$

$$A_w = \mu^{2\omega}\varepsilon^{2\omega} \tag{1.3}$$

where μ^{ω} and $\mu^{2\omega}$ are the one-photon and two-photon transition moments, and ε^{ω} and $\varepsilon^{2\omega}$ are the optical fields driving the ω and 2ω transitions respectively. These fields are phase-coherent with each other, as required in order to obtain interference between the two amplitudes. The total transition amplitude is the sum of A_w and A_{2P}:

$$\sum A = A_{2P}e^{2i\varphi^{\omega}} + A_w e^{i\varphi^{2\omega}} \tag{1.4}$$

We have retained in (1.4) the phase factors $e^{2i\varphi^{\omega}}$ and $e^{i\varphi^{2\omega}}$ that represent the phase delays we can impose on the ω and 2ω fields, respectively. For single pathway excitation, these phase factors do not have a physical meaning, but in our case they are relevant in the interference of the amplitudes of (1.4). The transition rate W is proportional to the modulus squared of the net amplitude of (1.4):

$$W \sim \left|\sum A\right|^2 = \left|A_{2P}e^{2i\varphi^{\omega}} + A_w e^{i\varphi^{2\omega}}\right|^2 \approx \left|A_{2P}\right|^2 + 2A_{2P}A_w \cos(2\varphi^{\omega} - \varphi^{2\omega}) \quad (1.5)$$

In the above expression we have dropped the term $|A_w|^2$ since it was assumed that the one-photon rate is much smaller than the two-photon rate. As it can be seen in (1.5), the transition rate *W*, aside from the large two-photon rate, contains an additional contribution due to the A_{2P} and A_w interference. This contribution is a sinusoidal function of the weighted phase-difference $\Delta\varphi = 2\varphi^{\omega} - \varphi^{2\omega}$. This dependence of the cross- term on $\Delta\varphi$ justifies the requirement for phase-coherence between the ω and 2ω fields in order to observe the multiple pathway interference. In its absence, the cross-term averages to zero. If phase-coherent fields are used, $\Delta\varphi$ is well defined, and it can be swept by delaying the phase of either field. This allows one to modulate the excitation rate and detect the interference term, which, as being the product of A_{2P} and A_w, is much larger than $|A_w|^2$. Therefore, the two-pathway excitation scheme can serve as an amplifier for the weak signal.

1.5 Earlier demonstration of Coherent Control for weak signal amplification

The use of Coherent Control for the amplification and detection of a weak atomic transition has been recently demonstrated by Gunawardena and Elliott [1,2]. This experiment was the first demonstration of Coherent Control with CW lasers, and forms the basis for the work presented in this thesis. The experiment was carried out on the 6S→8S transition in Cs, with a pair of phase-coherent optical fields (an 822 nm fundamental field and its 411 nm second harmonic) driving the 6S→8S transition through two different pathways: a strong two-photon transition and a much weaker (but controllable in strength) Stark-induced transition. The measurements are performed in a Cesium vapor cell, fitted with electric field plates for the creation of a controllable DC electric field. The 6S→8S excitation rate is detected through fluorescence collection from atoms decaying to the ground state. The interference of the one-photon and two-photon pathways is controlled by sweeping the phase difference between the two optical fields,

which is accomplished by delaying the path on the second harmonic field in a Mach-Zehnder interferometer. Figure 1.3 shows a layout of the experimental apparatus. The transition amplitude interference results in a modulation in the net excitation rate, which lies on top of the large DC background due to the two-photon rate. Figure 1.4 shows a plot of the modulating signal as a function of the 822 nm and 411 nm phase difference. The amplitude of the observed modulation, measured as a means of detecting the weak Stark-induced amplitude, was as much as two orders of magnitude greater than the Stark-induced rate on its own. The weak amplitude detection in the experiment reached the shot-noise limit for the largest of the electric fields applied to the atoms.

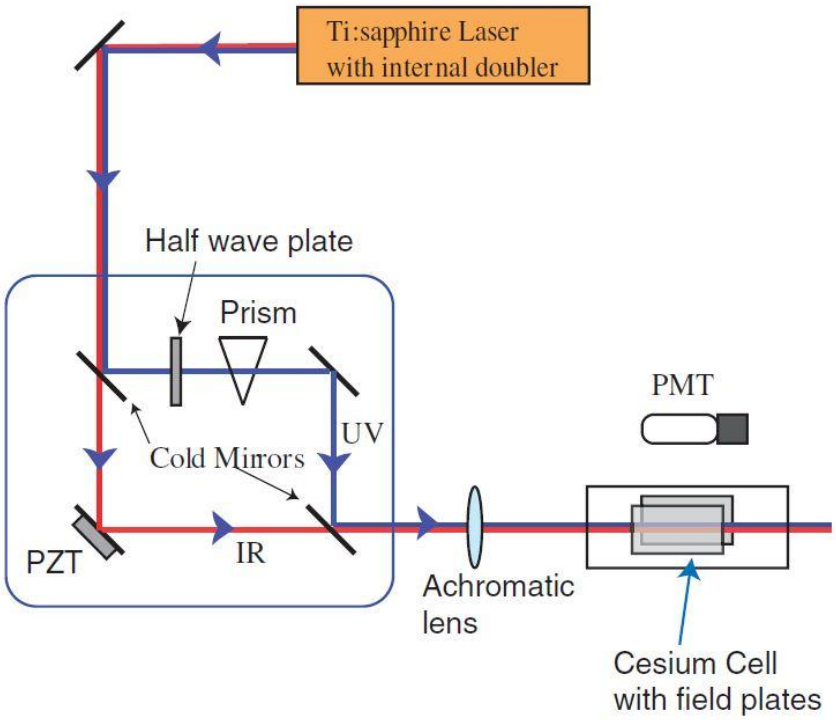

Figure 1.3: Schematic of the apparatus in Gunawardena's experiment. Figure taken from [1].

In the experiment just described, the weak signal is dependent upon quantities such as the Cesium beam density, the 822 nm and 411 nm field intensities, the two-photon amplitude, etc. In order to extract the weak transition amplitude from the

measurement, a careful calibration of these quantities is required, which is not an easy task. In chapter 2 we show how it is possible to use the two-pathway excitation scheme in a way that allows us to measure ratios of weak transition moments, so that the dependency on such parameters in removed.

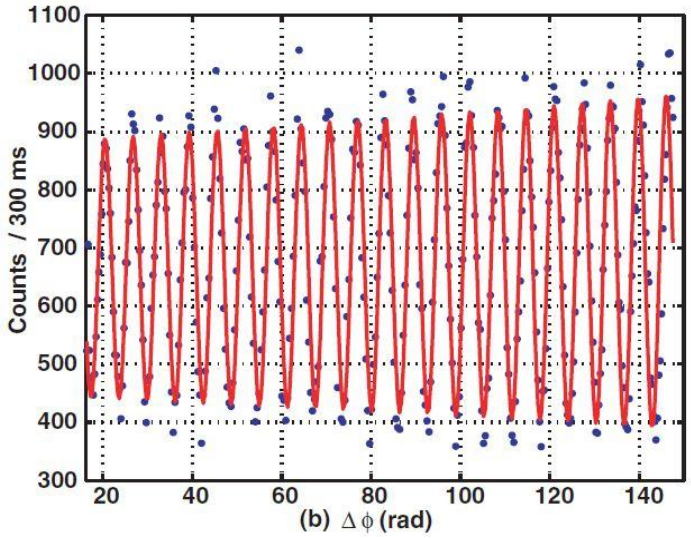

Figure 1.4: Modulation of the excitation rate for the 6S→8S transition in Gunawardena's experiment. Figure is from [1].

2. TWO-PATHWAY COHERENT CONTROL SCHEME FOR MEASURING WEAK TRANSITION MOMENTS

In this chapter we describe the principle of the two-pathway Coherent Control method that allows us to measure ratios of weak transition moments. First, we discuss the 6S→7S transition in Cesium, along with all the possible optical interactions through which the transition can occur. This is the transition on which the measurement of the M_1 transition moment is performed. Then, we describe how the two-pathway excitation through a strong two-photon transition and a combination of two weak transitions, a Stark-induced and an M_1, can be used to measure the ratio of the M_1 to the Stark-induced moment. Afterwards, we discuss the application of the same scheme, this time for measuring the ratio of the extremely small PNC moment to a Stark-induced moment on the 6S→7S transition.

2.1 The 6S→7S transition in Cesium

The 6S→7S transition in Cs has been studied extensively, both at the experimental and theoretical level, primarily due to its relation to the atomic Parity Violation studies. Figure 2.1 shows a partial energy level diagram of ^{133}Cs with the 6S ground state and the 7S level. The 7S state natural lifetime is 48.5 ns [16], which corresponds to a transition natural linewidth of 3.3 MHz. The 6S and 7S states are separated by (on average) 277,841 GHz, corresponding to a wavelength of approximately 539.5 nm. Each of the states has its own hyperfine structure, owing to the nonzero spin (I=7/2) of the Cs nucleus. The ground state is split into two levels with F=3 and F=4, separated by 9.19 GHz, and the 7S state into two components F=3 and F=4, spaced by 2.18 GHz. Each of the hyperfine levels is 2F+1 degenerate. F=I+J is the total angular momentum of the atom, where J=L+S is the total electronic angular momentum. The

2F+1 Zeeman sublevels corresponding to each F level, labeled m_F, are degenerate in a magnetic field-free region, but upon application of B, the degeneracy is lifted and the levels are shifted in energy by $\Delta E=g_F m_F \mu_B B$, where is g_F is the Lande-factor, and μ_B is the Bohr magneton.

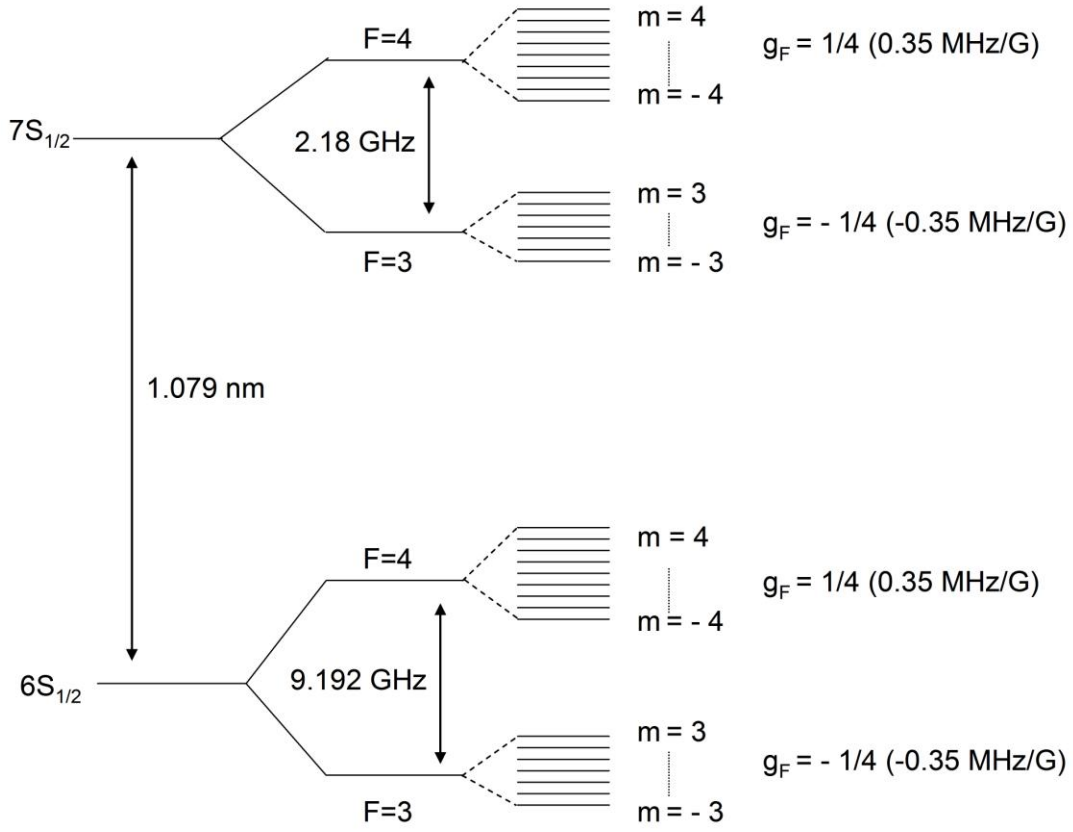

Figure 2.1: Partial energy level diagram of ^{133}Cs with $6S_{1/2}$, $7S_{1/2}$ states, hyperfine and Zeeman structure.

The 6S→7S transition, as an L=0→L'=0 transition, is to first order electric-dipole forbidden. It can be driven however, through an allowed two-photon interaction, as well as four weakly-allowed one-photon interactions: the Stark-induced interaction, the magnetic dipole interaction, the electric-quadrupole interaction, as well as the extremely weak electroweak-induced interaction. The amplitude of the two-photon interaction is second order in the optical field(s) driving the transition, whereas the amplitudes of the

latter four are linear in the optical field. Figure 2.2 illustrates the coupling of the 6S and 7S states through the above mentioned interactions.

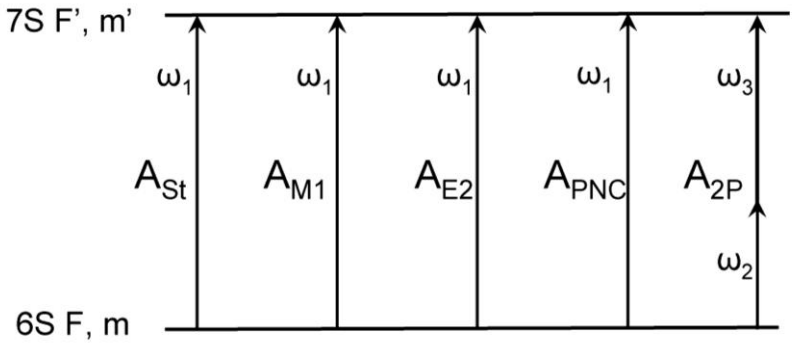

Figure 2.2 - The five possible transition pathways for coupling of the 6S and 7S levels of Cs

2.2 The five interactions coupling the 6S and 7S levels

In this section we discuss the five interaction pathways by which a 6S→7S excitation can be induced. We introduce the relevant transition amplitudes that are essential to the analysis of our Coherent Control scheme. It is the interference of such transition amplitudes that we use to amplify and detect the weak amplitude of interest. In each case, we consider a transition from a 6S F, m state to a 7S F', m' state.

2.2.1 The Stark-induced interaction

Consider a Cs atom in the region of an optical field of amplitude $\varepsilon^{\omega 1}$ of frequency ω_1 and phase $\varphi^{\omega 1}$. In the absence of an external static electric field, an S→S transition is to first order forbidden. The presence of such an electric field E_{St} (Stark field) induces mixing of opposite parity states |nP> into the |S> states through the Hamiltonian of the interaction $H_{St} = -\vec{D}\cdot\vec{E}_{St}$, thus allowing the optical transition to proceed. $\vec{D} = -e\vec{r}$ is the dipole operator. We show this mixing process pictorially for the Cs 6S and 7S states in Figure 2.3.

The electric dipole transition amplitude $A_{St}(F,m;F',m')=\langle\overline{7S}|-\vec{D}\vec{\varepsilon}^{\omega 1}|\overline{6S}\rangle$, where $|\overline{6S}\rangle$ and $|\overline{7S}\rangle$ are the perturbed $6S_{1/2}(F,m_F)$ and $7S_{1/2}(F',m_F')$ states, is given in the notation of Gilbert and Wieman [14] by:

$$A_{St}(F,m;F',m')=\{\ \left[\alpha\mathbf{E}\cdot\varepsilon^{\omega_1}\delta_{F,F'}+i\beta(\mathbf{E}\times\varepsilon^{\omega_1})_z C_{F,m}^{F',m'}\right]\delta_{m,m'} \qquad (2.1)$$
$$+\left[\pm i\beta(\mathbf{E}\times\varepsilon^{\omega_1})_x-i\beta(\mathbf{E}\times\varepsilon^{\omega_1})_y\right]C_{F,m}^{F',m'}\delta_{m,m'\pm1}\ \}e^{i\varphi^{\omega_1}}$$

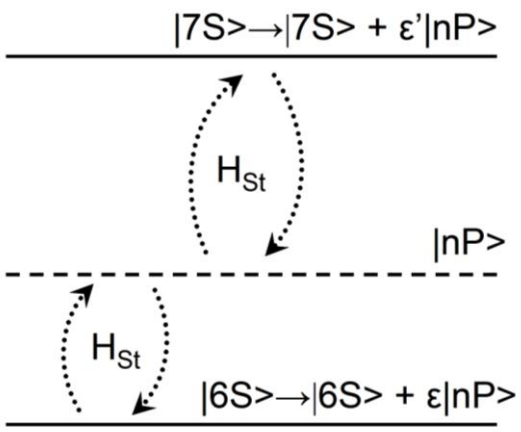

Figure 2.3: Stark-mixing of an |nP> state into the |6S> and |7S> states, occurring due to the Hamiltonian $H_{St}=-\vec{D}\cdot\vec{E}_{St}$.

The coefficients $C_{F,m}^{F',m'}$ in (2.1) are proportional to the Clebsch-Gordon coefficients and are tabulated in ref. [17] and [18]. For transitions between same F states, $C_{F,m}^{F,m}=-m_F/4$ for F=3 and $C_{F,m}^{F,m}=+m_F/4$ for F=4. α and β are the scalar and vector ac-Stark polarizabilites of the transition. They determine the amplitude of the Stark induced transition for an optical field ε^{ω_1} parallel and perpendicular to the Stark field, respectively. Explicit forms for α and β are given in ref. [19]. These quantities have been studied extensively, due to their relation to the Parity-Violation experiments on the 6S→7S transition. In particular, the calibration of the most precise PNC measurement to date, that made on the Cs 6S→7S in Cs [5], relies on accurate knowledge of β, since

what was determined in the experiment is the ratio of the PNC transition moment E_{PNC} to β. There have been two very accurate β determinations. Of these, one comes from a measurement of the α/β ratio (-9.905±0.011) [20], combined with an accurate determination of α [21,22]. α is determined using known values of matrix elements related to the Stark-mixing process and the dipole couplings between the perturbed 6S and 7S states, induced by the optical field. This method yields β=27.11(5) a_o^3. We note that β can also be computed (similarly to α), but this calculation is not as stable and precise as that of a. The second (and most accurate) β determination comes from a measurement of the ratio of the off-diagonal magnetic dipole moment in the 6S→7S transition (that can be precisely calculated) to β [23]. This determination yields β=26.96(5) a_o^3 [22]. The two independent β determinations are combined to give a weighted average of β=26.99(5) a_0^3.

2.2.2 The magnetic dipole interaction

The 6S→7S magnetic dipole transition occurs due to the interaction Hamiltonian $H_M=-\mu_M \cdot B^{\omega 1}$, and its amplitude is of the form:

$$A_{M_1} = e^{i\varphi^{\omega 1}} \left\langle 7S \left| \boldsymbol{\mu}_M \cdot \mathbf{B}^{\omega 1} \right| 6S \right\rangle \tag{2.2}$$

where $\boldsymbol{\mu}_M = \mu_B \left(g_L \mathbf{L} + g_S \mathbf{S} + g_I \mathbf{I} \right)$ is the magnetic dipole moment and $B^{\omega 1}$ is the magnetic flux density of the optical field driving the transition. **L**, **S**, and **I** are the orbital angular momentum, the electronic spin, and the nuclear spin respectively. g_L, g_S, g_I are the corresponding gyromagnetic ratios. For the 6S and 7S states, the orbital angular momentum L=0. In addition, the nuclear magnetic spin contribution to μ_M is much smaller than that of the electronic spin, and so the corresponding term can be dropped in the expression for μ_M, leaving **S** as the only contribution: $\boldsymbol{\mu}_M \approx \mu_B g_S \mathbf{S}$. Due to the orthogonality of the spatial part of 6S and 7S states, the matrix element of (2.2) is to first order zero. However, configuration interactions and relativistic corrections relax this somewhat, allowing a small moment for the 6S→7S transition [24,25,26]. The amplitude of (2.2) can be written as:

$$A_{M_1} = -\left\{(\hat{k}\times\varepsilon^{\omega_1})_z\delta_{m,m'} + \left[\pm(\hat{k}\times\varepsilon^{\omega_1})_x + i(\hat{k}\times\varepsilon^{\omega_1})_y\right]\delta_{m,m'\pm1}\right\} e^{i\varphi^{\omega 1}} M C_{F,m}^{F',m'} \qquad (2.3)$$

$\hat{\boldsymbol{k}} = \boldsymbol{k}^{\omega 1}/\left|\boldsymbol{k}^{\omega 1}\right|$ is the unit wave-vector of the optical field and $M = \langle 7S|\mu_z/c|6S\rangle$ is the magnetic dipole transition moment. This moment has been measured in a series of experiments, primarily due to its relation to the PNC measurements [23,27,28,29,30]. The most accurate of the existing determinations is M_1 = - 4.241(10) x 10^{-5} $|\mu_B/c|$ [23]. The authors of [31] have shown that *M* depends on the particular initial F and final F' states of the transition. *M* can be expressed as:

$$M = M_1 + M_{hf}(\text{F-F'}) \qquad (2.4)$$

M_{hf} is the off-diagonal amplitude which contributes to the overall moment for $\Delta F \neq 0$ transitions and it is due to mixing introduced by the hyperfine interaction. The most precise determination of the vector polarizability β (a quantity used in the interpretation of the Parity-Violation measurements of the Boulder group), comes from a measurement of the ratio M_{hf}/β [23]. Due to this, several calculations of M_{hf} have been reported [31, 32, 33]. Of these, the most accurate is at the 0.2% level: M_{hf} = 0.8094(20) x 10^{-5} $|\mu_B/c|$ [31]. In this thesis, we make a new determination of the magnetic dipole moment M_1 by employing $\Delta F=0$ transitions. The particular selection rule implies that our measurements are not sensitive to M_{hf}.

2.2.3 The electric–quadrupole interaction

The electric-quadrupole interaction is to first-order forbidden, but due to hyperfine mixing, it becomes weakly allowed, with transition amplitude given by [34]:

$$A_{E2} = -e^{i\varphi^{\omega 1}}\langle 7S|\left[\left(\mathbf{S}\cdot\varepsilon^{\omega_1}\right)\left(\mathbf{I}\cdot\hat{\mathbf{k}}\right) + \left(\mathbf{S}\cdot\hat{\mathbf{k}}\right)\left(\mathbf{I}\cdot\varepsilon^{\omega_1}\right)\right]|6S\rangle E_2/2 \qquad (2.5)$$

E_2 is the electric-quadrupole moment, which has an estimated value of $0.05M_{hf}$ [34]. The interaction only contributes for $\Delta F=\pm1$, $\Delta m=\pm1$ transitions. In our experiment, we employ $\Delta F=0$, $\Delta m_F=0$ transitions, so the E_2 does not contribute to our signal.

2.2.4 The PNC interaction

The electroweak interaction between the nucleons and electrons in the Cs atom is responsible for a very small dipole transition moment between the 6S and 7S states, as discussed in (chapter 1). This moment arises from mixing of opposite parity eigenstates (P states) into the 6S and 7S states due to the electro-weak Hamiltonian H_w. The mixing process is illustrated in figure 1.1.

The amplitude the PNC-induced dipole transition has the general form:

$$A_{PNC} = \left\langle \overline{7S} \right| -\vec{D}\cdot\vec{\varepsilon}^{\omega 1} \left| \overline{6S} \right\rangle \tag{2.6}$$

where $\vec{D} = -e\vec{r}$ is the dipole operator and $\vec{\varepsilon}^{\omega 1}$ the optical field driving the transition. $\left|\overline{6S}\right\rangle$ and $\left|\overline{7S}\right\rangle$ are the 6S and 7S states respectively, perturbed by the weak interaction. A_{PNC} can be expressed as:

$$\begin{aligned} A_{PNC} &= e^{i\varphi^{\omega 1}} \left\langle 7S \left| \varepsilon^{\omega_1}\cdot\boldsymbol{\sigma}\cdot i\,Im(E_{PNC}) \right| 6S \right\rangle \\ &= \left[\varepsilon_z^{\omega_1}\delta_{m,m'} + \left(\pm\varepsilon_x^{\omega_1} + i\varepsilon_y^{\omega_1} \right)\delta_{m,m'\pm 1} \right] e^{i\varphi^{\omega_1}} iIm(E_{PNC}) C_{F,m}^{F',m'} \end{aligned} \tag{2.7}$$

$E_{PNC} = \left\langle \overline{7S} \left| D_z \right| \overline{6S} \right\rangle$ is the purely imaginary dipole transition moment, arising from the electro-weak interaction. It has been measured in a series of experiments, the most accurate of which is the one by the C. Wieman group [5], a determination (reported in terms of the vector polarizability β) that reached the unprecedented level of 0.35 % accuracy: $Im(E_{PNC})/\beta$ = - 1.5935(56) mV/cm. This corresponds to a PNC transition moment ~ $0.9\cdot 10^{-11}$ $e\cdot\alpha_B$. In comparison, the transition moment for an electric-dipole allowed transition is approximately 1 $e\cdot\alpha_B$. The PNC induced moment is much smaller than all other moments that are relevant in the M_1 measurements (approximately $5\cdot 10^{-5}$ times smaller than M_1), and we therefore do not need to consider its contribution as a systematic effect in the M_1 experiment.

2.2.5 The two-photon interaction

The last 6S→7S excitation pathway we discuss is through an allowed two-photon interaction. It is the interference of this large transition amplitude with the weak amplitude that we exploit in order to amplify the weak signal in our measurements. In the experiment presented in this thesis, we use degenerate photons to drive the two-photon pathway. Since the intermediate level of the two-photon process is not real, the transition has a modest strength, but its amplitude can be made to be (for the available laser power and beam focusing conditions) many orders of magnitude greater than the Stark–induced, the magnetic-dipole, and the PNC transition amplitudes.

The 6S→7S two-photon transition amplitude, in the general case of non–degenerate fields ε^{ω_2} and ε^{ω_3} with frequencies ω_2 and ω_3 respectively can be shown to be [35,36,37]:

$$A_{2P}(F,m;F',m') = \{ \left[\tilde{\alpha}\, \varepsilon^{\omega_2} \cdot \varepsilon^{\omega_3} \delta_{F,F'} + i\tilde{\beta} (\varepsilon^{\omega_2} \times \varepsilon^{\omega_3})_z C_{F,m}^{F',m'} \right] \delta_{m,m'} + \left[\pm i\tilde{\beta} (\varepsilon^{\omega_2} \times \varepsilon^{\omega_{31}})_x - i\tilde{\beta} (\varepsilon^{\omega_2} \times \varepsilon^{\omega_3})_y \right] C_{F,m}^{F',m'} \delta_{m,m'\pm 1} \}\, e^{i(\varphi^{\omega 2} + \varphi^{\omega 3})} \tag{2.8}$$

The form of the A_{2P} is similar to that of the Stark-induced amplitude, as it can be seen by comparing (2.8) with (2.1). The scalar term $\tilde{\alpha}$ and vector term $\tilde{\beta}$ are real quantities that characterize the two-photon amplitude for polarizations of the fields ε^{ω_2} and ε^{ω_3} parallel and perpendicular to each other respectively. Since a single laser field is used to drive the two-photon transition, $\varepsilon^{\omega_2} = \varepsilon^{\omega_3}$ and the two photons are degenerate in frequency. Only $\Delta F=0$, $\Delta m_F=0$ two-photon transitions are allowed in this case. The transition amplitude takes the simple form:

$$A_{2P} = \tilde{\alpha} \left(\varepsilon^{\omega_2} \right)^2 e^{i(2\varphi^{\omega 2})} \tag{2.9}$$

$\Delta F=\pm 1$ two-photon transitions are possible if the two photons have different frequencies and polarizations. With the use of the F=3→F'=4 and F=4→F'=3 transitions, we could make measurements of the off-diagonal component of the magnetic dipole moment M_{hf} (equation) as well as measurements of the spin-dependent PNC effect on an alternative set of transitions. This possibility of employing $\Delta F=\pm 1$ transitions, would add

to the complexity of the experiment however, since two laser fields would be required to drive the two-photon transition, and these fields would also need to be phase-coherent with the field driving the one-photon transition. The degenerate two-photon process offers an additional advantage, because only $\Delta m_F=0$ excitations are allowed for the two-photon interaction in this case. Since the multiple-pathway interference than we employ for the weak transition measurements can only occur between the same initial and final states, the presence of $\Delta m_F=\pm 1$ contributions to the net one-photon transition amplitude does not affect the measurements, since these contributions do not interfere with the two-photon amplitude. This is a major advantage of the two-pathway Coherent Control scheme, compared to the Stark-PNC interference scheme.

2.3 Two-pathway Coherent Control for measuring weak transition moment ratios

In Chapter 1 we introduced the two-pathway Coherent Control technique as a tool to amplify and detect weak transition amplitude. We now show that the two-pathway excitation with a combination of a strong transition and two weak transitions (such as the Magnetic dipole and Stark-induced amplitude) can be used for measurements of the ratio of the two weak transition moments. We have demonstrated the applicability of this new scheme, through a precision determination of the ratio of the magnetic dipole transition moment M_1 to the vector-polarizability β in the 6S→7S transition, presented in chapter 4. In the following sections, we discuss the specifics of the technique for the M_1/β measurement and afterwards its future application to measurement of the ratio E_{PNC}/α.

2.3.1 Application in measurements of M_1/β

Let's assume that a Cesium atom is in the presence of two phase-coherent optical fields, a fundamental field of frequency ω_2 at 1079 nm, which drives a $\Delta F=0$, $\Delta m_F=0$ 6S→7S two-photon transition (i.e. either the F=3→3 or F=4→4) , and its second harmonic ω_1 ($\omega_1=2\omega_2$) at 539.5 nm, which can drive one-photon transitions between the same states. These one-photon transitions can be the Stark-induced, the magnetic dipole or the extremely weak PNC transition. We can neglect contributions of the latter interaction in our model, since its magnitude is much smaller than all other contributions ($\sim 5\cdot 10^{-5} M_1$). In addition, we do not need to consider electric quadrupole transitions,

since these only occur between ΔF=+/-1 states. The weak pathway that is going to interfere with the strong two-photon pathway is a combination of the Stark-induced and the M_1 transitions. As we will show, the presence of the Stark-induced amplitude (the "β" term in particular) serves as a convenient means of calibrating the M_1 amplitude, i.e. it allows us to measure the ratio of M_1 to β.

The interaction of the laser fields with the Cs atoms takes place in a region of crossed DC electric and magnetic fields, which along with the direction of propagation of the optical beams, define the coordinate system of the apparatus. The electric field is needed to induce Stark-transitions, and the magnetic field defines the quantization axis of the system. With a proper choice of the orientation for the DC fields and the polarization of the field driving the weak transitions, we can select the transition amplitudes required for the measurement, while at the same time unwanted contributions to the net transition amplitude are suppressed. Without loss of generality, we define the optical beam direction of propagation as the y-axis. With this definition, a Stark-field E_y (i.e. parallel to the optical fields) and a magnetic field B_z, combined with linear polarization along the x-axis for the ω_1 field driving the one-photon pathways (i.e. $\varepsilon_x^{\omega 1}$), will induce an M_1 as well as a "β" Stark-induced transition. These interactions will interfere with the two-photon transition. We show in figure 2.4 the orientations of all the relevant optical and DC fields present in the interaction region. The orientation of the ω_2 field polarization (collinear with the ω_1 field) is not shown in the figure, since this does not affect the interference of the transition pathways.

The one-photon amplitudes for the field geometry of figure 2.4 are:

$$A_{M_1} = -M_1 \varepsilon_x^{\omega_1} C_{F,m}^{F,m} e^{i\varphi\omega_1} \tag{2.10}$$

$$A_{St} = -i\beta E_y \varepsilon_x^{\omega_1} C_{F,m}^{F,m} e^{i\varphi\omega_1} \tag{2.11}$$

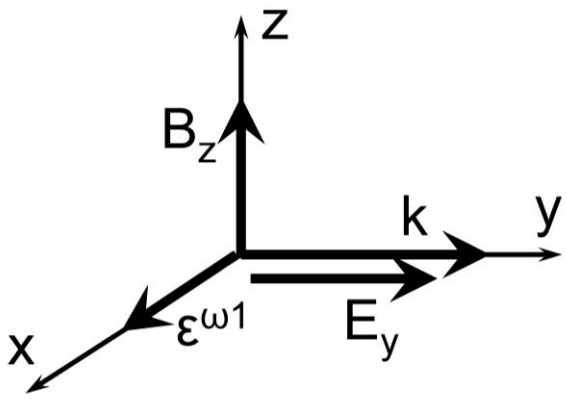

Figure 2.4: Experimental field geometry for measurements of M_1/β

At this point we must note that the terms (2.10) and (2.11) are the only contributions to the total one-photon amplitude, under the assumption of perfect DC field and optical field polarization alignment with the coordinate system of the apparatus. Field misalignments will introduce additional terms in the total amplitude that could create complications in the experiment. Fortunately, with the exception of a Stark contribution $aE_x\varepsilon_x^{\omega_1}$ that we can handle easily in our data analysis (as discussed in chapter 4), all these terms are products of two or three misalignments, and therefore their contributions are insignificant at the level of the measurement accuracy we achieve in the M_1/β experiment (~0.3%).

The (2.10) and (2.11) amplitudes interfere with the two-photon amplitude:

$$A_{2P} = \left|A_{2P}\right| e^{2i\varphi^{\omega 2}} \tag{2.12}$$

The transition rate is the modulus squared of the net amplitude:

$$\begin{aligned} W &= \left| \left|A_{2P}\right| e^{2i\varphi^{\omega 2}} - \left(\mathrm{M}_1 + i\beta \mathrm{E}_y\right) \varepsilon_x^{\omega_1} C_{F,m}^{F,m} e^{i\varphi^{\omega_1}} \right|^2 \\ &\approx \left|A_{2P}\right|^2 - K\left(E_y\right)\cos\left(\Delta\varphi + \delta\varphi(\mathrm{E}_y)\right) \end{aligned} \tag{2.13}$$

Terms which are second order in the $\varepsilon^{\omega 1}$ field have been omitted from (2.13) since their contribution is negligible. The interference of the one-photon and two-photon pathways appears in the excitation rate through the cross-term in (2.13). This term has an E_y-dependent amplitude:

$$K(E_y) = 2\left|A_{2P}\right|\varepsilon_x^{\omega_1} C_{F,m}^{F,m}\sqrt{M_1^2 + \left(\beta E_y\right)^2} \tag{2.14}$$

The phase of the cross-term consists of the weighted phase-difference between the two optical fields $\Delta\varphi = 2\varphi^{\omega 2} - \varphi^{\omega_1}$ as well as an E_y-dependent phase:

$$\delta\varphi\left(E_y\right) = \tan^{-1}\left(\frac{\beta E_y}{M_1}\right) \tag{2.15}$$

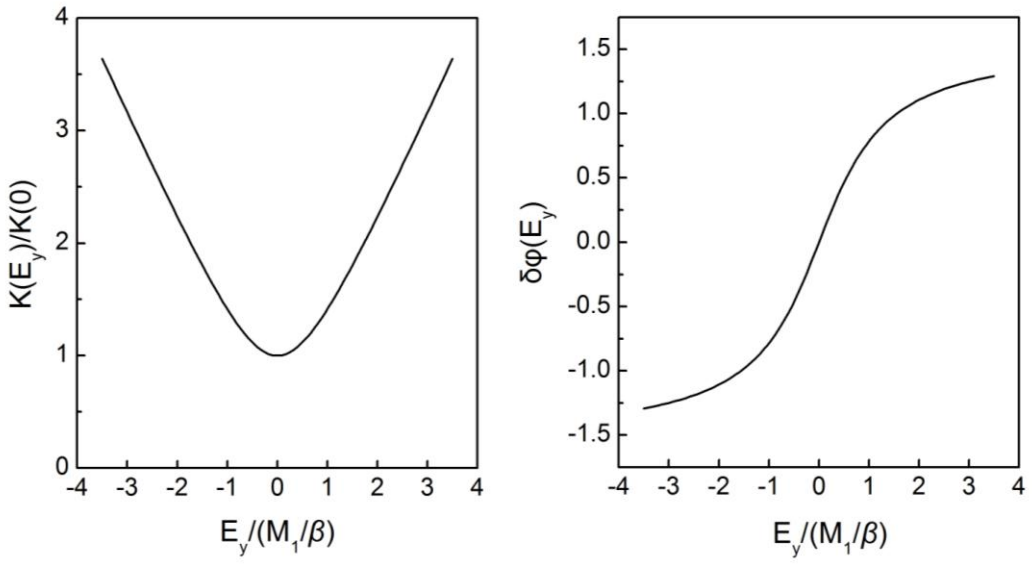

Figure 2.5: Amplitude (left) and phase (right) of modulation in the net transition rate as a function of the Stark field E_y.

The amplitude of the cross-term has a convenient form which we exploit in order to determine the magnetic dipole transition amplitude. $K(E_y)$ is a hyperbolic function of the electric field E_y. We show a plot of $K(E_y)$ (normalized to K(0)), vs. E_y in Figure 2.5. Observations of this amplitude for different electric field values, allow us to

compare the M_1 moment to the Stark-moment βE_y, and obtain the ratio $|M_1/\beta|$. The ability to measure M_1 in terms of β, justifies the selection of a dual (M_1 and "β") one-photon excitation pathway. The advantage of this approach is that knowledge of parameters such as the two-photon amplitude or the optical field intensities is not required. We only require that these parameters remain stable during the course of the measurements. As discussed in chapter 4, the interference term in the excitation rate in (2.13) can be modulated by sweeping the phase difference Δφ, as a means of determining the amplitude $K(E_y)$.

In addition to measuring the $|M_1/\beta|$ ratio, it is possible to determine the sign of M_1/β. This requires observations of the phase-shift $\delta(E_y)$ of (2.15) vs. E_y. Figure 2.5 shows the expected dependence of $\delta(E_y)$ vs. E_y.

One might ask why we choose to measure the M_1 moment in terms of β instead of the scalar polarizability α. The primary reason for this is because in the first case the two weak amplitudes (M_1 and βE_y) add in quadrature, as (2.13) shows. This feature reduces the measurement sensitivity to stray electric fields present in the interaction region. In the presence of a stray electric field ΔE_y, the amplitude of modulation (2.14) becomes:

$$K(E_y) = 2\left|A_{2P}\right|\varepsilon_x^{\omega_1} C_{F,m}^{F,m}\sqrt{M_1^2 + \beta^2\left(E_y + \Delta E_y\right)^2} \tag{2.16}$$

The effect of the stray field is to shift the vertex of the hyperbola of figure 2.5. However, the value of M_1/β, which can be determined as the ratio of the limit of $K(E_y)$ for large E_y to K_{min}, is unaffected by the presence of ΔE_y. If instead we wanted to measure M_1/α, we would choose a field geometry that activates the α-Stark and M_1 amplitudes (DC electric field in the z-axis, and optical polarization $\varepsilon^{\omega_1} = \varepsilon_x^{\omega_1}\hat{x} + \varepsilon_z^{\omega_1}\hat{z}$). The M_1 and α-Stark amplitudes add in-phase, resulting in amplitude for the interference term:

$$K(E_z) = 2\left|A_{2P}\right|\left|M_1 C_{F,m}^{F,m}\varepsilon_x - aE_z\varepsilon_z\right| \tag{2.17}$$

This amplitude increases linearly with E_z. A determination of M_1/α is possible by making measurements at different E_z values. M_1/α is obtained as the ratio of the slope of $K(E_z)$ to

K(0). In the presence of a stray field ΔE_z, K(0) would shift by $a\Delta E_z\varepsilon_z$. Therefore the measurement is sensitive to stray fields.

A second reason why measuring M_1/α is more challenging, is because the scheme just described would actually yield $M_1 C_{F,m}^{F,m}/\alpha$. $C_{F,m}^{F,m}$ is a factor proportional to m_F. We would have to measure precisely the atomic population distribution among the different m_F levels, in order to obtain M_1/α. This is not necessary in the M_1/β scheme, since as it can be seen in (2.14), the $C_{F,m}^{F,m}$ is factored-out in the $K(E_y)$ amplitude. However, considering that the population among Zeeman sublevels is generally uniform, it follows that no interference signal between the two-photon and the M_1 and β-Stark amplitudes can be observed without some spin-polarization, since atoms in opposite m_F states contribute with opposite signs to the amplitude of (2.14). In Chapter 3, we discuss the state-preparation we perform to the atoms, which allows us to transfer more than 90% of the atoms to an extreme m_F state.

2.3.2 Application in measurements of Im(E_{PNC})/α

In the final section of this chapter, we illustrate how the two-pathway Coherent-Control scheme can be used for future measurements of the extremely weak PNC moment. The experimental principle is very similar to the one presented for the M_1/β determination. The combination of a PNC and Stark-induced amplitude (the α-Stark in this case) interfere with the strong two-photon amplitude. These two weak amplitudes add with quadratures phases, which is necessary, as explained in the previous section, in order to reduce sensitivity of the measurement to stray electric fields. Measurements of the amplitude of modulation in the overall excitation rate allow a determination of the ratio of Im(E_{PNC}) to a.

The field geometry which induces the α-Stark and PNC excitations, while suppressing other contributions, is shown in figure 2.6. The optical fields propagate in the y-direction, and the DC electric and magnetic field point along the z-axis, as does the $\varepsilon_{\omega 1}$ optical field driving the weak transitions. Owing to the extremely small size of the PNC

moment (~$5\cdot10^{-5}M_1$), careful control of the various field orientations and uniformity becomes critical, since very small imperfections can introduce large (relative to the PNC moment size) systematic contributions to the overall one-photon transition amplitude. The hardships involved in characterizing and controlling the various systematic contributions to the signal, largely explain the long term character of Atomic PNC experiments.

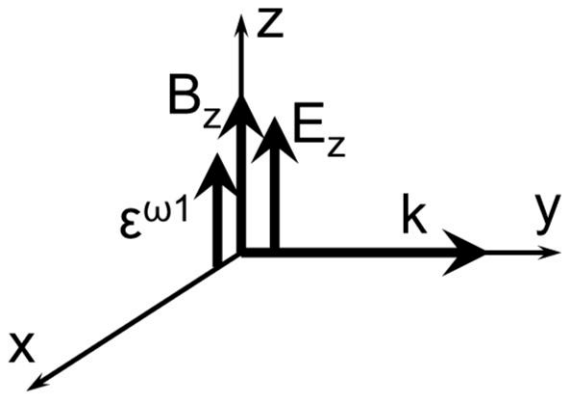

Figure 2.6: Experimental field geometry for measurements of $\mathrm{Im}(E_{PNC})/\alpha$

For the field geometry of figure 2.6, the Stark-induced and PNC amplitudes are given by:

$$A_{St} = \alpha E_z \varepsilon_z^{\omega_1} e^{i\varphi\omega_1} \tag{2.18}$$

$$A_{PNC} = iIm(E_{PNC})\varepsilon_z^{\omega_1}\ C_{F,m}^{F,m} e^{i\varphi^{\omega_1}} \tag{2.19}$$

These weak amplitudes interfere with the two-photon amplitude, resulting in an overall transition rate:

$$\begin{aligned} W &= \left| \left| A_{2P} \right| e^{2i\varphi^{\omega 2}} + \left(aE_z + iIm(E_{PNC})\, C_{F,m}^{F,m} \right) \varepsilon_z^{\omega_1} e^{i\varphi^{\omega_1}} \right|^2 \\ &\approx \left| A_{2P} \right|^2 + K\left(E_z\right) \sin\left(\Delta\varphi + \delta\varphi(E_z)\right) \end{aligned} \tag{2.20}$$

The amplitude and phase of the modulating part of the transition rate are given by:

$$K(E_z) = 2\left|A_{2P}\right|\varepsilon_z^{\omega_1}\sqrt{\left(aE_z\right)^2 + \left(Im(E_{PNC})\, C_{F,m}^{F,m}\right)^2} \tag{2.21}$$

and

$$\delta\left(E_z\right) = \tan^{-1}\left(\frac{aE_z}{Im(E_{PNC})\, C_{F,m}^{F,m}}\right) \tag{2.22}$$

Similarly to the method discussed in section (2.3.1), observations of the amplitude $K(E_z)$ for various electric fields, can yield the ratio $\left\langle C_{F,m}^{F,m}\right\rangle Im(E_{PNC})/\alpha$, and observations of the phase-shift $\delta(E_z)$ vs. E_z yield the sign of $Im(E_{PNC})/\alpha$. Figure 2.7 shows plots of the expected $K(E_z)$ and $\delta(E_z)$ vs. E_z.

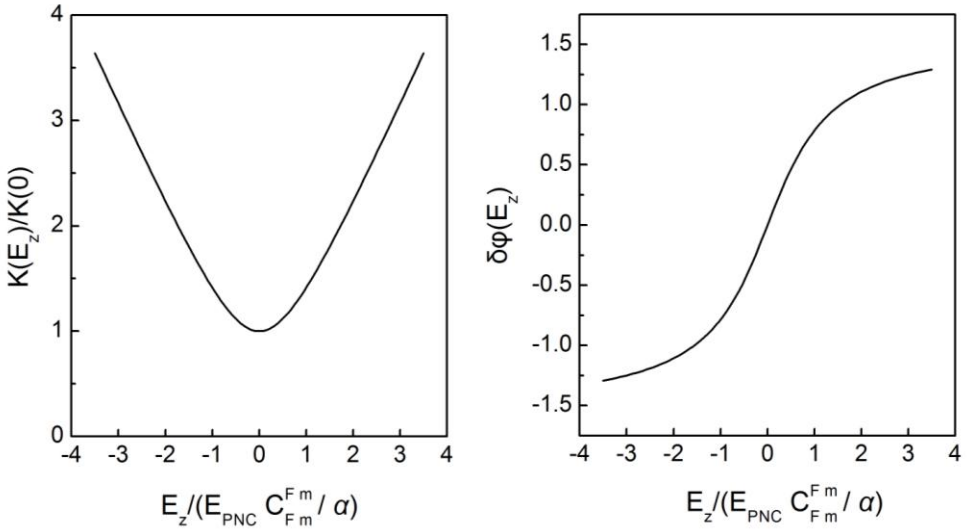

Figure 2.7: Amplitude (left) and phase (right) of modulation in the net transition rate as a function of the Stark field E_z.

3. THE APPARATUS FOR THE M_1 EXPERIMENT

3.1 Overview of the experimental apparatus

The Coherent Control scheme we demonstrate in the measurements of the magnetic dipole transition amplitude as well as its future extension to the PNC measurements makes use of a beam of Cs atoms. An atom beam is a convenient platform for the weak transitions experiments, because we benefit from employing a proven detection scheme of the 6S→7S excitations (developed by the Colorado group in their PNC experiments) which is much more efficient than the more commonly used scheme of fluorescence detection through imaging. In addition to this, our Coherent control scheme requires atoms prepared to a particular (F,m_F) component of the $6S_{1/2}$ ground state. The atom beam provides a nice environment for the state preparation, in which preparation can be done in a location remote from the 6S→7S interaction region, and so the various static field requirements for both the preparation and interaction region can be met without significant difficulty. Alternative platforms for the weak transition experiments could be a Magneto Optical Trap (MOT), or a vapor cell, but in these, state preparation and subsequent detection of the 6S→7S excitations would not be possible to implement with the ease that the atom beam permits us to do. In addition, in these platforms it would be much more challenging to satisfy the static field requirements, especially in the interaction region of the atoms with the optical fields.

The Cs beam is housed in a vacuum chamber, and along its path it intersects multiple laser beams in three different regions: The preparation (or optical pumping), the interaction, and the detection region. We show a schematic layout of the apparatus in figure 3.1.

In the optical pumping region, the atom beam crosses a pair of two laser fields at 852 nm, which optically pump the atoms into a single (F,m_F) hyperfine component of the

$6S_{1/2}$ ground state. This can be either the (3,3), (3,-3), (4,4) or (4,-4). Preparation to a single m_F level is necessary in order to observe interference between the two-photon transition amplitude and the weak amplitude (M_1, β-Stark or E_{PNC}), since the transition amplitudes for Zeeman sublevels of opposite m_F have opposite signs. In the absence of at least some m_F polarization, the interference would vanish.

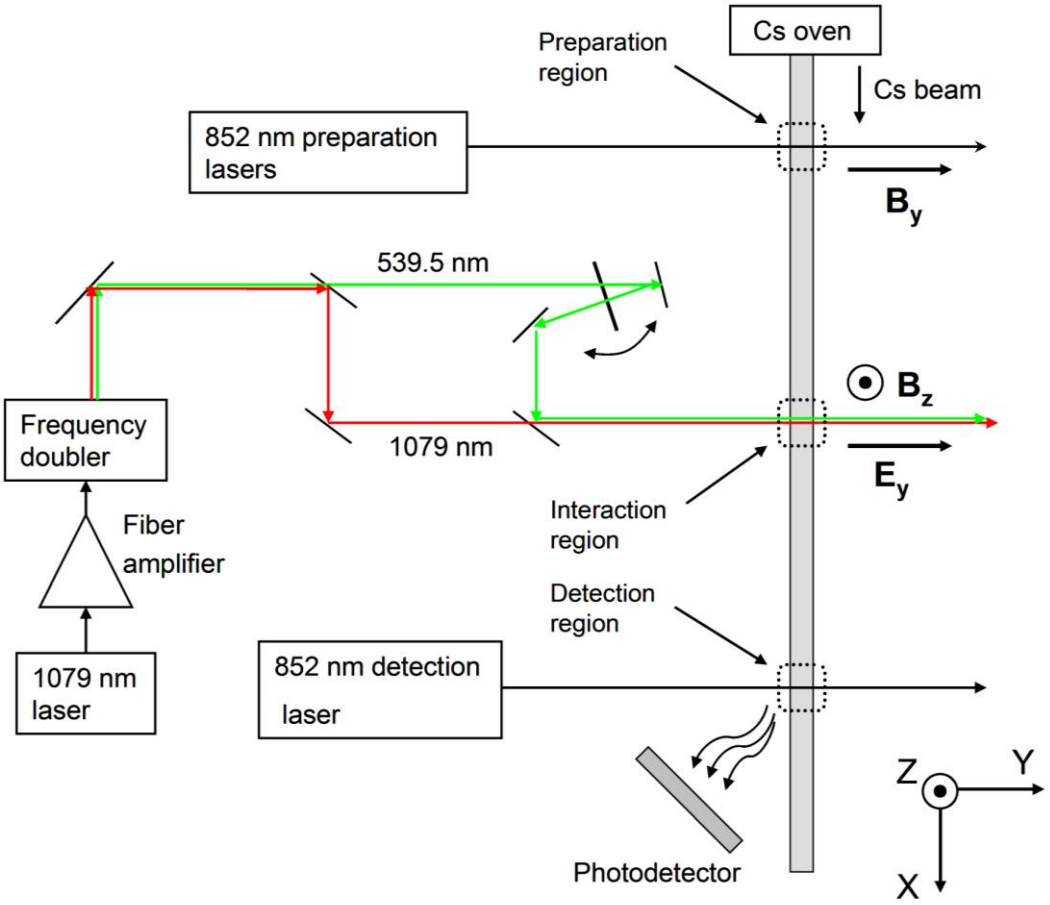

Figure 3.1: Schematic layout of the experiment for the M_1 measurements

After state preparation the atoms travel downstream and enter the interaction region. In this region, atoms intersect two overlapping laser beams, one at frequency ω_1 (λ_1=539.5 nm) and another at frequency $\omega_2=\omega_1/2$ (λ_2=1.079 μm). The component at ω_1 is produced via frequency doubling of ω_2, so the two laser fields are phase-coherent. The ω_2 component excites a strong (in relative terms) two-photon transition between the 6S and

7S states, and the ω_1 component drives a weak one-photon transition between the same states, which can be a Stark-induced, a magnetic dipole, a PNC transition or a combination of these. We are able to select which of these weak interactions are active by appropriately setting the DC electric field and magnetic fields, present in this region, as well as the laser polarization $\varepsilon^{\omega 1}$ (see section 2.3.1).

The Coherent control scheme we introduced in chapter 2, and we employ for the weak transition measurements, relies on the ability to modulate the quantum mechanical phase-difference between the strong and weak amplitudes, by modulating the optical phase-difference of the two mutually coherent lasers fields driving the two transitions pathways. We modulate this optical-phase difference in our apparatus, by splitting the green and IR beams in a Mach-Zehnder interferometer, phase-delaying the 540 nm beam, and then recombining them. The delay is imposed by double-passing the beam through a galvanometer-mounted plate. By sweeping the phase of the green beam, we create a modulation in the 6S→7S excitation rate, synchronous with the 540 nm phase modulation, which allows us to separate the two-photon and weak amplitude interference from the (much stronger) two-photon rate through phase-sensitive detection in the 6S→7S transition rate.

The detection of the 6S→7S excitation rate is done with a scheme developed by the Colorado group for their PNC experiment [5]. In this scheme, further downstream from the interaction region, atoms intersect another laser beam at 852 nm. This laser is tuned to excite atoms which, after undergoing the 6S→7 S transition, have decayed down to the hyperfine component of the ground state which was depleted during the optical pumping process. The detection laser puts these atoms into a cycling transition of the D_2 line, thus scattering many photons and making the detection of the 6S→7S transition very efficient. A large-area photodiode placed in proximity to the detection region collects some of the emitted fluorescence. With this scheme, the collection efficiency (percentage of 6S→7S excitations we are able to detect) approaches unity, whereas in the case of fluorescence detection from the interaction region, the efficiency would likely be at least an order of magnitude smaller.

3.2 Laser instrumentation for the M_1 transition experiment

In this section we describe the laser systems we have constructed for the Cs weak transition measurement apparatus. These are four External Cavity Diode Lasers (ECDL) at 852 nm and another ECDL system at 1079 nm. A pair of 852 nm lasers are necessary for state preparation of the Cs atom beam, a single laser is needed for detecting the atoms undergoing 6S→7S excitations, and another is used for the Raman Spectroscopy employed to determine the quality of the state preparation. The 1079 nm laser is used to induce the 6S→7S two-photon transitions, and it is also the source for the second harmonic generation of the 540 nm, driving the 6S→7S one-photon transitions. We discuss the required specifications for these lasers and we provide details regarding their construction. We also present the optical setups and design of electronics necessary to control and frequency stabilize these lasers.

3.2.1 The 852 nm External Cavity Diode Laser systems

The state preparation of Cs atoms into a single hyperfine component of the ground state, as well as the detection of atoms undergoing 6S→7S transitions, require CW lasers at 852 nm. Two lasers are necessary for preparing atoms and another for detecting the 6S→7S transitions. We need to be able to tune and frequency stabilize each of these lasers to one of the components of the D_2 line ($6S_{1/2}$ F=3→ $6P_{3/2}$ F=2, 3, 4 and $6S_{½}$ F=4→ $6P_{3/2}$ F=3, 4, 5). The three lasers must generate sufficient power to saturate the transitions they excite. In addition, the frequency noise of the lasers, when stabilized to a reference resonance, has to be low enough so that the noise introduced by the lasers to the detection of 6S→7S transition rate does not affect the detection significantly.

The above requirements can be satisfied by ECDL systems [38,39]. ECDLs are easy to construct, requiring a minimal number of mostly readily available components and are therefore very economical compared to other alternatives (such as Ti:Sapphire or Dye lasers). In addition, they are very easy to operate and require very little maintenance. The main feature of an ECDL is the use of optical feedback from a diffraction grating in order to enhance the spectral characteristics and tunability of a laser diode. In what follows we give a brief introduction to the Littrow ECDL, which is the most common

type of an ECDL and the type that we have implemented for our experiment. An alternative, but less common external cavity design is the Littman-Metcalf design, which offers narrower linewidth, but has a somewhat more complicated setup. Another interesting approach to enhancing the tunability and spectral purity of a laser diode, is the use of optical feedback provided not by a grating, but instead by an optical cavity [40]. It is known to provide very narrow linewidths (20 kHz or less), but compared to a Littrow design, it allows limited wavelength tunability and it is more costly than an ECDL, since a separate optical cavity is required for each laser system.

In a Littrow laser, light from a laser diode is directed to a diffraction grating, aligned such that the diffracted light is injected back to the diode. When subjected to optical feedback, the laser diode is forced to oscillate at the frequency at which the feedback is maximum. This has two important consequences. First, the laser diode linewidth is reduced from about 30 MHz to ~ 1 MHz, i.e. from a value greater than the typical atomic resonance linewidth to one which is lower than the resonance linewidth. Second, it is possible to use the grating to substantially enhance the laser diode tunability. By rotating the grating, the spectral component of the diode's gain profile fed back to the diode can be swept, resulting in a laser frequency which can be "pulled" by as much as several nm away from the diode's free running wavelength (coarse grating tuning). In addition, fine wavelength tuning is possible by changing the external cavity length, defined by the grating and the back facet of the diode chip. This is accomplished with a piezo-ceramic element (PZT) that both rotates and translates the diffraction grating (PZT tuning). The PZT tuning range is a fraction of the external cavity free spectral range (FSR). Additional wavelength control is obtainable by tuning the laser diode injection current and temperature. In fact, in order for the laser to run in a single mode of the external cavity, a proper combination of injection current, temperature and PZT cavity length adjustment is necessary. The light reflected from the grating is the ECDL output.

We have constructed three nearly identical Littrow lasers at 852 nm. These systems use a Thorlabs non AR-coated laser diodes (L850P030) and output 15-20 mW. A schematic of the design is shown in figure 3.2. The diode laser can is placed inside a commercial collimation tube containing a lens that collimates the highly diverging beam

emitted from the diode chip. The tube is housed in an aluminum rectangular holder, which is mounted on an aluminum baseplate. The diffraction grating (1800 lines/mm), providing optical feedback to the diode, is mounted on a ½" mirror mount which is also mounted on the same aluminum baseplate as the diode holder. A PZT stack properly placed on the mirror mount allows fine grating rotation and tuning of the external cavity length. Injection current to the diode is provided by a Thorlabs laser diode controller. The laser diode temperature is actively stabilized with a Thorlabs temperature controller, along with a AD590 temperature sensor mounted on the laser diode holder, and a thermoelectric cooler (TEC) placed under the aluminum base plate. This latter feature results in a temperature stabilized external cavity. This is significant because frequency drifts associated with temperature changes in the lab are virtually eliminated, leaving humidity drifts as the main cause for frequency changes. When properly tuned, the unlocked lasers never mode-hop (except during some summer days with large humidity changes).

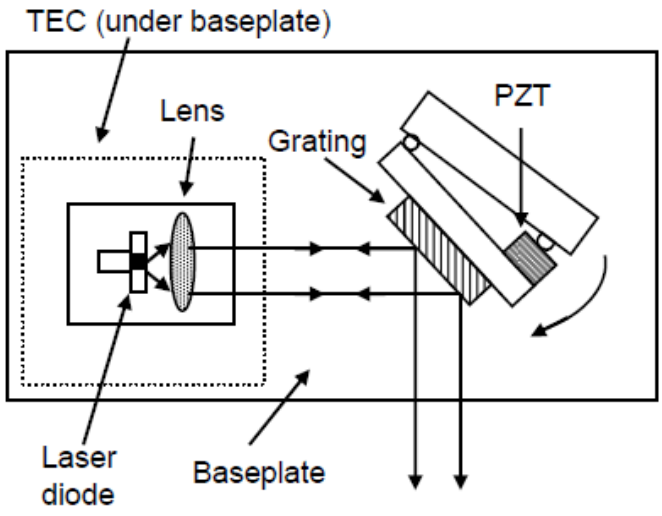

Figure 3.2: A drawing of the 852 nm External Cavity Diode Laser system

Lasers are in general very sensitive to external perturbations, and good acoustic and mechanical isolation from their environment is required to avoid unnecessary conversion of environmental noise to frequency noise. The 852 diode laser systems are housed inside ½ " thick aluminum boxes for acoustic isolation. Isolation from mechanical

vibrations coupled through the table, is provided by a layer of sorbothane placed between a massive aluminum block onto which the laser baseplate sits (also serving as a thermal heat sink for the TEC) and the aluminum enclosure. The mechanical and acoustic isolation is sufficiently good so that the lasers, when frequency stabilized, will remain locked even when objects are dropped on the optical table. The use of sorbothane creates a slight pointing instability in the lasers. With the optical table floated, the laser baseplate center of mass can shift, and change the beam direction, which is a major cause of concern. We have not needed to float the table however, and so this slight instability has not been an issue.

It is worth discussing the particular external cavity length chosen for our 852 nm lasers. The cavity length is approximately 2.5 cm corresponding to an FSR of ~ 6 GHz. This FSR is a convenient choice which is neither close to 9.2 GHz nor 4.6 GHz. This is the separation (or ½ the separation respectively) between the two hyperfine components of the Cs ground state. As discussed in [18], an ECDL operating on a particular single external cavity mode may have some power present in adjacent external modes. For lasers used to optically pump the Cs atoms, if the external mode spacing were close to 9.2 GHz (or close to a multiple of 4.6 GHz) the laser's slight multimode behavior could induce unwanted transitions that tend to cancel the pumping process. A similar issue can arise with the detection laser. In that case, transitions related to spectral impurity tend to add an unwanted background to the detected signal.

3.2.2 The 852 nm laser frequency stabilization scheme

The weak transition experiments require that the frequency of the 852 nm lasers be well stabilized to the peak of the transitions the lasers excite in the atom beam. This requirement is particularly important for the detection laser, since the frequency noise present in this laser is directly observable in the 6S→7S detection noise. Frequency stabilization involves three things: a resonance that provides a reference frequency, a scheme to obtain an error signal between the reference frequency and the laser frequency and an electronic feedback loop filter that uses the error signal to stabilize the laser frequency to the given resonance frequency. We have implemented saturated

absorption spectrometers in order to obtain Cs D_2 line resonances that serve as our reference resonances, and we have used frequency modulation spectroscopy to obtain the necessary error signals. A simple loop filter is used to stabilize the laser frequency by applying the feedback signal to the laser PZT and the laser injection current.

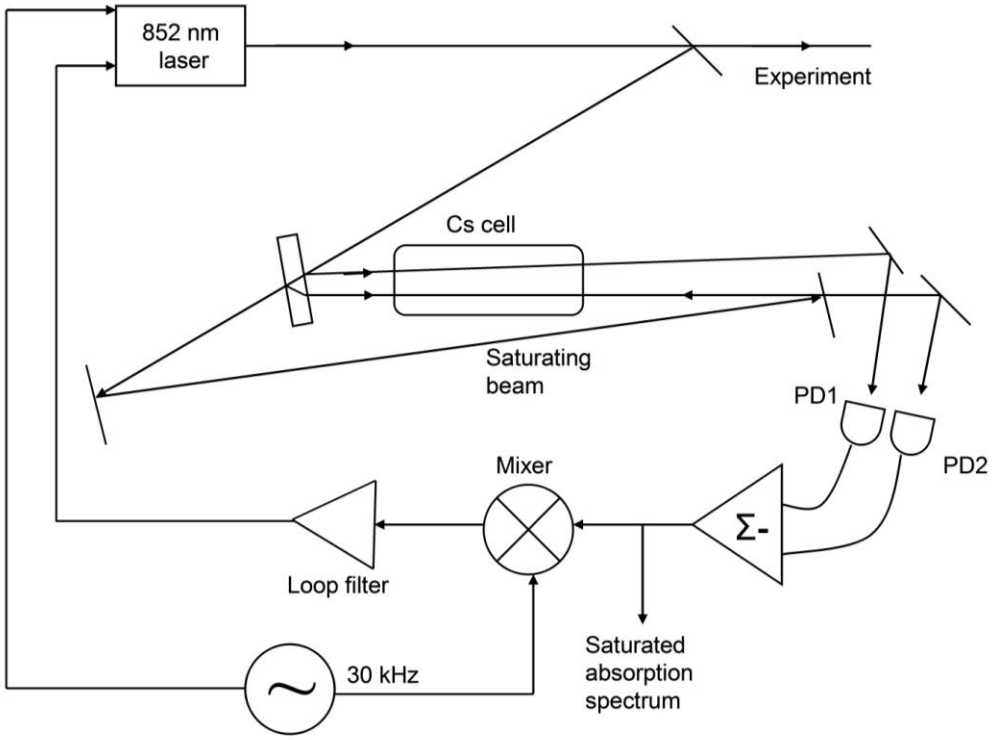

Figure 3.3: The optical setup for obtaining a saturated absorption spectrum and simplified schematic of the frequency modulation spectroscopy employed to obtain an error signal as well as the feedback loop that frequency stabilizes the 852 nm lasers.

Saturated absorption spectroscopy is a type of pump-probe spectroscopy that provides nearly Doppler-free spectra of atomic and molecular transitions in a vapor. In this straightforward-to-implement scheme (Figure 3.3) two counter-propagating beams, a strong beam that saturates a given transition called the pump, and a much weaker one, the probe, overlap inside cell containing an atomic vapor. Due to the opposite Doppler shifts seen by the atoms for the two beams, atoms only absorb from one beam or the other. The exception to this is the class of atoms with a velocity corresponding to small Doppler

shifts, within the natural linewidth of the transition. Although these atoms can in principle absorb from both beams, since the pump is saturating the transition, little probe absorption can occur. Therefore, as the laser frequency is scanned, a probe absorption measurement will show a Doppler broadened resonance with a decreased absorption at the center frequency of the transition. This dip in absorption represents the (nearly) Doppler-free resonance, and in the absence of power and pressure broadening, its width should be simply the resonance natural linewidth. The absorption signal from a second probe beam (not overlapping the pump) is subtracted from the probe signal, to provide a spectrum free of the Doppler broadened background. A typical saturated absorption spectrum for the F=4→F=3, 4, 5 component of the D_2 line is shown in figure 3.4 a).

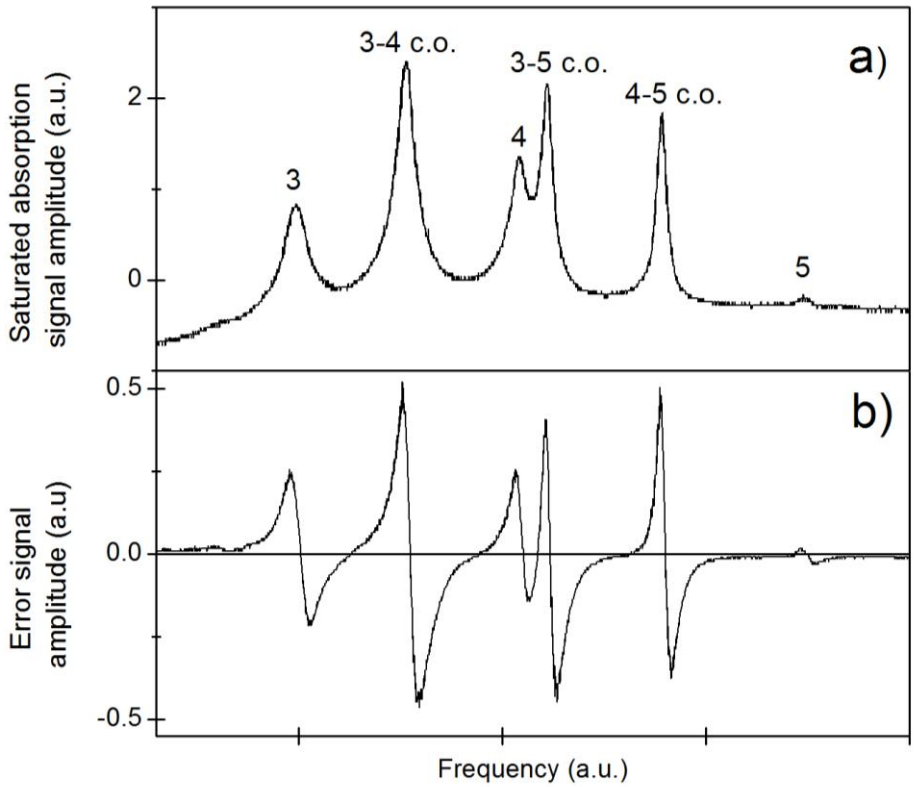

Figure 3.4: Saturated absorption spectrum obtained for the $6S_{1/2}$ F=4 → $6P_{3/2}$ F=3,4,5 transitions (a), and the corresponding error signals (b). The intermediate resonances, labeled c.o., are crossover resonances.

To obtain an error signal from the saturated absorption spectra, frequency modulation spectroscopy is employed [41]. The laser injection current is dithered at a frequency *v* of approximately 30 kHz, which imposes a small modulation on the laser frequency with an amplitude of a few hundred kHz. This modulation appears as a modulation in the saturated absorption signal when the laser frequency is on the side of a resonance. With the use of an electronic mixer, this signal is mixed with the same dither signal used to modulate the laser frequency. The mixer output has a component near the DC and a component oscillating at 2*v*. The DC component, which is proportional to the derivative of the resonance, serves as the error signal. Figure 3.4 b) shows the corresponding error signal of the spectra of Fig. 3.4 a).

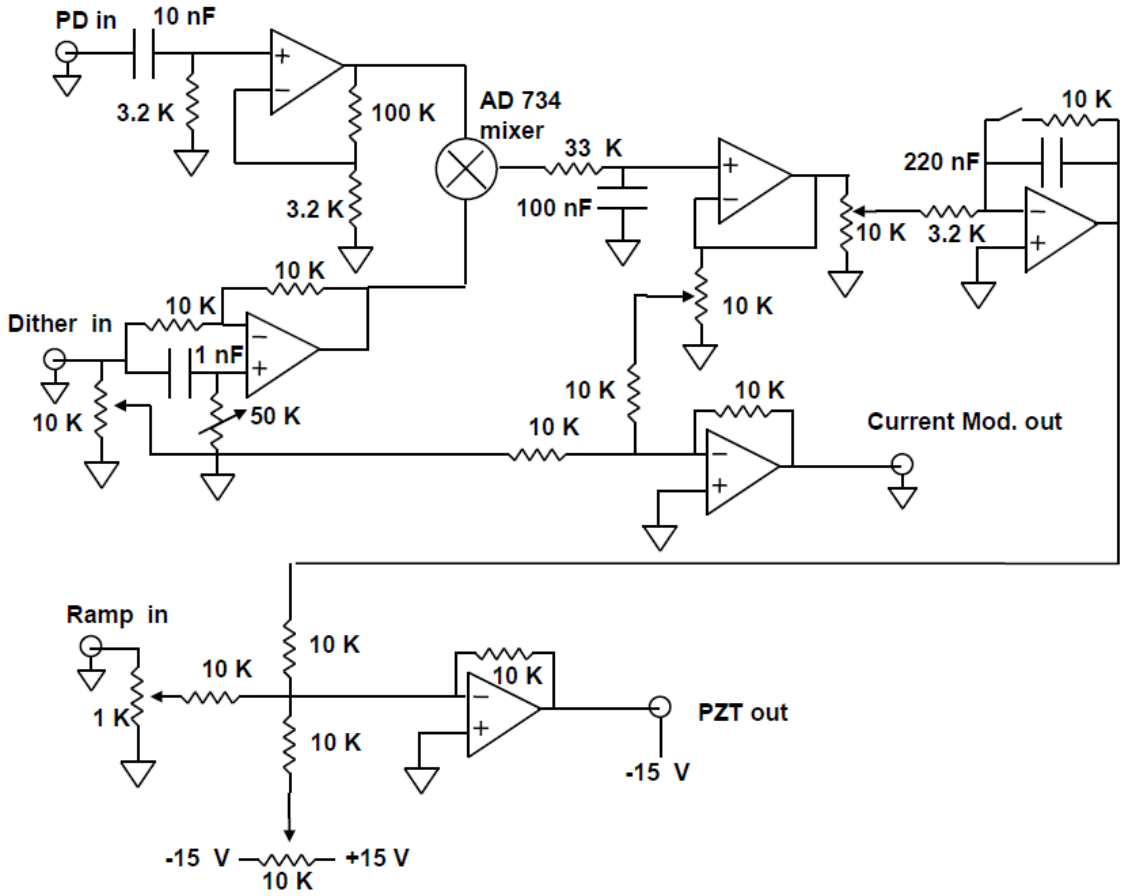

Figure 3.5: Simplified schematic of the circuit used to obtain an error signal from the saturated absorption spectrum and the loop filter used to stabilize the frequency of the 852 nm lasers. All op amps shown are OPA227.

A feedback loop filter is employed to lock the laser frequency to the peak of the saturated absorption resonance. The loop consists of two paths: a fast path, which applies the feedback to the injection current, and a slow path which provides feedback to the PZT. The fast path is essentially the error signal, has a bandwidth of 500 Hz and corrects for higher frequency excursions. The slow path consists of an op-amp integrator. The integrator has a very high gain at DC (equal to the open loop gain of the op-amp) which is needed for tight locking to the peak of the resonance. Figure 3.5 shows a schematic of the circuit used to derive an error signal as well as the loop filter that stabilizes the laser frequency

The performance of the 852 nm locking scheme has been evaluated by heterodyning two of the 852 nm lasers on a fast photodiode. These lasers were locked to adjacent saturated absorption peaks (frequency difference of 80 MHz). From the width of the peak in the photodiode's power spectrum at 80 MHz, and assuming equal linewidths for the nearly identical lasers, we estimate an individual linewidth of ~ 1.5 MHz on the 1 sec scale.

3.2.3 The 852 nm laser for Raman spectroscopy

As discussed in section 3.10, there is a need for measuring the population distributions among the various m_F levels of the F state to which the atoms are optically pumped. For this purpose we perform off-resonant Raman spectroscopy between the two components of the $6S_{1/2}$ ground state, and measure the relative m_F populations. We have constructed an 852 nm ECDL whose injection current is modulated at 4.6 GHz to provide frequency sidebands that serve as our two Raman components, needed for the spectroscopy. Alternative methods to produce a pair of coherent sources, detuned by 9.2 GHz from each other, would be either by use of a microwave-frequency Electro-Optic Modulator (EOM) at 4.6 GHz, or by phase-locking of two independent lasers,

Laser diodes are known to have significant frequency modulation capabilities, which extend to as far as a few GHz in frequency [38]. However, the modulation depth of a typical laser diode at the required frequency of 4.6 GHz is very small. Fortunately, it is possible to take advantage of the optical feedback in an ECDL in order to enhance the

effect of the modulation and obtain appreciable laser sidebands in the microwave regime. The requirement to achieve this is that the external cavity FSR matches the desired modulation frequency. In this case, the small amplitude sidebands produced by the laser diode, are fed back to the diode and get amplified since the corresponding fields can resonate inside the external cavity, and because of the inherent sensitivity of the laser to optical feedback. The laser can be thought of as lasing in three adjacent external cavity modes (carrier and the two 1st order sidebands), and these modes are phase locked to each other.

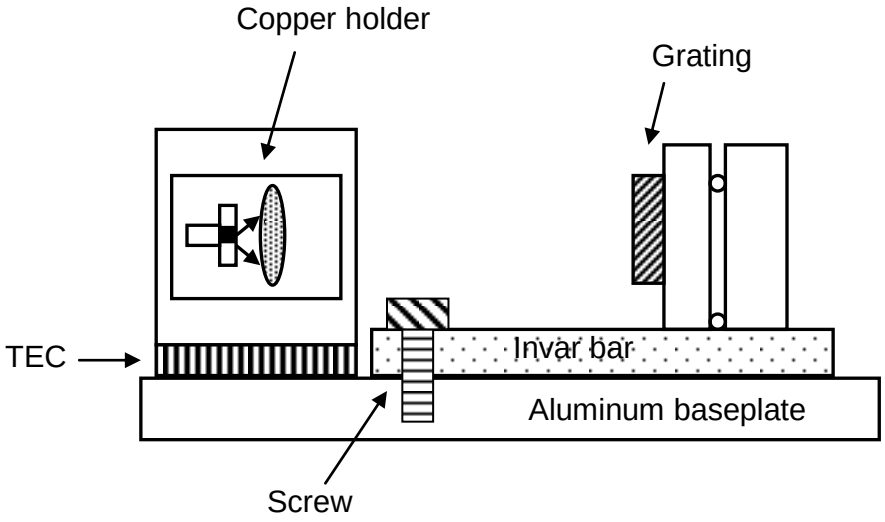

Figure 3.6: Schematic of the Raman laser design

The 852 nm Raman laser is similar in design to the 852 nm ECDL described in (3.2.1). There are two distinctive differences however. The first is the longer external cavity length, ~3.3 cm, that corresponds to the required FSR of 4.6 GHz. The other difference is a change that enhances the temperature stability of the laser diode. In particular, the holder that houses the tube containing the laser diode and the collimating lens is mounted directly on the TEC, which is in turn in contact with the cavity baseplate (figure 3.6). This way the feedback loop that stabilizes the diode temperature can respond faster and handle temperature shifts better. The shifts are caused by small changes in the microwave power coupled to the diode, occurring as the microwave frequency is scanned. The drawback of this approach is that the cavity baseplate now acts as the TEC

heat sink, and so to improve long term stability, the grating mount is mounted on a small invar bar, such that temperature drifts of the aluminum baseplate have little effect on the external cavity length.

The microwave electronics used to produce the 4.6 GHz sidebands consist of a tunable voltage controlled oscillator (VCO) of this frequency, followed by three consecutive amplifiers, and a bias-tee which combines the DC injection current and the microwave signal. The microwave power at the output of the bias-tee is ~ 16 dBm. The actual power coupled to the diode is not known, and is most likely only a small fraction of the 16 dBm. Most of the power is expected to reflect back, due to impedance mismatching. This does not seem to matter though. As it can seen in the Raman laser spectrum of figure 3.7, slightly more than 50% of the total power can be put into the 1st order sidebands, which is sufficient for the Raman spectroscopy.

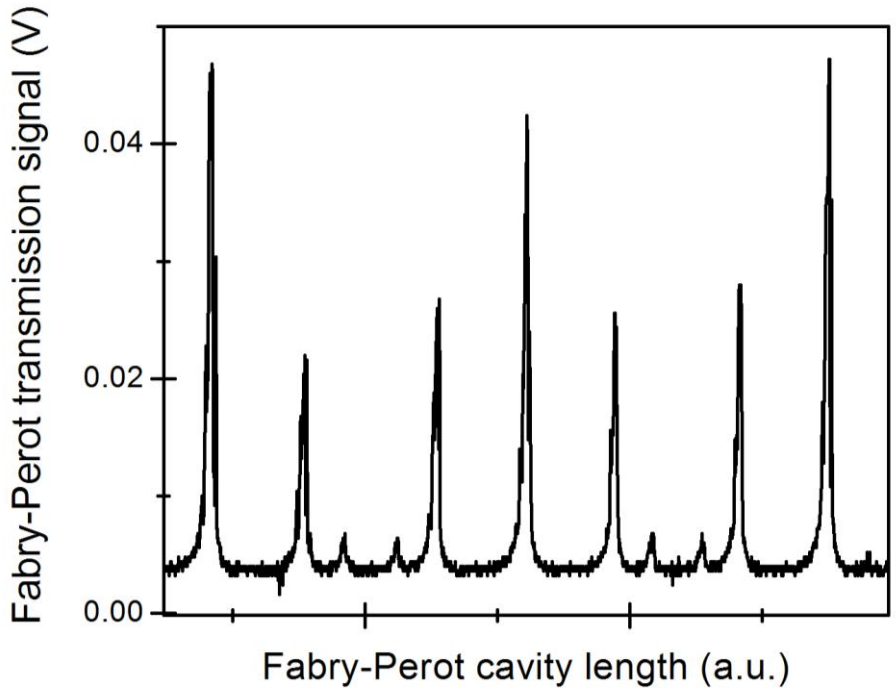

Figure 3.7: 852 nm Raman laser spectrum. The largest amplitude peaks correspond to the laser carrier, the intermediate amplitude peaks are 1st order frequency sidebands at 4.6 GHz and the smallest amplitude peaks are 2nd order sidebands. The total fraction of power in the 1st order sidebands is ~ 50%. The spectrum was obtained with a 300 MHz scanning Fabry-Perot spectrum analyzer.

The off-resonant Raman spectroscopy requires that the frequencies used to transfer the m_F populations from one component of the ground state to the other be off-resonant from the $6P_{3/2}$ transition, so that population is not excited to the $6P_{3/2}$ state. In the scheme we have implemented, the high frequency 1^{st} order sideband of the Raman laser is frequency stabilized to a frequency 160 MHz below the F=3→F=2 transition frequency (see figure 3.22). To achieve this, the laser output is passed through an AOM and the frequency up-shifted beam is sent to a saturation absorption setup, where the high-frequency sideband of the laser is locked to the F=3→2 transition. The loop filter used for locking the laser is identical to the one described in (3.2.2). The un-shifted beam is used in the actual experiment. We show a schematic of the Raman laser system in figure 3.8.

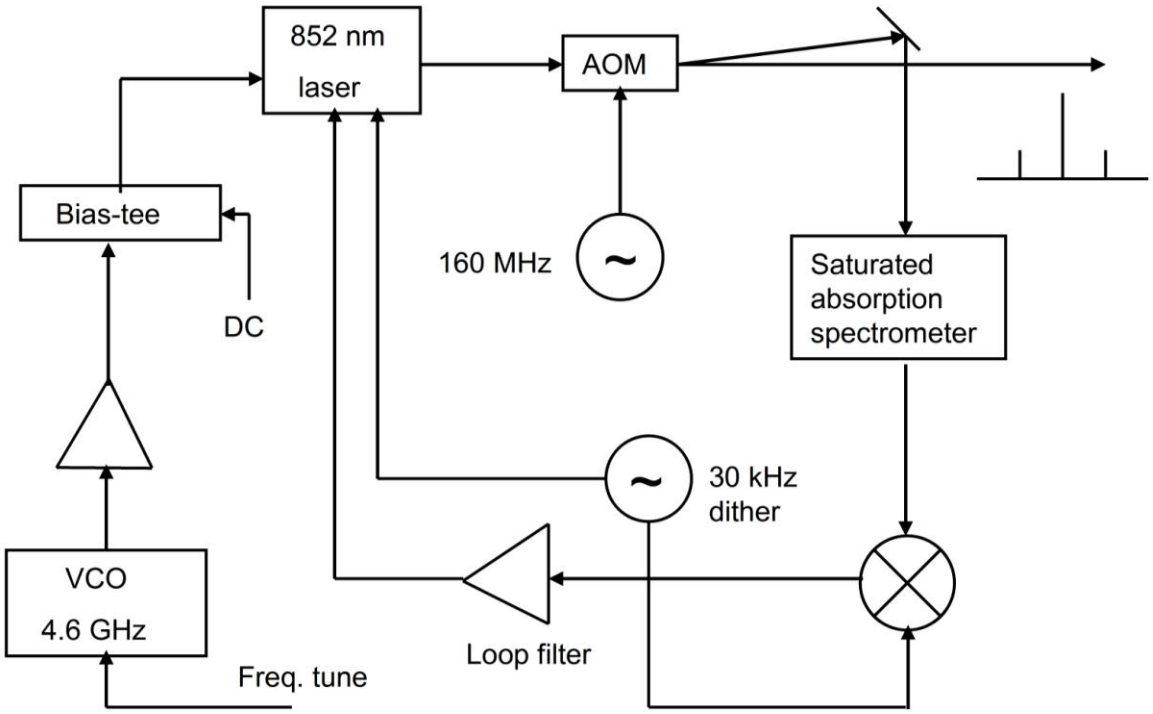

Figure 3.8: Schematic of the setup for obtaining frequency sidebands at 4.6 GHz from an 852 nm ECDL, with a 160 MHz frequency offset from the D_2 line resonance frequencies.

3.2.4 The 1079 nm ECDL system

The two-photon 6S→7S excitation in the weak transition experiments requires a laser at 1079 nm. The available source needs to output as much power as possible, in order to obtain a large SNR in the 6S→7S rate, and also a high efficiency for the second harmonic generation at 540 nm. Advances in rare earth doped fiber amplifier technology have made high power IR amplifiers commercially available, with outputs that may reach as much as 50 W in the IR range. We have acquired a Keopsys fiber amplifier, capable of outputting ~ 12 W at 1079 nm, and we have constructed an ECDL at 1079 nm to seed the amplifier. The option of purchasing a commercial laser system to seed the amplifier was also considered, but the homebuilt approach is considerably less expensive and offers greater versatility than a commercial system.

The 1079 nm laser is of the Littrow type and its design is very similar to that of the 852 nm lasers described in (3.2.1). The laser diode is from QPhotonics, capable of producing about 80 mW of light in the external cavity configuration. The diode has an AR-coating on the front facet, with a specified 2% reflectivity. There are two features of the 1079 laser that differ from the 852 nm design: the grating resolution (1200 lines/mm instead of 1800 lines/mm) and the cavity length (4 cm, compared to 2.5 cm for the 852 nm lasers). It is desirable to use a grating with as high a resolution as possible, since the larger the resolution, the narrower the laser linewidth [42], but the 1800 lines/mm grating of the 852 nm lasers has a very poor diffraction efficiency at 1079 nm, so a lower resolution grating had to be used. The longer cavity length was chosen because it is known to result in a lower ECDL linewidth. This can be explained in terms of the higher spectral purity for light fed back to the laser diode, obtained for a larger diode-grating spacing. The narrow 1079 nm linewidth is needed in order to reduce frequency noise in the 6S→7S excitation rate. A very long cavity length on the other hand reduces the tunability and thus the 4 cm cavity length is a compromise between the competing requirements for low linewidth and decent tunability. The ECDL free spectral range is about 3.5 GHz with a single mode frequency scan range of ~ 1.5 GHz.

3.2.5 The 1079 nm laser frequency locking scheme

The 1079 nm ECDL needs to be frequency locked to the Cs 6S→7S resonance, and the lock has to be tight enough so that the frequency noise on the laser does not add substantially to the 6S→7S transition frequency noise. The error signal required for locking can be obtained from either the atom beam, or from a Cs cell. If the laser is to be locked directly to the resonance, in order to obtain an error signal, the frequency needs to be dithered in the acoustic region, typically between 5 and 50 kHz (~30 kHz for the 852 lasers). Due to bandwidth limitations of the 6S→7S detection scheme in our atom beam apparatus, (see section 3.14), detecting a kHz-type modulation on the resonance is not possible. This leaves the Cs cell as the only option for locking. However, there are quite a few advantages for using this. First, the two-photon transition in the cell can have a very narrow linewidth (narrower than that of the atom beam). This is possible by employing counter-propagating laser fields to drive the two-photon transition. In this configuration, atoms can absorb a single photon from each beam and become excited with the same probability, regardless of their velocity class. This occurs since the net Doppler shift $\vec{k}\cdot\vec{v}+(-\vec{k})\cdot\vec{v}$ in the atom frame is zero. Doppler broadening is thus eliminated and the resonance width is nearly natural linewidth limited. For the purpose of locking, a narrow resonance is desired, since it results in an error signal with a steep slope, which is an obvious requirement for a tight lock. In our apparatus, the linewidth in the cell is two times smaller than that of the atom beam (7 MHz and 14 MHz, respectively). In addition to a steeper error signal, a cell allows a higher SNR to be obtained for the error signal, since the available atom density can be much greater than that of an atom beam, and also because of the higher optical intensity available (due to the ability to focus the beams tighter).

The frequency modulation technique and electronics used to derive an error signal from the cell and lock to the 6S→7S resonance peak have been described in (3.2.2). We show a schematic of the relevant setup in figure 3.9. Compared to the 852 nm locking scheme, the main difference is the method by which the resonance is obtained, the two-photon Doppler-free spectroscopy in this case. A small fraction of the fiber amplifier output (~4% or ~ 450 mW) is picked off by a beam sampler and is directed to the vapor

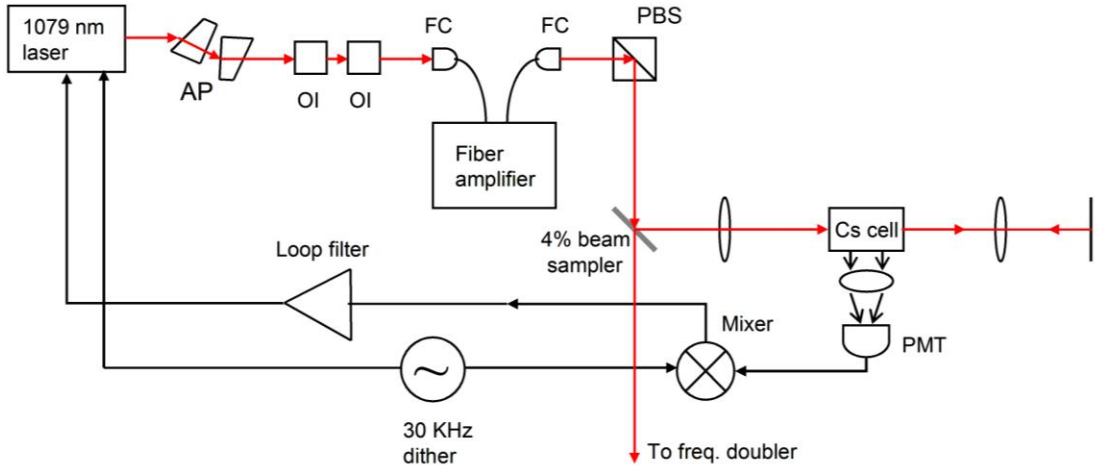

Figure 3.9: Simplified schematic of the 1079 nm setup for obtaining an error signal and locking to the 6S→7S two-photon transition. Abbreviations: OI: Optical isolator, FC: Fiber coupler, PBS: polarizing beam splitter, PMT: photomultiplier, AP: Anamorphic prisms.

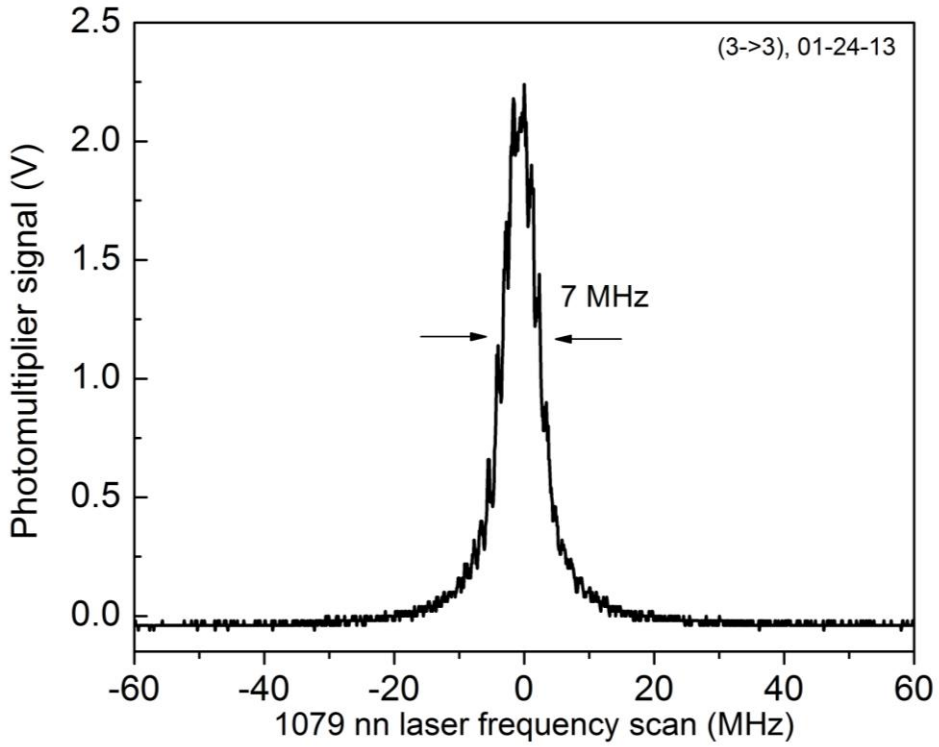

Figure 3.10: The $6S_{1/2}$ F=3 → $7S_{1/2}$ F=3 two-photon resonance, obtained by scanning the 1079 nm laser.

cell. The beam is focused using a 15 cm lens, resulting in a ~ 60 μm waist (radius) at the center of the 8 mm long cell, housed inside an aluminum enclosure. Upon exiting the cell, the beam passes through a second lens, and gets focused on a retro-reflecting mirror, retracing its path back to the cell. The beam retro-reflection results in a Doppler-free resonance. A spectrum of this resonance is shown in figure 3.10. A photomultiplier (PMT) collects (through a lens) some of the 852 nm fluorescence, emitted by atoms decaying to the ground state through the $7S_{1/2} \rightarrow 6P_{3/2}$ channel (~67% branching ratio). An 852 nm interference filter placed in front of the PMT cathode, blocks any unwanted light. The cell has a cold finger which is heated at ~ 70 ^{o}C (with the main body heated at a higher temperature), enough to produce a very large PMT photocurrent.

3.3 The 1079 nm second harmonic generation

The one-photon pathway of the 6S→7S excitation is driven by light at a frequency which is twice the frequency of the 1079 nm field driving the strong two-photon pathway. In order to be able to control the interference of the two pathways, phase coherence between the two fields is required. To ensure phase-coherence, the 540 nm field is produced by second harmonic generation of the 1079 nm light, which is a coherent process. In addition to the coherence requirement, the available 540 nm power has to be as high as possible, in order to obtain a strong modulation in the 6S→7S rate. In our apparatus, we use a Magnesium-oxide doped, periodically-poled $LiNbO_3$ crystal (MgO:ppLN), to perform second harmonic generation with quasi-phase matching [44]. With a single-pass of ~ 11 W of IR through the crystal, we generate ~ 1 W of green power. This level of power is adequate for the M_1 experiment. The observed conversion efficiency level agrees with an estimate based on the theory of Boyd and Kleinman [43].

The ppLN crystal (purchased from Covesion) is 20 mm long and contains five periodically poled sections, each with a different poling-period, so that quasi-phase matching can be achieved in the range 1058-1080 nm. The crystal is housed in a commercial oven assembly, which allows active temperature stabilization of the crystal in the range of 20 to 220 ^{o}C. The crystal faces are AR-coated with a specified residual

reflectivity of less than 0.5 % for both the IR and green light. With temperature tuning at ~210 ^{o}C we achieve quasi phase-matching conditions at 1079 nm. Because of the narrow cross-section of the periodically-poled region (0.5 x 0.5 mm), proper alignment of the fundamental beam through the crystal is necessary. For this, the crystal is mounted on a rotation stage, which is mounted on a mirror mount, and the mirror mount is in turn attached to an X-Y-Z translation stage. With so many degrees of freedom, alignment is easy. Using a 12.5 cm lens, the 1079 nm beam is focused to the crystal, with a waist of approximately 45 μm at the crystal center. A tighter focus yields higher conversion efficiency, but this is not without trouble for our experiment. We believe that heating in the crystal is responsible for slight instabilities in the modulation measured on the 6S→7S rate, as discussed in section X, and therefore a higher IR intensity in the crystal would probably increase the level of these fluctuations. Upon exiting the crystal, the green and IR beams are incident on a collimating silver-coated mirror. We show a schematic with the relevant optical setup in figure 3.11.

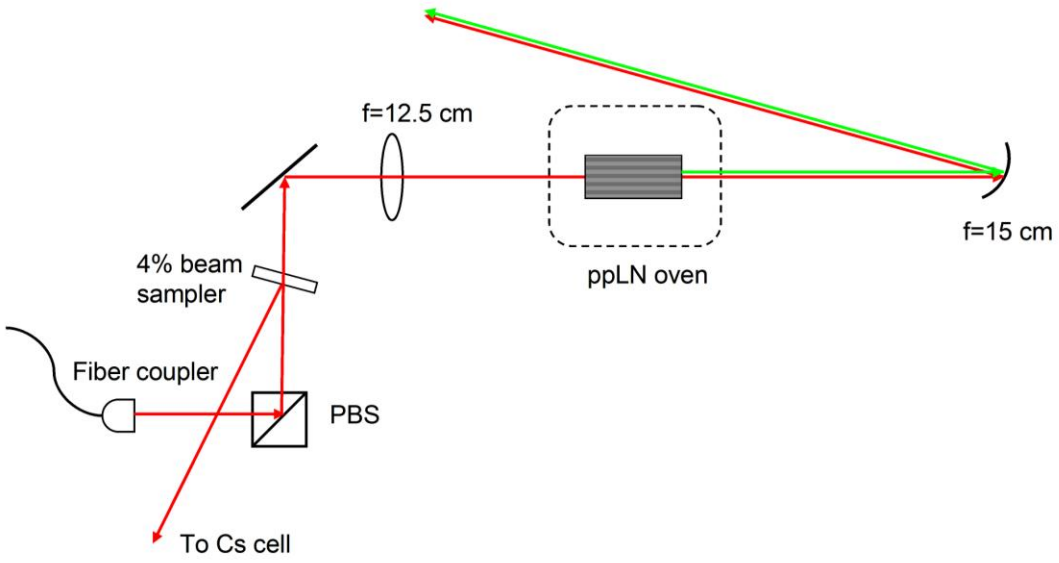

Figure 3.11: Optical setup for frequency doubling of the 1079 nm beam with the ppLN crystal.

Careful optimization of the alignment is required in order to obtain the optimum conversion efficiency and at the same time retain a nice circular beam shape for the green and IR beams at the crystal output. It was observed in several instances that while

tweaking the crystal position, the two-photon signal level in the atom beam can drop by as much as a factor of two, while at the same time the fundamental power directed to the atoms remains unchanged. We attribute this to IR beam distortion due to poor alignment through the crystal. The alignment optimization is as follows: Initially, the crystal is aligned such that the produced second harmonic beam, when observed far away from the crystal location, looks circular (a dichroic reflector can be used to separate the green output from the fundamental). This can be done at low IR input. Then, the IR power is increased to the maximum level available. This will create a slight thermal lensing effect in the focusing lens, which changes the position of the focus in the crystal, making it necessary to translate the crystal closer to the lens to re-optimize the focus position. In addition, the increased IR intensity in the crystal causes some heating, and so the crystal temperature needs to be reduced slightly to obtain optimum power. With proper alignment, the conversion efficiency remains high for long periods of time (weeks), and only a slight temperature optimization may be necessary from day to day.

3.4 Vacuum chamber construction

The vacuum chamber that houses our Cs beam was designed with a few key considerations. First, it is large enough to fit all the necessary magnetic field coils, electric field plates, cryo-baffles and other components that may be required for the future PNC experiments. Its dimensions are 55x50x40 cm. Second, unlike most vacuum chambers, it was made from aluminum, as part of an effort to maintain stray magnetic fields in the interaction region to as low a level as possible. This requirement is more stringent for the PNC measurements. Third, several pairs of optical windows were included that allow passage of multiple beams through the chamber. In total, there are four pairs of 2” windows with AR-coating at 852 nm and one pair of 1” windows with dual-AR 1079-540 nm coating. Lastly, it was designed with a (heavy) lid at the top that can be removed easily, so that whenever needed, access to the chamber interior can be easy and quick. A long o-ring running along the top of the chamber walls forms a vacuum seal between the lid and the chamber. A drawing of the vacuum chamber is shown in figure 3.12.

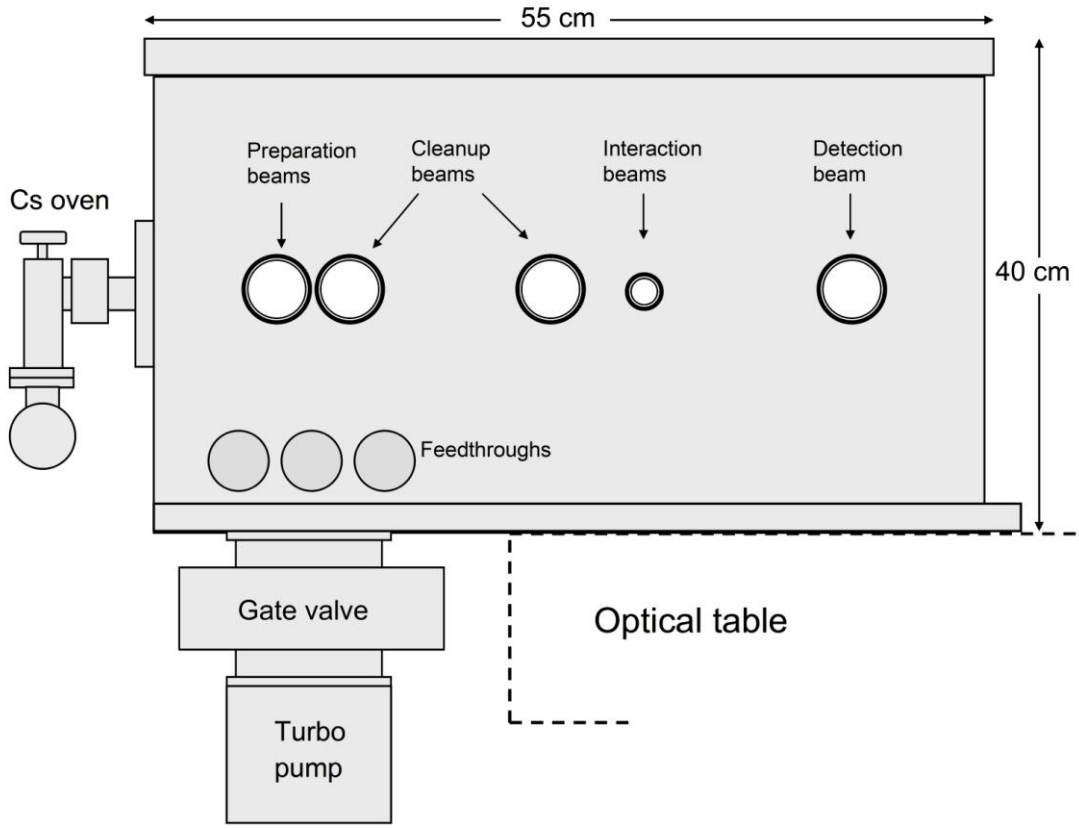

Figure 3.12: A drawing of the vacuum chamber for the weak transition experiments

The chamber is pumped by an Edwards STP-451 turbopump (pumping speed 480 L/sec) which is magnetically levitated and advertised to have very low levels of vibration. The DC and AC magnetic fields produced in the pump that reach the interaction region are negligible. The pump is backed by a 200 L/sec roughing pump. A pneumatic gate-valve installed between the turbopump and the chamber allows venting the chamber to atmosphere (e.g. when work needs to be done in it) without having to stop the pump. This avoids frequent acceleration/breaking of the pump that tend to decrease its life time. The system has a base pressure of $2.5 \cdot 10^{-6}$ Torr. This level is low enough so that the fraction of atoms in the Cs beam that collides with background gas and is lost from the beam is small (~2%). After initial pumping to the tens of milliTorr range with the roughing

pump, the turbopump can be allowed to pump the chamber. It takes approximately 24 hrs for the system to reach its base pressure, but this time can vary, depending on how long it has been left exposed to atmosphere.

A pair of Liquid Nitrogen-cooled baffles is installed in the chamber to reduce Cs clouding that could otherwise create issues in the optical pumping and detection of Cesium atoms. In addition, the baffles act as secondary pumps for the chamber, contributing a reduction of the pressure by ~($0.2 \cdot 10^{-6}$ Torr). Each baffle is a large copper plate with a small stainless steel tank attached to its surface. The baffles are placed on opposite chamber walls. The first is close to the Cs oven, and has an aperture 10 mm wide x 3 mm high) that defines the shape and dimensions of the atom beam. The other is at the end of the atom beam path. A resistor-based temperature sensor inside one of the tanks provides an estimate of the nitrogen level. It takes approximately 60 minutes for the LN_2 to completely evaporate, once the tanks have been filled. Refilling is done from a large LN_2 tank, through a vacuum feedthrough, when a relay-controlled pressure valve is switched on. Due to the slight pumping capability of the cryo-baffles, refilling needs to be done within ~ 30 minutes after LN_2 has completely evaporated, or else the pressure will slightly rise, and cause a small (but observable) reduction in the beam density.

3.5 The Cesium Oven

The Cs beam of our apparatus effuses from an oven constructed of (mostly) readily available vacuum components, and mounted on one of the vacuum chamber walls. As with many other oven designs, this oven consists of two sections, one containing a Cesium ampoule and another maintained at a higher temperature and fitted with a nozzle through which the atoms effuse and form a beam. The atom density in the beam is primarily determined by the temperature of the coldest section of the oven, and the atomic velocities of the beam by the temperature of the nozzle section. Figure 3.13 is a drawing of the oven.

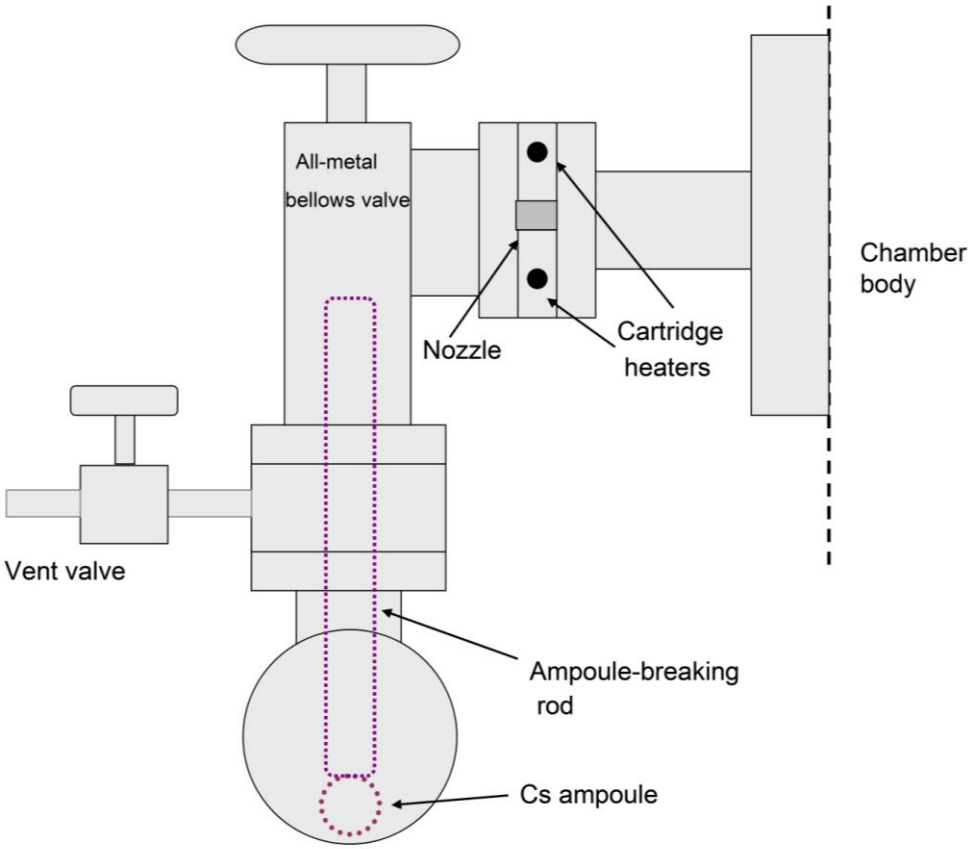

Figure 3.13: A drawing of the Cesium oven

The oven design was adapted from [45]. It consists of a CF 2.75" tee which holds a Cs ampoule and is held at ~120 ^{o}C, and an all-metal bellows valve which forms the high temperature section of the oven (~150 ^{o}C). The two sections are heated with rope heaters, covered by aluminum foil layers. A 2.75" CF blank flange attached on one end of the valve, machined with a rectangular-shape bore (~ 1.2 cm wide, 8 mm high), is fitted with ~100 stainless steel hypodermic needle tubes (1 cm long, 0.8 mm inner diameter), that form the oven nozzle. Atoms effusing from the oven form a dense and relatively collimated beam. The authors of [45] report a density of 10^{10} cm^{-3}, with a very similar nozzle and the same oven temperature as ours. A pair of cartridge heaters placed into bores in proximity to the nozzle, help maintain the nozzle hotter (~170 ^{o}C) than all other oven sections, in order to prevent clogging with Cs. For the same reason, some heating is

applied to the nozzle even when the system is not operated. After one year of operating the system, no signs of nozzle clogging have been observed.

The Cs oven was designed so that the Cs ampoule can be broken safely under vacuum. This is done with the bellows valve and a stainless steel rod placed inside the oven. When the valve is rotated clockwise (i.e. tends to shut), the rod presses against the ampoule and breaks it. With the ampoule broken, the valve can fully shut and isolate the oven from the vacuum chamber, which is useful whenever it is necessary to open up the chamber. If the chamber is to be left un-pumped for long times, in order to prevent Cs oxidation, the oven can be pumped with another roughing pump through an auxiliary vent valve.

Power is supplied to the oven heaters from a pair of DC power supplies. Once the supplies are on, it takes about two hours for the Cs density to stabilize. After this point, the density remains quite stable, with drifts of ~ 1-2 %/hour, which are low enough so that active temperature stabilization of the oven is not necessary.

3.6 Magnetic fields for the optically pumped Cs beam

The state preparation of the Cs beam, the 6S→7S excitation and the subsequent detection of interacting atoms require different DC magnetic fields in their respective regions. A comprehensive discussion of the magnetic field requirements for the optically pumped beam can be found in C. Wood's thesis [18]. We have followed his approach and have constructed several pairs of magnetic field coils which produce the desired fields for our experimental conditions. The field requirements for our experiments are quite similar to the ones of the Boulder PNC experiment.

In the optical pumping region (OP), the field is approximately 2 G, parallel to the direction of the pumping beams (y). This orientation is necessary in order to induce either Δm_F=+1 or -1 transitions and drive the atomic populations to an extreme m_F with the Zeeman laser. Then, as atoms travel downstream, the field slowly rotates and increases in magnitude, until the atoms reach the interaction region, where the field is 7G in the z-direction. This field defines the quantization axis in the region. Then, as atoms

approach the detection region, the field quickly decreases and reaches a smaller value (approximately zero or ~ 2 G) in the detection region.

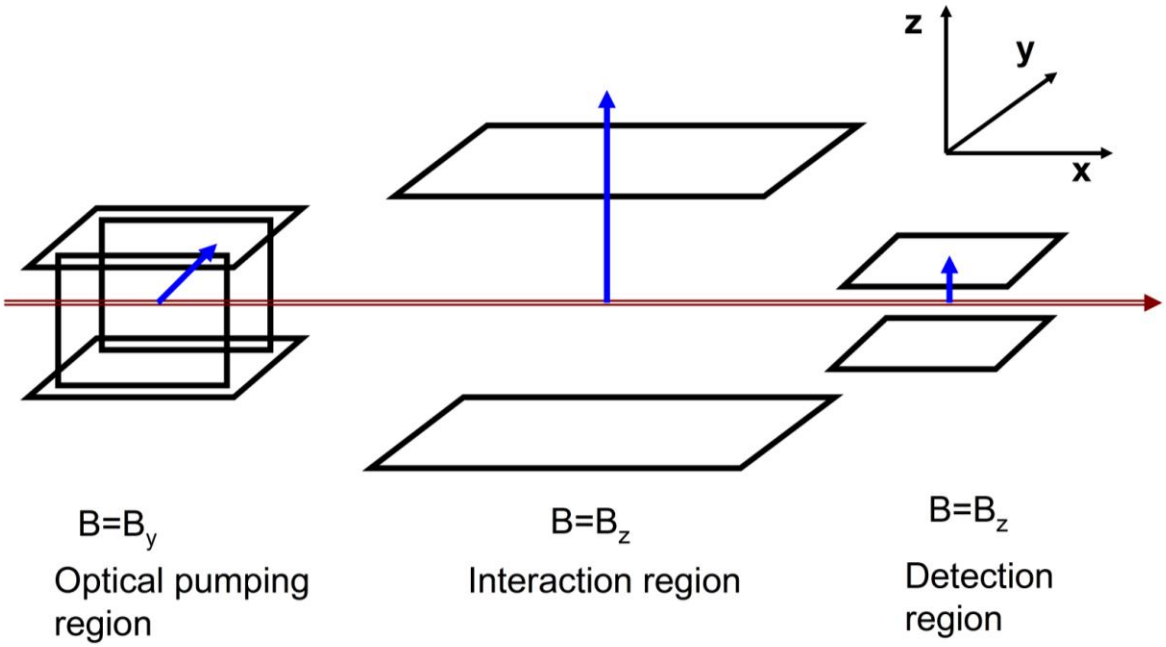

Figure 3.14: A drawing of the magnetic field coils inside the vacuum chamber

We have used a total of seven pairs of magnetic field coils in order to obtain the required fields. Three of these pairs are external to the chamber and are primarily used to cancel the Earth's field as well as the field from the optical table. These coils are centered on the interaction region, and due to the chamber size, their respective fields exhibit a variation between this and the other regions of interest. This however does not create issues. The other four pairs are inside the vacuum chamber, centered on the optical pumping, interaction or detection region. Fig 3.14 is a drawing of these coils. In the OP region, a pair creates a field in the y- direction. A second pair is used to cancel the leakage of the interaction region coils into the OP region. Around the interaction region, a large coil set produced the 7 G field in the z-direction. Lastly, the detection set of coils is used to cancel the field leaking into this region from the interaction region pair, and also to apply an additional field if necessary. These coils are narrow in the x-direction, in order to limit the extension of the produced field into the interaction region.

The interaction region coils are as large as possible with a spacing which is also large. The coils are 25x25 cm squares, spaced by 25 cm. This size requirement follows from the need for a slowly varying field (and free of zero-crossings) that the spin-polarized atoms experience as they travel from the OP to the interaction region. Under such conditions, their spin precession axis adiabatically follows the magnetic field rotation, and spin polarization is preserved. The optimum field then, has to extend as far away as possible from the interaction region, and even leak into the OP region, which leads to a choice of large size coils.

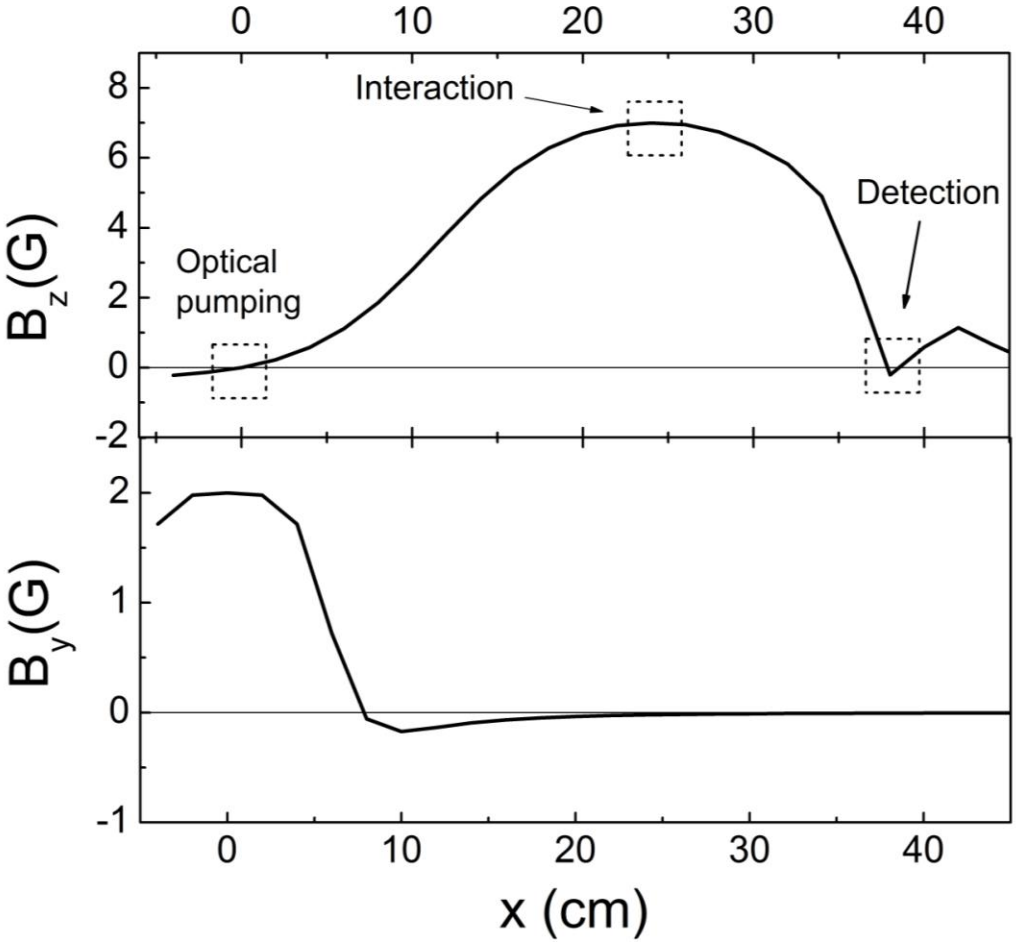

Figure 3.15: Computed z- and y- components of the net magnetic field produced by the coils inside the vacuum chamber

We show a simulation of the net z- and y- field components, produced by all coils internal to the chamber, in figure 3.15. The field was evaluated at different points along the atom beam path (around which all coils are centered), using a Mathematica code that computes the Biot-Savart law integral. The field simulations also provide an estimate for the expected variation of B_z within the ~ 1.5 cm interaction region, which is ~ 1% or better. There is a small (~40 mG) B_y field in the interaction region, as shown by the simulations (and as measured), produced by the OP coils, which is nulled using the external y-pair of coils. The measurements of the B-fields are performed with a laboratory Gaussmeter.

3.7 Electric field plates for the M_1 experiment

The M_1 as well as the future PNC experiment employ a Stark-induced transition in order to calibrate the magnitude of either the M_1 or the PNC transition. A DC electric field is therefore required in the interaction region. For the experimental geometry of the M_1 measurements, this field is applied along the y-axis, parallel to the propagation direction of the 1079 and 540 nm beams, driving the two 6S→7S transition pathways. Its magnitude is variable between zero and several times the equivalent M_1/β electric field (~ 30 V/cm). The electric field plate geometry has to be such that the E_y field is uniform in magnitude along the interaction region length. In addition, small off-axis components (x- and z-) present due to field non-uniformity need to be kept below the 10^{-3} level.

We have constructed a field plate assembly that provides the required electric field. Figure 3.16 is a drawing of the plate geometry. Each plate is a square aluminum plate, with a very flat surface (surface variations ~ 25 μm). The plate inner surfaces are coated with Aquadag, as an effort to reduce stray fields, that can result from charge accumulating on the plate surface. A small hole at the center of each plate allows passage of the 1079 and 540 nm beams through the plates. A circular basin machined on the external plate surface, concentric with the laser beam hole, helps to decrease the field fringing in the vicinity of the holes, and therefore to increase the field uniformity in the interaction region. Since the vacuum chamber surfaces (which are the boundary conditions for the electric field) are grounded, in order to avoid possible asymmetries in

the field, the voltage between the plates is applied symmetrically (± V/2). The plate separation is large enough such that the ~ 1.5 cm wide Cs beam propagating in between the plates along the x-direction does not coat the plates. We do not use spacers to set the plate separation. A prior plate assembly with nylon spacers resulted in large stray fields, observed through two-photon and Stark-induced interference at zero plate voltage! We attributed the unwanted signal to charge accumulation on the spacer surfaces, because after removing the spacers from the assembly, the zero-field interference signal did not reappear.

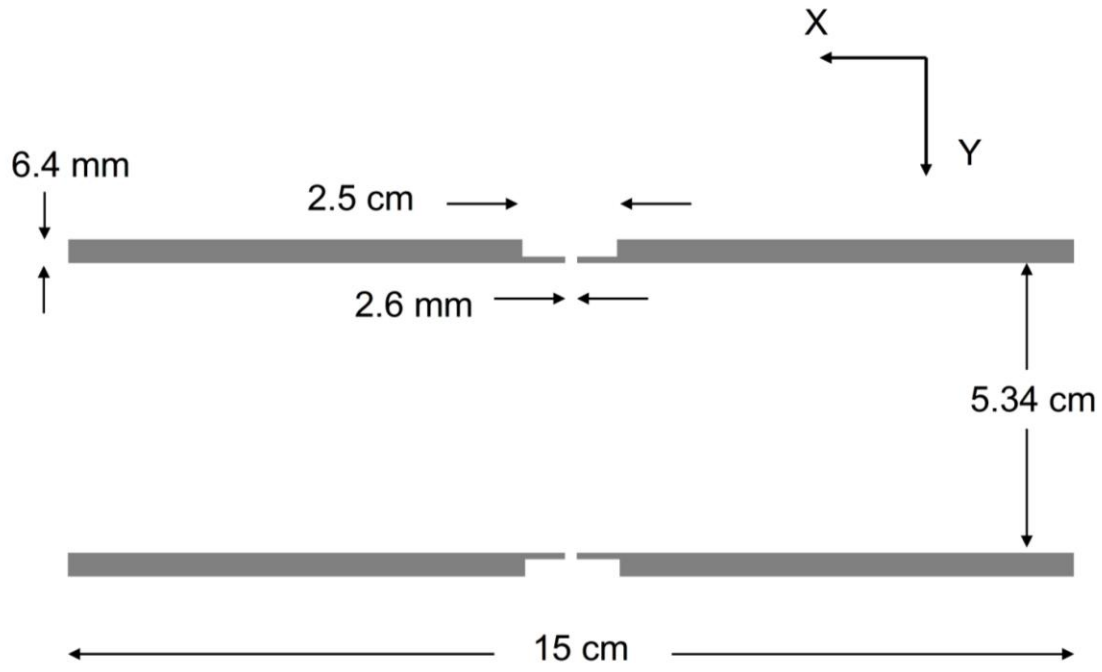

Figure 3.16: A sketch of the electric field plates used in the M_1 experiment

A uniform plate separation is essential in order to obtain a uniform electric field. In order to align the plates and ensure spacing uniformity, each plate is mounted on a JILA-type optical mount, with a glass insulating spacer between the plate and mount. The mount knobs allow precise adjustment of the plate orientation. The spacing uniformity is achieved by iteratively adjusting the individual plate orientation, until the plate spacing (measured at four different points with a caliper) reaches the desired uniformity. With this procedure, the plate separation was set to 5.338(7) cm, with the uncertainty including

the caliper tolerance (~ 50 μm). After the end of the M_1 experiment, the plates were removed from the chamber and the spacing was re-measured with the same caliper and found to be consistent with the initial measurement to within 5 μm.

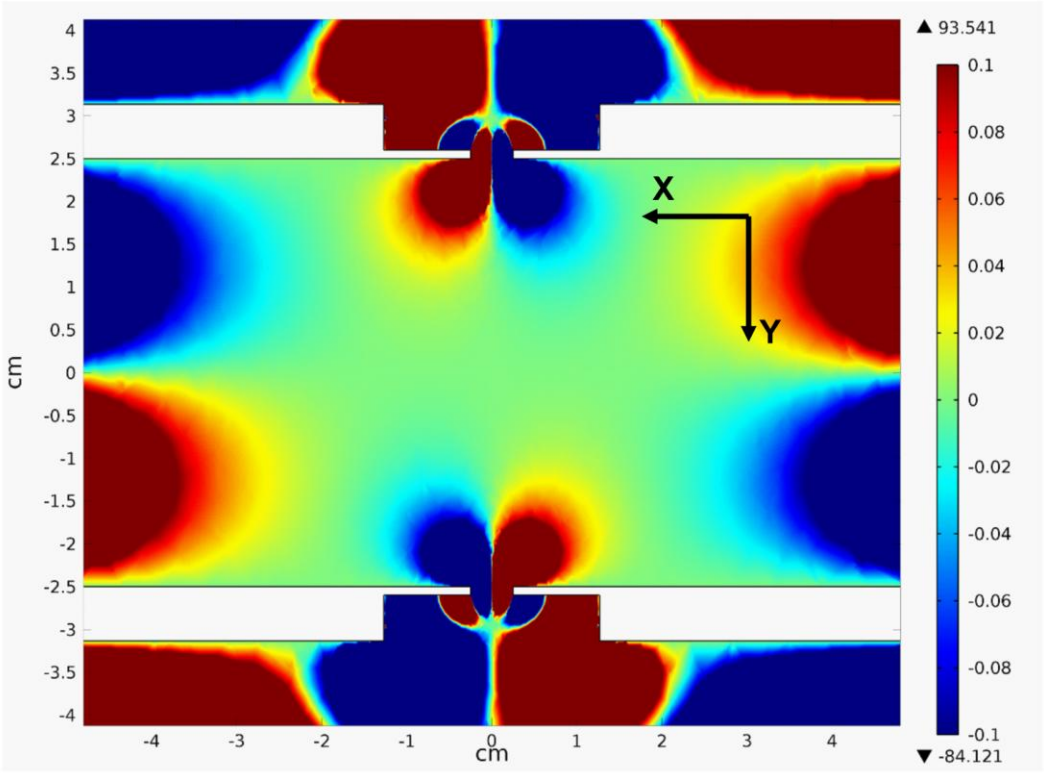

Figure 3.17: Contour plot of the x-component of the electric field produced by the field plates, due to fringing. The main electric field component is E_y=40 V/cm.

We have studied the possible electric field non-uniformity due to the presence of the two laser beam holes in the plates or due to fringing owing to the finite ratio of plate size to plate spacing. This was done with COMSOL simulations of the electric field between the plates. The region of particular interest in the field plate model is the interaction region, which is the central 1.5 cm section between the holes. The grounded vacuum chamber is included in the simulation, serving as the boundary surface for the model. We show a contour plot of the x-component E_x, arising from field-fringing. The primary field is E_y=40 V/cm for this model (with the voltage applied symmetrically to the

plates) and we can estimate a value of 0.01 V/cm for E_x in the interaction region, that corresponds to a ratio E_x/E_y of approximately $2.5 \cdot 10^{-4}$. This non-uniformity level is well within our tolerances for the M_1 experiment. The actual E_x/E_y (and E_z/E_y) ratio is determined by the orientation precision of the 540 nm beam (which defines the y-axis of the coordinate system) relative to the field produced by the plates.

3.8 Optical pumping of atoms

The interference of the two-photon and the weak (M_1, E_{PNC} or β-Stark) amplitude for particular $(F,m_F) \rightarrow (F, m_F)$ transition results in a cross-term in the overall transition rate, whose amplitude and sign depend on the value of the particular m_F value (this is because the weak amplitudes themselves are proportional to m_F, see section 2.3.1). This means that with a uniform distribution among the Zeeman sub-levels, there will be no interference observed, because transitions involving opposite m_F states contribute with opposite signs to the overall 6S→7S excitation rate. It is therefore necessary to spin-polarize the atoms. For this, we pump atoms to the extreme Zeeman sublevel, which is the m_F =+3/-3 for the F=3 component, and m_F =+4/-4 for the F=4 level.

The detection scheme we use for the 6S→7S excitation detects atoms which, after undergoing the $(F, m_F) \rightarrow (F, m_F)$ excitation have decayed to the other hyperfine F' component of the ground state. These atoms are made to cycle through a cycling transition of the D_2 line (see section 3.9 for detection through cycling transition). It follows from this, that in addition to pumping atoms of the F level to the extreme m_F, atoms must also be pumped out of the F' level or else their contribution will dominate our detection signal. The level of depletion must be low compared to the fraction of the population undergoing the 6S→7S excitation (~ 0.5 %).

In our atom beam apparatus, we perform the state preparation and satisfy the two requirements mentioned above, following the work reported on ref. [46]. We use a pair of ECDL lasers at 852 nm, crossing the path of the beam at right angles approximately 10 cm after the beam enters the chamber from the oven section. One of these lasers (the hyperfine laser) is linearly polarized and tuned to pump the atoms out of one hyperfine component, and the other (the Zeeman laser) is circularly polarized (and collinear to 2

the G magnetic field in the y-direction) and used to gradually drive the atoms to the extreme m_F of the other hyperfine component. Figure 3.18 shows an energy level diagram with the particular selections of transitions used to populate the (F=3, m_F =+/- 3) or the (F=4, m_F =+/- 4) Zeeman sublevel. For pumping to the (3,+3) level for instance, the hyperfine laser excites the F=4→3 transition and the Zeeman laser is right-circularly polarized and tuned to the F=3→3 transition, inducing Δm_F =+1 transitions. Atoms undergoing the Δm_F =+1 transition decay to the ground state with a selection rule Δm_F =0 or +/-1, but on average, at the end of the cycle they have shifted by Δm_F =+1 and after many cycles they accumulate in the extreme m_F. At that point the pumping is completed and atoms stop absorbing. In case they decay to the F=4 component, they are pumped out this state by the hyperfine beam until they return back to the F=3 level. In order to achieve this re-pumping by the hyperfine beam, the two beams have to overlap each other in the optical pumping region.

Fluorescence re-absorption by the atoms is the limiting factor to the optical pumping quality. Atoms in the OP region as well as atoms moving downstream from the OP region, can absorb light scattered in the region, and either decay to the nominally-depleted hyperfine component (F=4 in our example) or decay to the F=3, m_F=+2 level. The particular selection of transitions for the hyperfine and Zeeman laser is made such that the average number of cycles the atoms go through until they reach the extreme Zeeman sublevel is minimal. This results in the least amount of fluorescence produced during the process. Since fluorescence is proportional to the atom density in the beam, its re-absorption places a limit on the density of the beam we can work with, and therefore to the signal size in the weak transition measurements. This is a significant constraint in a shot-noise limited experiment. The authors of ref. [46] have done comprehensive studies of the optical pumping process, including pumping efficiency dependence on beam density, laser intensities and magnetic field strengths.

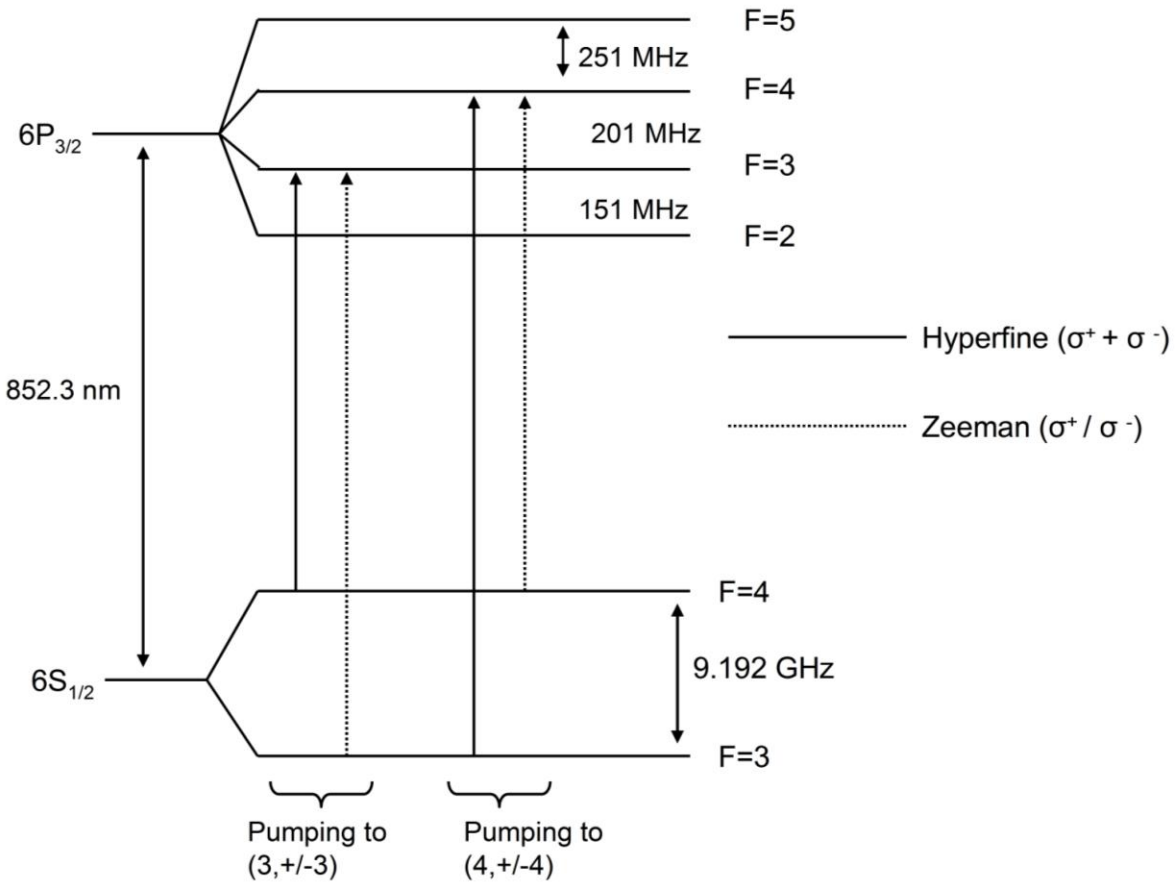

Figure 3.18: Sets of transitions used in the state preparation of the atom beam

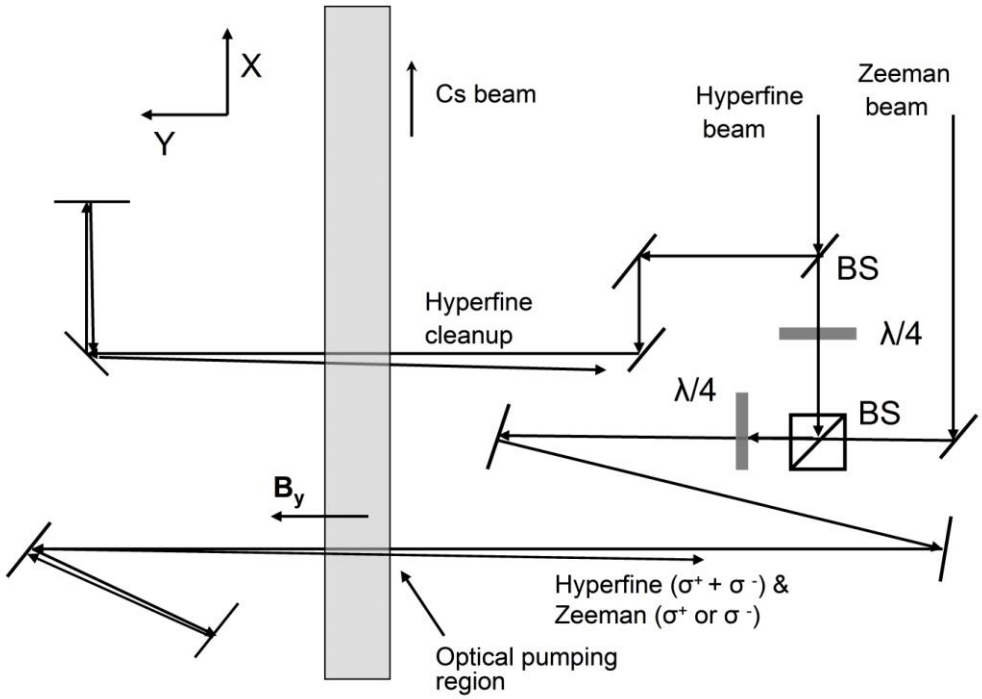

Figure 3.19: Optical setup for the optical pumping of atoms

In order to achieve as high a spin-polarization as possible, and to minimize the remaining population in the nominally-depleted hyperfine state, we have taken several steps. First, the hyperfine and Zeeman beams are double-passed through the optical pumping region. The two beams are combined in a non-polarizing beam-splitter, passed through a λ/4 waveplate (which changes the polarization state of the Zeeman beam to left- or right-circular and that of the Hyperfine beam to nominally linear) and then sent to the chamber. Upon exiting the chamber the beams are retro-reflected, retracing their original path. A layout of the relevant optical setup with the optical pumping beams is shown in figure 3.19. Second, we send another portion of the hyperfine beam to the atoms (about 7 cm downstream from the OP region), as a means of improving the depletion level of the depleted hyperfine level. This beam is also double-passed. Third, we have installed LN_2-cooled cryo-baffles in the chamber (see section 3.4), which catch

stray Cs atoms that would otherwise form a background vapor in the chamber and spoil the pumping efficiency, by emitting fluorescence which the atoms in the beam re-absorb. We have seen an improvement of ~ 5 times in the fraction of atoms in the depleted F level after installing the baffles.

Proper alignment of the hyperfine and Zeeman beams in the OP region is required in order to achieve good pumping efficiency. The alignment is performed while observing the Raman laser spectrum, which reflects the population distribution among the m_F levels (see section 3.10), and periodically measuring the leftover population in the depleted hyperfine level. The (dual) objective is to adjust the beam orientation in order to maximize the percentage of atoms in the extreme m_F level while at the same time minimizing the population remaining in the depleted level. It was observed in several instances that it is possible to optimize the former but not the latter, and some effort is usually needed to achieve both objectives. The two beams are circular with a 6 mm diameter, fully overlapping the 3 mm high atom beam. The hyperfine beam intensity is ~ 5 mW/cm^2, while the Zeeman beam intensity is ~ 1 mW/cm^2 (saturation intensity for the D_2 line ~ 1.5 mW/cm^2). Higher beam intensities did not improve the pumping efficiency. In fact, due to diode laser beam spectral impurities, power at the frequency corresponding to the opposite hyperfine component to the laser is tuned, induces unwanted transitions and affects the pumping process. This is discussed in C. Wood's thesis [18]. We have observed this behavior for intensities of the Zeeman laser higher than 1 mW/cm^2.

For the typical Cs beam conditions of the *M_1* experiment (oven temperature at 120 ^{o}C, nozzle at 170 ^{o}C) and with optimum OP beam alignment, more than 92% of the atom population is driven to the extreme m_F level and about 0.15-0.2% of atoms remain in the depleted F-level and contribute to the detection signal as a DC (with its noise) background. This latter value corresponds to a 6S→7S signal to background ratio of about 3 (~ 0.5-0.6 % of the atoms in the beam undergo the 6S→7S transition). Both the degree of spin-polarization and the degree of the hyperfine depletion are somewhat lower than the ones achieved by the Boulder group (~ 97% in the extreme m_F with 0.03% in the depleted level). We feel that this is primarily do to the fact that our beam density (and therefore the fluorescence from the OP region) is higher than that of the Boulder

experiment. We have worked with a density ~ 5-10·10^9 cm^{-3}, whereas the Wieman group reported a value of $3 \cdot 10^9$ cm^{-3}. In addition, the large size electric field plates required in the M_1 experiment block the optical access close to the interaction region, not allowing use of a second hyperfine cleanup beam. This will not be an issue in the PNC experiment, because of the different plate geometry required by that experiment.

3.9 Detection of the 6S→7S transition rate

The scheme introduced in (3.1) allows for a very efficient detection of the atoms undergoing 6S→7S transition. It detects the fraction of the atomic population, which after decaying back to the ground state, ends up in the hyperfine component which was depleted during the initial state preparation. For instance, in the case of the 6S→7S transition between the F=3 components, the scheme will detect atoms that decayed to the F=4 component of the ground state after the transition. This component was initially emptied by the hyperfine laser, and has almost no population at all in the absence of 6S→7S transitions. A wide laser beam at 852 nm, locked to the F=4→5 component of the D_2 line, puts the atoms into a cycling transition, with many photons scattered per atom during the transit-time through the beam. A large-area photodiode placed very close to the detection region collects a fraction of the emitted fluorescence (~10 %), yielding a large photocurrent. This way, all the atoms decaying to the F=4 component of the ground state are detected, and the detection efficiency for the 6S→7S transition rate is essentially the branching ratio for the $7S_{1/2}$ F=3 → $6S_{1/2}$ F=4 decay (of order ¼). For the F=4→4 component of the 6S→7S transition, the optical pumping depletes the F=3 ground state, and the detection laser cycles atoms through the F=3→2 component of the D_2 line.

The detection region is defined by the intersection of the 1.5 cm wide (y-direction) atom beam and the ~ 2 cm wide detection laser beam (x-direction). The 852 nm beam is linearly polarized, and double-passed through the region. Double-passing helps increase the amount of fluorescence emitted, since the atoms are more saturated.

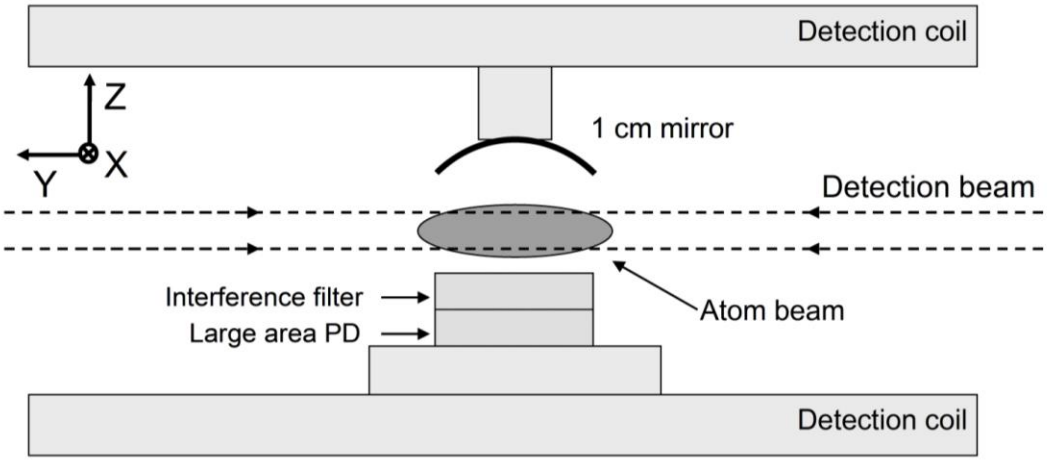

Figure 3.20: Geometry of the detection region. The atom beam propagates into the page(+x).

The height of the atom beam is greater than that of the 852 nm beam, so there is only partial beam overlap in the z-axis (figure 3.20) but this does not decrease our 6S→7S signal, since the height of the interaction region (defined by the 1079 nm beam diameter) is only about 400 μm, and so all 6S→7S atoms are detected. A pair of coils (detection coils) centered on the detection region, produces the required magnetic field in the region. The coils primarily cancel the ~ 3G z-field leaking from the interaction region coils, but are also used to apply an additional field in order to optimize the detection signal when the F=3→2 cycling transition is used. The large area photodiode, placed approximately 11 mm below the detection region, collects a fraction of the emitted fluorescence (~10%). An f=1 cm gold-coated concave mirror placed symmetrically above the detection region, helps increase the collected signal. An interference filter on top of the photodiode transmits light at 852 nm and blocks unwanted frequencies, such as scattered light at 1079 and 540 nm, room light, etc. The filter has a quite wide bandwidth (50 nm FWHM) which provides a decent angular-acceptance bandwidth of the 852 nm fluorescence. Due to the limitation in the latter bandwidth, most of the collected light (about 75%) comes from a (roughly collimated) reflection from the gold-coated mirror, and not directly from the detection region.

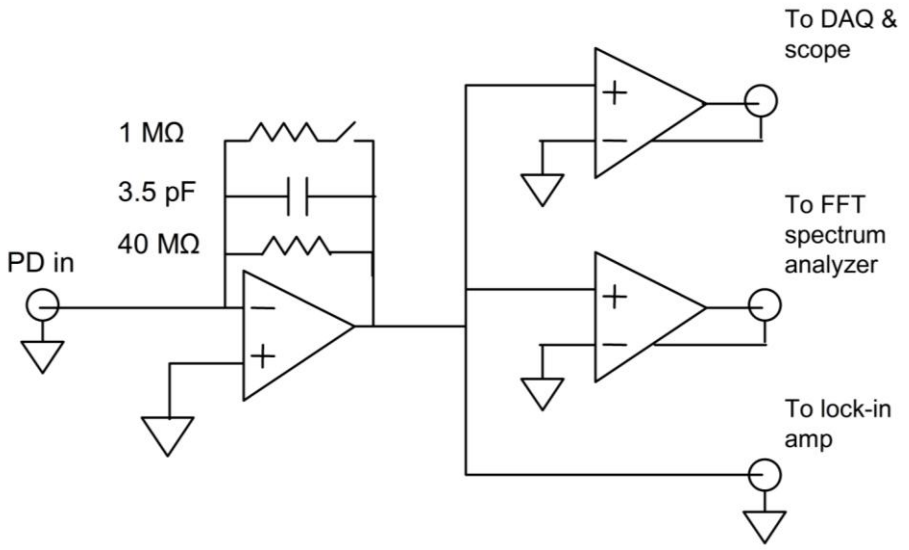

Figure 3.21: Schematic of the circuit used to amplify the detector photocurrent and distribute the amplified signal among different instruments

The large area photodiode is a Hamamatsu (#S3204-08) with an 18 x18 mm^2 active area. It is operated in the photovoltaic mode (i.e. no reverse bias is applied to it). The produced photocurrent is amplified in a transimpedance amplifier with a gain of 40 MΩ and a 1.1 kHz bandwidth (figure 3.21). The gain can be switched to a reduced value of ~ 1 MΩ, whenever the signal of the un-pumped beam needs to be measured. This is useful for probing the atom beam density, and also for measuring the detection laser noise (section 3.12). The transimpedance op-amp is an OPA 132 with a low input bias current, which is needed for our high gain system. The noise output level in the absence of any light incident on the photodiode of the detector and circuit is only ~ 1.5 μV/√Hz, which is a negligible contribution to the overall noise of the 6S→7S excitation. The output of the preamp is sent to a lock-in amplifier for phase-sensitive detection of the two-photon & weak amplitude interference in the 6S→7S excitation rate. The same output is also sent to an oscilloscope with FFT analysis capability (Tektronix TDS 3032B), the data acquisition system and another scope for signal monitoring. In order to avoid unwanted ground competition that could introduce noise in lock-in detection output and the FFT spectrum, instrumentation amplifiers are used to isolate the grounds of different instruments in the setup.

Spectral impurity in the 852 nm laser combined with a high optical intensity in the detection region can create issues in the detection. As seen in the Boulder experiment, and also experienced in our setup (both in the Zeeman beam, and in the detection beam), a high diode laser intensity tends to induce unwanted transitions, because of a small amount of power at frequencies ~ 9.2 GHz away from the transition frequency to which the laser is locked. For instance, when the detection laser is locked to the F=4→5 transition, some power at a frequency that corresponds to a F=3→F' component of the D_2 line, can induce such transitions and promote atoms to the F=4 ground state, resulting in an increase of the F=4 background. This is obviously unwanted since it increases the total noise in the 6S→7S excitation. In order to reduce this effect, the detection laser intensity is kept at a level for which the repopulation of the depleted state does not contribute significantly to the overall background. In our experiment, this intensity is ~ 4 mW/cm^2, which is a few times above saturation.

There is a difference in the amount of fluorescence emitted between the F=4→5 and F=3→2 transitions. Unlike the 4→5 transition, the 3→2 transition is not truly cycling. In the presence of the detection laser field, as discussed in Wood's thesis, the atom can evolve into a dark state that stops absorbing light. We have observed in our apparatus that under the conditions of the F=4→5 detection (linear polarization and detection region magnetic field ≈ 0) the F=3→2 signal is only about 10% of the F=4→5 level. In order to remedy this situation, when the F=3→2 detection is used, a ~ 2G field (+z-direction) is applied in the detection region. This creates conditions that prevent the system from evolving into a non-absorbing state, and results in a ~ 5 times increase in the emitted fluorescence. Since the detection field leaks slightly into the interaction region, the different field requirement for the detection of the F=3→3 and F=4→4 component of the 6S→7S transition means that the net interaction region field is also slightly different for the two measurements. This leakage however, is relatively small (~100 mG) and in the same direction (+z) as the 7G field created by the large interaction region coils. The M_1/β measurement does not depend on the particular B_z value. In addition, systematic contributions to the measurement related to magnetic field

misalignments, involve ratios B_x/B_z and B_y/B_z. Varying the detection region field does not introduce B_x or B_y components, which would result in systematic errors.

3.10 Measuring the Cs beam population distributions

For the purpose of optimizing the quality of the optical pumping of atoms, described in the previous paragraph, we need to be able to probe the distribution of the populations among the different m_F sublevels of the populated F state. Maximizing the fraction of atoms in the extreme m_F level is desired in the M_1 experiment, since the interference signal is proportional to the average m_F. Furthermore, in the PNC measurements, the measured observable ($\sim <m_F>E_{PNC}/\alpha$) depends directly on $< m_F >$, therefore an accurate measurement of $< m_F >$ is essential.

In the scheme we use to measure the population distribution among the sublevels of the populated F state, we stimulate off-resonant Raman transitions between the F component and the one depleted by the optical pumping process, and use the 6S→7S detection scheme to measure the occurring population transfer for each m_F level. This is the scheme of the Boulder experiment as well. It requires light at two frequencies, separated by the hyperfine splitting of the ground state (9.192 GHz). The two frequency components need to be phase-coherent. We have constructed an 852 nm ECDL whose injection current is modulated at 4.6 GHz to provide frequency sidebands that serve as our two Raman frequencies. The laser construction and its characteristics are described in (3.2.3). C. Wood's thesis provides a great deal of information regarding the off-resonant Raman spectroscopy employed in the Boulder experiment, including a detailed description of their methodology for accurately determining the m_F populations. In this section we will only give a brief description of the method, as we have applied it for probing the m_F populations in the M_1 experiment

We show in figure 3.22 an example of an off-resonant $\Delta m_F=0$ Raman transition, which is employed in order to probe the distribution among the m_F components of the $6S_{1/2}$ F=3 state. The higher Raman frequency component is locked with a 160 MHz detuning from the $6P_{3/2}$ F=2 state, in order to minimize unwanted population of the F=4 ground state. Atoms are stimulated from a given m_F level of the F=3 state to the same m_F

level of the state F=4. The 6S→7S detection scheme, which in this case will detect population increase in the initially empty F=4 state, can be used to probe the particular Raman transition. By scanning the Raman laser sideband frequency a few tens of MHz around 4.6 GHz, we sweep the frequency difference of the two laser sidebands and stimulate Raman transitions corresponding to all different m_F levels of the F=3 state. The F=4 population probing then, reflects the m_F population distribution in the F=3 state. The $\Delta m_F=0$ selection rule (valid when the Raman laser polarization is parallel to the magnetic field) makes it possible to probe the population of each m_F level separately.

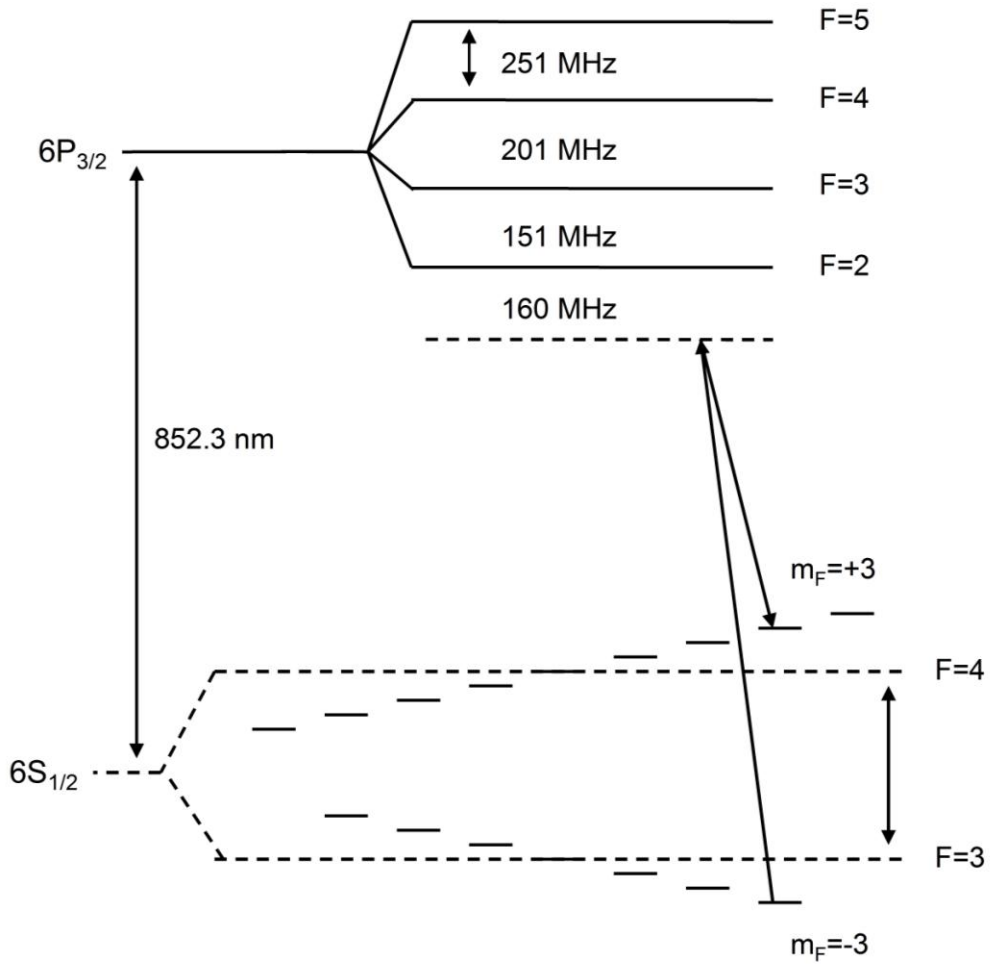

Figure 3.22: Example of off-resonant Raman transition that transfers atoms from the $6S_{1/2}(3,m_F)$ state to the $6S_{1/2}(4,m_F)$ state.

It is desired to probe the populations at the same location where the 6S→7S excitation occurs. For this reason, the Raman beam passes through the same field plate holes through which the 1079 and 540 nm beams also enter the interaction region. Due to the small size of these holes, the beam is moderately focused in the interaction region (using a 1 m lens). This results in a transit-time broadening of the Raman transitions (~0.5 MHz linewidth), which should otherwise be very narrow, since the excited state of the transition is a ground state. This however does not create any complications.

We show in figure 3.23 a typical $\Delta m_F=0$ Raman spectrum, from which we determine the quality of the state preparation of atoms in the F=3, m_F= +/-3 state. When the alignment of the optical pumping beams is optimized, about 92% of the atoms can be pumped to the extreme m_F level. This fraction is somewhat lower than the Boulder group efficiency (~ 96-98%), but this can be attributed to the fact that we work at a higher atom beam density (maybe 2 times higher). The Cs density is a limiting factor for the pumping efficiency. We have observed more complete pumping to the extreme m_F at lower densities.

An issue arises when measuring the population distributions for atoms pumped to the F=4 component of the 6S ground state. In this case the Raman transitions transfer atoms from the F=4 to the F=3 state. Since the initial state preparation pumps atoms to the extreme m_F states, the $\Delta m_F=0$ selection rule is not suitable, since the corresponding Raman spectrum does not provide any information about the $m_F=\pm4$ sublevels, for which we are most interested. To probe the populations, we switch the Raman laser polarization to horizontal, (perpendicular to B) and make use of the $\Delta m_F=\pm1$ selection rule. This selection rule results in pairs of different transitions which are degenerate in frequency. For instance the +3→+2 and the +2→+3 correspond to the same transition frequency. Fortunately, this excludes the transitions from the extreme levels (the m_F =+4→+3 and m_F= - 4→ - 3), which have a unique frequency. This allows us to probe the population of the extreme levels without significant complications.

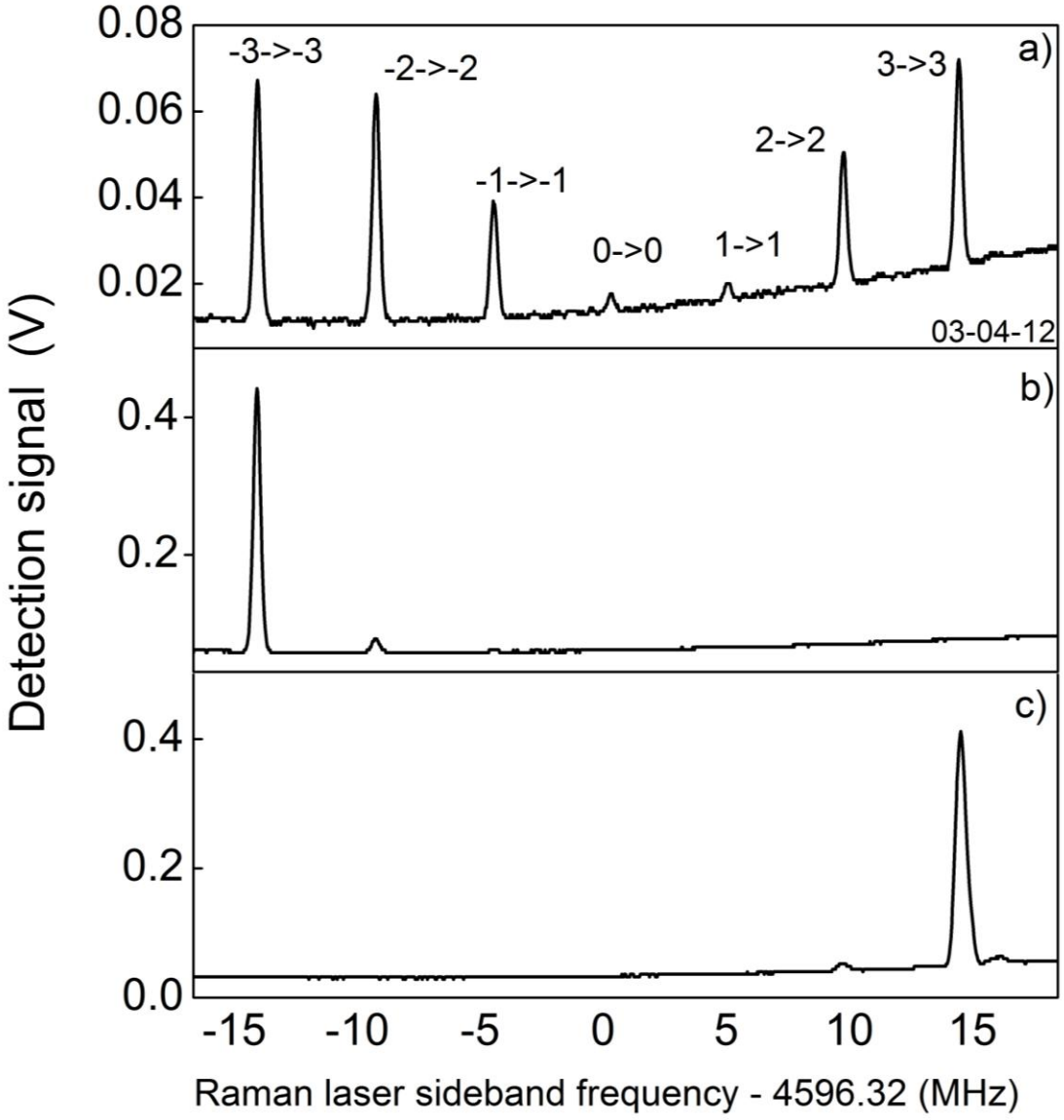

Figure 3.23: $\Delta m_F=0$ Raman transitions between the $6S_{1/2}$ F=3 and $6S_{1/2}$ F=4 ground states. In a) there is no Zeeman pumping and the peak amplitudes are essentially determined by the line strengths of each transition. In the intermediate b) and lower spectra c), approximately 92% of atoms are pumped to either the (3,-3) or the (3,3) state

3.11 The 6S→7S two-photon transition in the atom beam

In this section we discuss the characteristics of the two-photon 6S→7S transition, induced in the atom beam by the 1079 nm laser field. The two-photon transition is the stronger of the two pathways in our Coherent Control scheme.

The two-photon excitations occur in the interaction region, which is defined as the intersection of the overlapped 1079 nm & 540 nm laser beams and the ~ 1.5 cm wide atom beam. Since the intermediate level of the transition is not real, the two-photon moment is weak, and a large amount of laser intensity is required in order to obtain an appreciable excitation rate. Approximately 9 Watts of IR power is available in the beam and sent to the chamber, through an AR-coated window. Furthermore, the 1079 beam is weakly focused (using a 50 cm silver-coated concave mirror), with a ~ 180 μm waist ($1/e^2$ intensity radius) in the interaction region. The tighter the beam waist is, the lower the amount of the two-photon and one-photon pathway interference will be, since the requirements for overlapping the 1079 and 540 nm beams in the interaction region become more stringent. The particular choice of the beam waist size is a trade-off between the requirement for a large two-photon signal (which requires tight beam focus), and the need to avoid dilution in the observed interference. In the current state of the atom beam apparatus, the two-photon signal is such that the 6S→7S shot noise level is smaller than the combined noise level due to all other noise sources in the detection of 6S→7S atoms, and a further increase in the two-photon strength would not improve the SNR of the interference measurements substantially. With the modest focusing of the IR beam, we achieve a typical 1079 and 540 nm beam overlapping efficiency of 75% of the optimum.

The linewidth of the two-photon resonance is determined by the Doppler broadening in the atom beam, occurring due to the slight transverse velocity spread of the atoms. The Full width at Half Maximum (FWHM) linewidth is approximately 14 MHz, larger than the 3.3 MHz natural linewidth. Transit-time broadening of the resonance is negligible for our moderate beam focusing. A spectrum of the resonance (F=3→3 transition) is shown in figure 3.24. The linewidth was measured by applying a large electric field that Stark-shifts the resonance by a known amount, providing a frequency

calibration for the laser scan. A narrow linewidth is generally desired, since broadening decreases the resonance amplitude. However, an attempt to further collimate the atom beam (using a collimator made of microscope cover slips) resulted in a loss in Cs density much greater than the gain in signal due to the narrower linewidth.

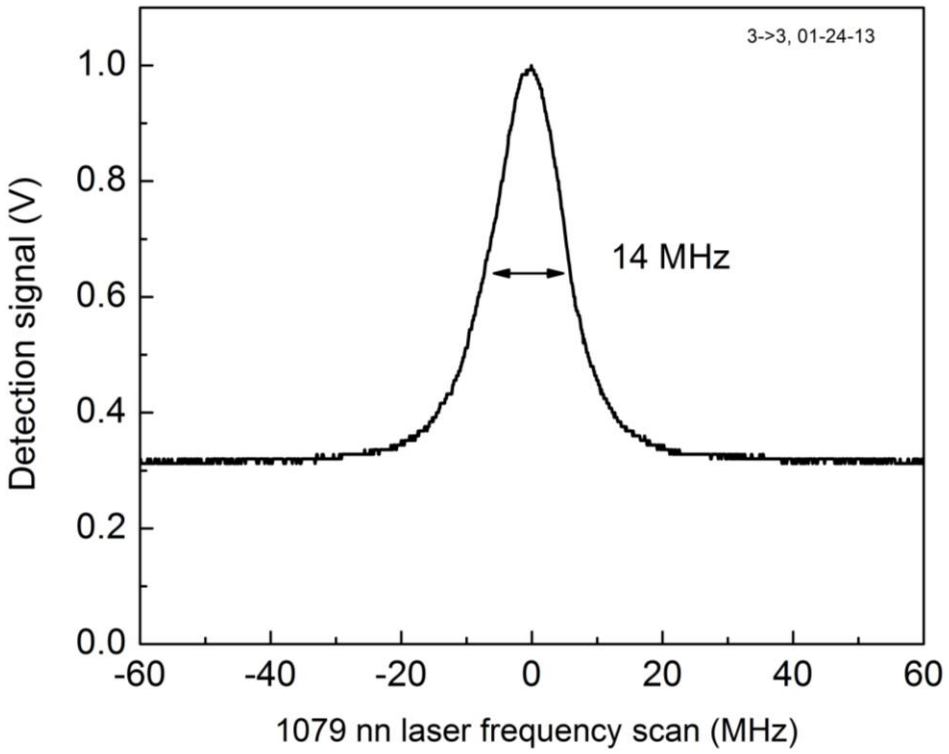

Figure 3.24: A spectrum of the two-photon F=3→3 6S→7S resonance in the atom beam

The detection of the 6S→7S transitions in the atom beam is done on top of a background level, as it can be seen in figure 3.24. About 85% of this background is due to the incomplete depletion (during the optical pumping process) of the hyperfine level probed by the detection laser, and to a lesser extent due to a slight repopulation of the same level, occurring due spectral impurities present in the detection laser. The presence of this background contributes slightly to the 6S→7S detection noise. A smaller fraction of the background signal (~15%) is due to scattered light reaching the large-area photodiode. The scattered light is mainly 1079 nm from the interaction region and 852 nm from the detection laser. This type of background however does not

contribute to the overall noise level, since it is small compared to the 6S→7S signal size, and also because the amplitude noise of the lasers is negligible.

3.12 Noise in the 6S→7S detection and estimation of the 6S→7S excitation rate

In this section we discuss the different types of noise present in the detection of the 6S→7S transition rate and we describe the measurements of noise levels of the various sources we have identified in our apparatus.

The first (and perhaps most fundamental) type of noise we discuss is shot noise. It represents the statistical fluctuations in any process that measures the mean value of a rate of random discrete events. If there are N events measured on average in some time interval, then the shot noise in the measurement is $\sqrt{N}$ and the fractional uncertainty in the measurement (noise/mean) is $1/\sqrt{N}$. An interesting property of shot noise is that its power spectrum is uniform, i.e. the same statistical fluctuations in the measurement of a rate appear for all different frequencies. In the detection of atoms undergoing 6S→7S excitations, shot noise represents the fluctuations in the rate of 6S→7S atoms arriving in the detection region and being detected. The higher this rate is, the lower the relative fluctuations in this rate will be. The $\sqrt{N}$ nature of shot noise is a distinctive feature of this particular noise type, and it can be used to discriminate shot noise from the other noise types present in the detection of atoms, the technical and background noise.

Technical noise is the type of noise that grows proportionally to the signal level. This implies that its contribution to the overall fractional noise in the detection of atoms does not depend on signal size. In the atom beam apparatus, the dominant sources of technical noise appear to be frequency noise on the detection laser as well as frequency and amplitude noise in the 1079 nm laser. Background noise is any type of noise which contributes by a constant amount to the overall noise level. Sources of background noise include noise due to scattered light in the chamber, noise in the electronics, photodiode dark current noise etc. These however have a negligible contribution to the overall 6S→7S noise.

The measurements of the two-photon and weak amplitude interference in the experiment are done by lock-in detection of the 150 Hz modulation imposed on the

interference term present in the 6S→7S transition rate. We have characterized to a reasonable extent the statistical noise sources in the 6S→7S signal and have managed to decrease the level of some of these at (and around) 150 Hz in order to improve the signal to noise ratio of the experiment. The main sources of noise in the detection appear to be shot noise in the 6S→7S two-photon rate, shot noise due to the background of atoms in the nominally depleted F state, as well as technical noise in the 852 nm detection laser and the 1079 nm laser (primarily amplitude noise). We have been able to measure the level of each of these contributions to the overall noise.

There is a simple noise measurement method that allows us to make estimates for the technical noise of the detection laser, the shot noise level in the 6S→7S transition rate and from that, obtain an estimate for the number of the detected the 6S→7S atoms/sec. The method is based on the ability to discriminate shot from technical noise. We can write for the total fractional noise (total noise/mean signal) S_F in the detection of atoms, measured in a 1 sec time interval,

$$S_F = \sqrt{\frac{1}{N} + T^2 + \frac{BG^2}{N^2}} \tag{3.1}$$

where T and BG are the fractional technical noise and background noise respectively. The unit for the fractional noise is parts per million (ppm) per √Hz. The background noise is much smaller than the other two contributions, and so the corresponding term can be dropped in (3.1). Of the two remaining terms, the shot noise is the dominant term for small N and the technical noise for a large value of N. The different behavior of S_F at the two limits is the key fact that we exploit in these measurements: we measure the fractional noise of the detection signal for different signal levels. At high levels, the technical noise dominates and T can be estimated from the asymptotic behavior of S_F. The T measurement can be then used to establish a relationship between the fractional noise and the number of atoms detected per sec:

$$N = \frac{1}{\sqrt{S_F^2 - T^2}} \tag{3.2}$$

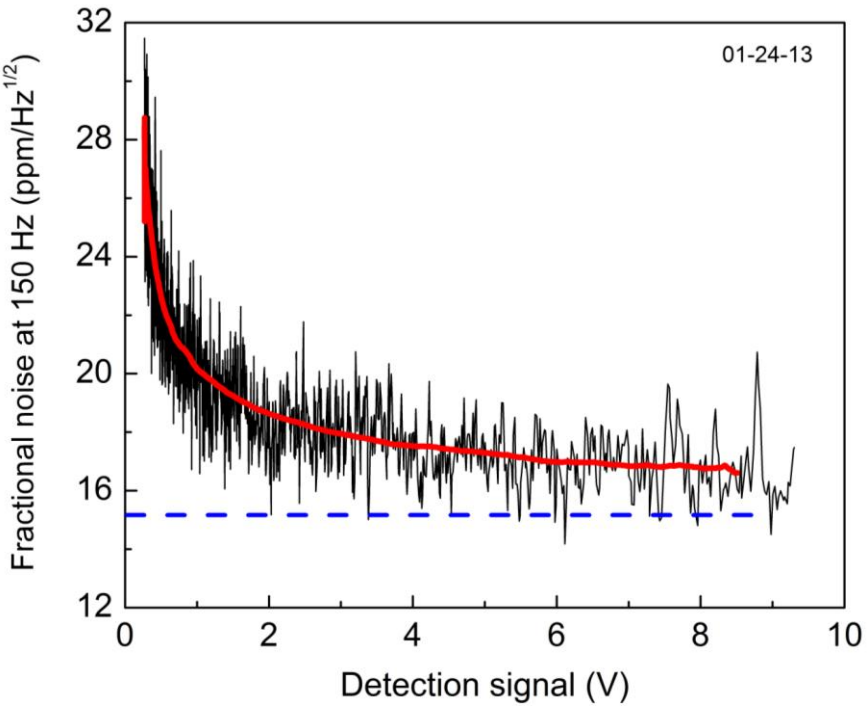

Figure 3.25: Plot of the fractional noise measured in the atom beam as a function of the photodiode signal (or atom beam density). The thick red line represents an average of the instantaneous noise level (black line).

We show in figure 3.25 a plot of the fractional shot noise measurement S_F on the F=4→5 cycling transition. The measurement is performed at 150 Hz with the same lock-in amplifier that is also used in the lock-in detection of the interference signal of the 6S→7S transition rate. The lock-in outputs a signal proportional to the measured noise (in √Hz). This signal is scaled (taking into account the lock-in gain), and divided by the detection signal level to obtain the fractional noise. The measurement is performed while the beam density is let to gradually decrease, after having turned the Cs oven heaters off. No optical pumping of the atoms is performed, and so 9/16 of the atoms in the beam populate the F=4 state, resulting in a large photocurrent from the large-area photodiode. The fractional noise reaches a typical plateau of T=15-16 ppm/√Hz at high beam densities. This level is solely due to the 852 nm detection laser and characterizes its performance. At low densities, comparable to the ones of the actual experiment, the shot noise of the atoms becomes significant. For the typical 6S→7S signal level in the

experiment of ~ 650 mV (F=3→F=3 transition), we can estimate a ~ 22 ppm/√Hz total noise level from the plot of figure 3.25. This corresponds to a shot noise 1/N = $\sqrt{22^2 - 15^2}$ ~ 16 ppm/√Hz or to a detected 6S→7S rate N~ $4 \cdot 10^9$ /sec . A similar analysis for the detection of the F=4→F=4 component of the 6S→7S (detection on the cycling F=3→2 transition), yields a 6S→7S shot noise level of ~ 18 ppm/√Hz or a rate of detected atoms ~ $3.1 \cdot 10^9$ /sec.

In another simple measurement with the lock-in amplifier we determine the amplitude noise of the 1079 nm light. The signal from an amplified photodiode on which a small portion of the 1079 nm light from the fiber amplifier is incident, is sent to the lock-in for a noise measurement at 150 Hz. We obtain a fractional noise of ~ 4 ppm/√Hz. This corresponds to a contribution to the 6S→7S rate of 8 ppm/√Hz (the two-photon transition rate is proportional to the square of the 1079 nm power). This level is low enough so that it doesn't add substantially to the overall detection noise.

Table 3.1 summarizes all noise measurements and estimates we have been able to make. These levels are listed separately for the F=3→3 and F=4→4 components of the 6S→7S transition. We note that the combined noise level of all sources is smaller than the level measured in the 6S→7S transition under the conditions of the actual experiment. The difference is greater for the F=4→F=4 transition. This difference must be made up by other potentially significant noise sources that we were not able to identify. These could include frequency noise of the two 852 lasers used for optical pumping as well as frequency noise of the 1079 nm laser. Each of these potential sources on its own however does not appear to affect the overall noise substantially. We determined this in a crude test where we looked for changes in the 6S→7S noise while switching the fast feedback of the laser lock (through the laser diode current) on and off. No difference in the 6S→7S noise level was observed. As a reference for comparison, the 6S→7S noise level drops by about 2 times when the current feedback to the detection laser is engaged.

Table 3.1: Fractional noise levels of the various sources of noise identified in the apparatus, combined level of known sources and actual 6S→7S noise of the experiment. Values are listed separately for the F=3→3 and F=4→4 transitions. All levels are with respect to the 6S→7S two-photon signal (BG signal subtracted).

6S→7S transition	F=3→3	F=4→4
Detection cycling transition	F=4→5	F=3→2
6S→7S shot noise	~16 ppm	~18 ppm
852 nm detection laser noise	~16 ppm	~19 ppm
Background atoms shot noise	~9 ppm	~12 ppm
Background atoms detection noise	~5 ppm	~9 ppm
1079 nm laser amplitude noise	~8 ppm	~8 ppm
Combined known sources	~26 ppm	~31 ppm
Actual 6S→7S noise	~32 ppm	~48 ppm

Using the rate of detected 6S→7S atoms estimated for the F=3→3 transition ($N\sim 4\cdot10^{9}$ /sec), we can make another estimate, regarding the number of photons collected by the large-area photodiode per atom cycling through the F=4→F'=5 transition. This is possible by comparing the rate of photons incident on the photodiode, to the 6S→7S rate. From the generated photocurrent and the detector spectral responsivity, we estimate that ~ $6\cdot10^{10}$ photons/sec are incident on the photodiode. This corresponds to 15 photons being collected per atom cycling through the 4→5 transition. From a similar analysis on the F=3→3 excitation and detection through the F=3→2 transition, we obtain an estimate of 5 photons collected per 6S→7S atom.

A further comparison, that of the number of photons collected per cycling atom, to the number of cycles each atom goes through while crossing the detection region, provides an estimate for the photodiode collection efficiency. Based on the atom transit time through the detection region and excitation rate for the saturated 4→5 transition, we can estimate that each atom cycles through the 4→5 transition ~165 times. This corresponds to a collection efficiency of ~ 9 %.

3.13 The Mach-Zehnder interferometer

The optical phase-delay imposed between the 1079 nm and 540 nm fields as a means to observe the interference in the 6S→7S transition, is done in a Mach-Zehnder interferometer. A drawing of the setup is shown in Figure 3.26. The paths of the co-propagating green and IR beams are split on the interferometer's dichroic input mirror. The green beam is double-passed though a rotating galvanometer-mounted plate, used to delay the 540 nm optical phase. The two beams are recombined on a second dichroic mirror and sent to the vacuum chamber. A hot mirror in the path of the green and a cold mirror in the path of the IR beam are used to block leakage of one frequency component into the path of the other, which could otherwise create unwanted amplitude modulation of the fields in the interaction region. Since the M_1 experiment requires horizontal polarization (ε_x) for the 540 nm field, a $\lambda/2$ waveplate in the green beam path is used to switch the incoming beam's vertical polarization.

The amount of two-photon and weak amplitude interference depends critically on the 1079 and 540 beam overlapping conditions in the interaction region. The slight beam motion occurring during the galvo-plate rotation needs to be kept to an acceptable level, or else the interference amplitude will vary during rotation, leading to a systematic error in the experiment. Double-passing the 540 beam through the 2 mm thick plate, solves most of the beam motion issues. For our particular geometry (green beam angle of 1st incidence ~ 10^{o}, beam separation ~ 7 ^{o}) we estimate that in a typical 20-cycle scan of the green beam phase (10 cycles per degree of rotation), this shift is approximately 2 μm or roughly 1% of the 540 nm beam waist in the interaction region. With the double-pass configuration, we do not detect any variation in the 6S→7S modulation during a phase-scan.

In addition to the possibility of slight beam motion, there are two more effects related to the galvo-plate rotation that we need to consider. The first is an etalon effect in the plate. The finite reflectivity of the AR-coated plate introduces a small sinusoidal modulation in the beam intensity, observed as the galvo-angle is swept. The amplitude of this modulation is measured to be ~ 0.4 % of the mean green power level. This modulation introduces a systematic error in the interference amplitude measurements.

However, as we show in chapter 4, the contribution of the effect to the measurements turns out to be negligible for the conditions of our experiment. The second effect is a non-linearity in the 540 nm beam phase-scan, occurring due to the non-linear nature of the path length sweep, as the plate rotates. This results in a ~ 11 % variation for the phase-scan rate, observed between the two extreme positions of the galvo. As discussed in (4.2), we are able to make measurements of this effect and include it in the data analysis, so this moderate amount of non-linearity does not create significant concerns.

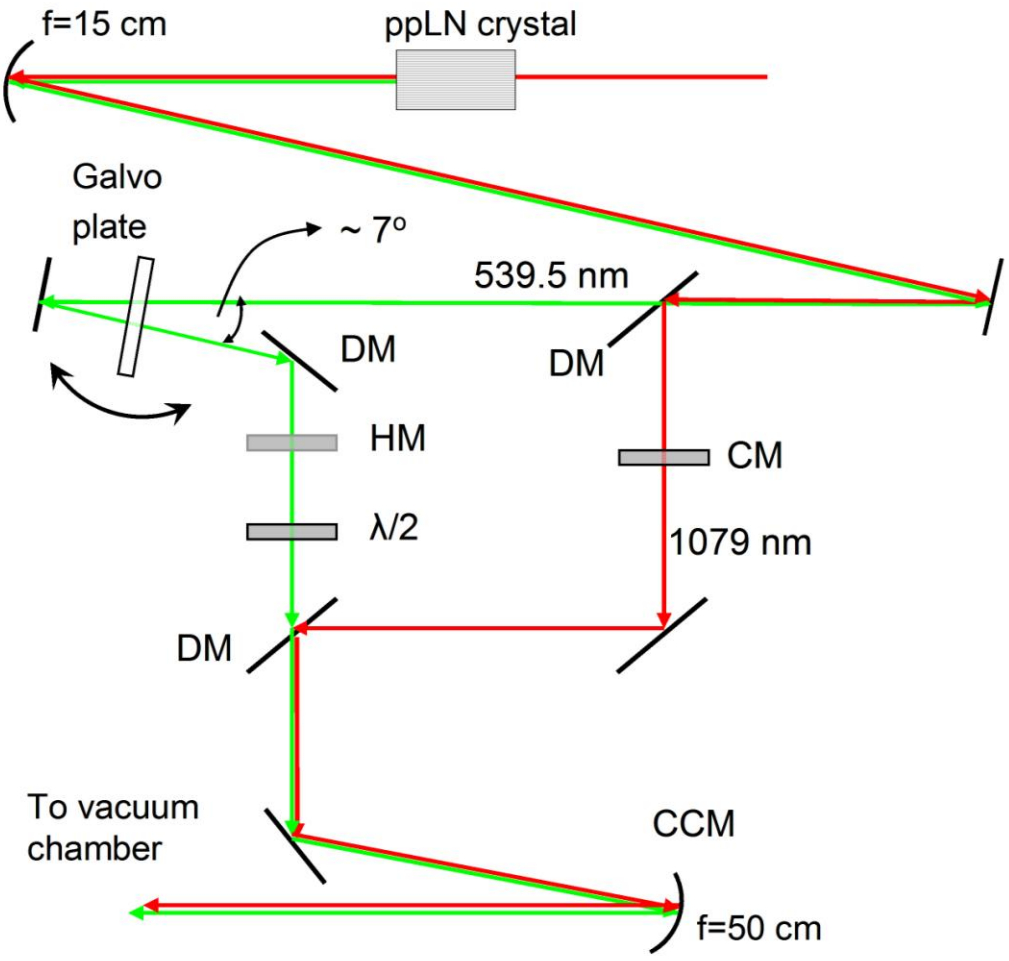

Figure 3.26: The Mach-Zehnder interferometer used to delay the phase of the 540 nm laser field. Abbreviations: DM: dichroic mirror, HM: hot mirror, λ/2: half-waveplate, CM: cold mirror, CMM: concave mirror (silver-coated).

The need for double-passing the green beam through the galvo-mounted plate, led to a choice of an asymmetric geometry for the interferometer, with different path-lengths for the IR and green beams. This difference makes the system more sensitive to relative IR-green phase-shifts, caused by temperature and humidity variations. These drifts are reflected on the interference pattern, and (depending on conditions) can in some cases be as large as a few percent of a cycle per minute. In our data acquisition routine however, the 540 nm phase-scans are performed fast enough (~ 8 sec) so that such drifts have a negligible effect on the measurements. Air-currents in the room can create bigger problems, since they induce phase-fluctuations on a much faster scale, and so the interferometer (and in fact all of the optical setup close to the chamber) is covered with a large Plexiglas cover.

In order to ensure mechanical stability of the setup, all the components are mounted on an aluminum breadboard (12”x12”x0.5’’), which is bolted to its base with nylon screws. Rubber sheets between the plate and its base reduce vibration coupling to the setup. There are two factors which are particularly important in the mirror mount selection. The first is the mount mechanical robustness. The more robust the mount is, the smaller the phase-noise due to vibrations. The second and perhaps more important factor is the amount of relaxation in the mount adjusters after an adjustment has been made. As part of the daily use of the apparatus, the green beam orientation needs to be adjusted slightly to maximize the signal. This is done using one or two of the Mach-Zehnder mirrors. If the amount of relaxation-related drift in the beam orientation is significant, it shows up as a drift in the observed interference. We have used JILA-type mounts for all the mirrors in the setup, which are known to be mechanically stable.

3.14 Lock-in detection of interference

The amplitude of the two-photon vs. one-photon interference is very small compared to the size of the two-photon signal. In the M_1 experiment, the modulation in the 6S→7S rate is only about a few parts per ten thousand of the two-photon rate. This signal level is buried under the noise of the large DC background, making direct

detection of the modulation impractical. We have used phase-sensitive (lock-in) detection of the interference, in order to extract the weak signal from the much greater background.

Lock-in detection is a method commonly used to detect small signals on top of much larger backgrounds or noise. In this method, a periodic modulation at a frequency ω_m is imposed on the signal to be extracted. Timing for the modulation is provided by a harmonic or square wave with a well-defined phase. This is typically called the phase-reference. The large, noisy signal from which we seek to extract the small signal, is multiplied in a mixer (demodulated) with the phase-reference. The mixer output is then filtered in a low-pass filter (cut-off frequency ω_c), followed by amplification. The result is a DC (or slowly varying) signal, whose amplitude is proportional to the weak signal, plus any other components present in the original signal, whose frequencies are within the $\omega_m \pm \omega_c$ range. All frequency components outside this band are filtered out. By making the low-pass frequency ω_c smaller, the SNR in the detection increases, since more noise is rejected. The SNR can also be improved by selecting ω_m to be within a quiet region of the spectrum. Based on this description, the lock-in detection can be thought off as a very narrow filter, placed around the signal that one seeks to measure. The lock-in detector detects signals which are in-phase with the phase-reference. Out-of-phase signals are not picked up. If there is a phase-shift between the reference and the weak signal, the lock-in output will be diminished. Therefore, some adjustment is usually required in the relative phase between the two mixer inputs, in order to obtain the maximum output. Some lock-in amplifiers (dual phase) are capable of simultaneously detecting both in-phase and out-of-phase components (X and Y quadratures) of the modulation, which they use to compute the modulation magnitude. In magnitude measurements, the relative-phase shift doesn't matter.

To implement lock-in detection in our apparatus, we need to impose a modulation on the interference signal. This is done by applying a sinusoidal dither to the galvo-motor at a frequency $\omega_m \approx 2\pi \cdot 150$ Hz, in addition to the ramp that slowly scans the green beam phase. The resulting phase-modulation shows up as a modulation on the 6S→7S rate, synchronous with the dither signal. The signal from the detection region is sent to a

commercial lock-in amplifier for demodulation. The lock-in outputs a signal proportional to the interference term. This process is sketched in figure 3.27.

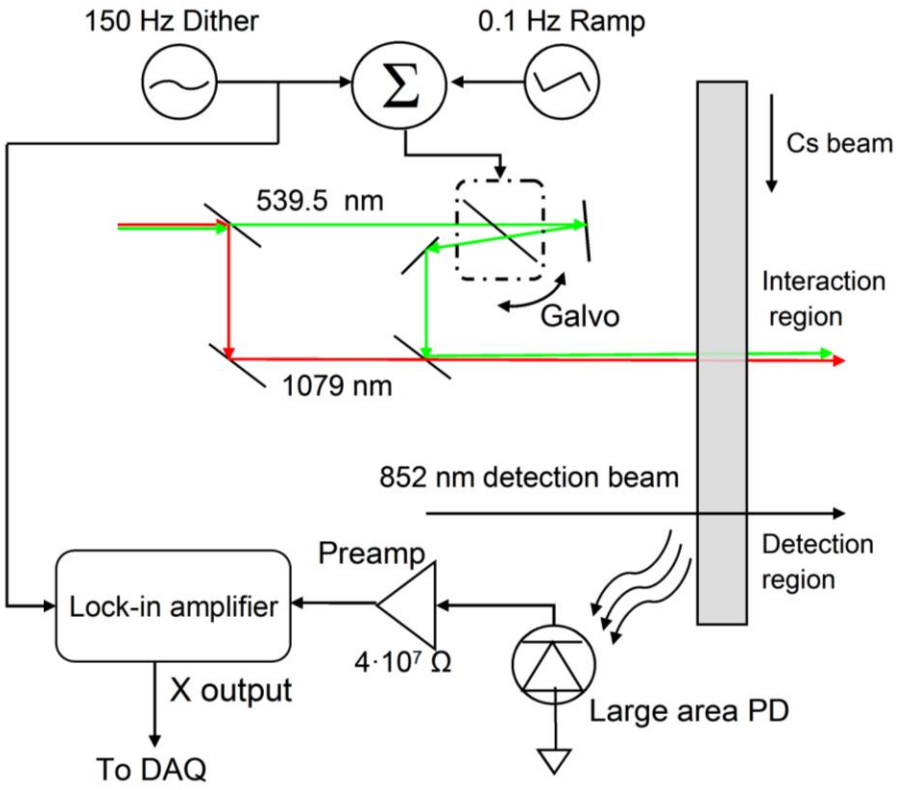

Figure 3.27: A schematic of the lock-in detection scheme used to detect the two-photon and weak amplitude interference

The interference signal, in the presence of the galvo-plate dither, can be expressed in a convenient form that reveals the nature of the modulation imposed on the signal. Its contribution to the overall 6S→7S rate has the form:

$$W_i = 2A_{2p}A_w\cos(\varphi_m + \varphi_s) \tag{3.3}$$

where the phase of the interference is separated into two terms: a term which corresponds to the phase dither (φ_m) and a second term (φ_s) which represents the slow phase-scanning

of the 1079 and 540 nm phase difference. For sinusoidal modulation of the phase by an amplitude m, we can write:

$$\varphi_m = m\cos(\omega_m t) \tag{3.4}$$

Using (3.4) and the following identities involving the Bessel functions $J_n(m)$:

$$\cos\left(m\cos\theta\right) = J_0\left(m\right) + 2\sum_{n=1}^{\infty}\left(-1\right)^n J_{2n}\left(m\right)\cos\left(2n\theta\right) \tag{3.5}$$

$$\sin\left(m\cos\theta\right) = -2\sum_{n=1}^{\infty}\left(-1\right)^n J_{2n-1}\left(m\right)\cos\left(\left(2n-1\right)\theta\right) \tag{3.6}$$

W_i can be expressed as follows:

$$\begin{aligned} W_i = 2A_{2p}A_w\{&J_o\left(m\right)\cos\left(\varphi_s\right) - 2J_1\left(m\right)\cos\left(\omega_m t\right)\sin\left(\varphi_s\right) \\ &- 2J_2\left(m\right)\cos\left(2\omega_m t\right)\cos\left(\varphi_s\right) + ...\} \end{aligned} \tag{3.7}$$

(3.7) is a series of harmonics in $\omega_m t$. It can be seen that the amplitude of the n^{th} harmonic is dependent on $J_n(m)$, and it can be varied as a function of the scanning phase φ_s. With our lock-in amplifier, we detect the first harmonic of W_i, while slowly scanning φ_s (~ 2.5 cycles/sec). The first harmonic has the largest amplitude among all non-zero order harmonics ($\approx 2\cdot J_1 max=1.164$), that is obtained for a depth of modulation $m \approx 0.29\cdot 2\pi$. This corresponds to a plate rotation amplitude $\approx 0.03^o$, much larger than the $\sim 0.001^o$ resolution of the galvo-motor. In practice, m is optimized by adjusting the galvo-dither amplitude, while looking at the lock-in output.

The selection of the particular modulation frequency requires some justification. We want to modulate in a quiet frequency region of the 6S→7S spectrum. Below 100 Hz, noise from the lasers, mechanical vibrations and 60 Hz noise, create a noisy environment for the modulation detection. Above 250 Hz, the modulation amplitude starts diminishing. This is due to the longitudinal velocity spread of the atoms in the beam. All atoms getting excited in the interaction region at a particular instant, contribute with the same overall phase to the interference term. However, owing to their different velocities, they arrive in the detection region (which is where the modulation is detected) at different times. This results in a slight phase-mixing that reduces the measured interference. To avoid appreciable reduction, the modulation frequency has to be a small fraction

(< 25%) of the inverse spread in the transit time from the interaction to the detection region, or approximately 1 kHz. The authors of ref. [47] have made a comprehensive analysis of the effect in their Yb beam apparatus. In addition to the constraints explained above, we have found that the narrow region around 150 Hz is relatively free of intermittent technical noise, which is why the particular frequency was chosen. The interferometer galvo-system has a bandwidth sufficiently large to support this frequency (~ 1 kHz for small angles).

3.16 Optimizing the interference amplitude

The amplitude of the two-photon and weak amplitude interference in 6S→7S rate depends on the quality of the 1079 and 540 nm beam overlap in the interaction region. Similar to the effort involved in optimizing the optical interference of two overlapping beams of the same color, careful alignment of the 1079 and 540 beams is necessary to obtain good results. Compared to working with collimated beams, the overlap requirements in the M_1 experiment are more stringent, since the green and IR beams need to be focused in the interaction region. M. Gunawardena's thesis [48] includes a complete analysis of the effect of various alignment/overlap imperfections to the amount of interference that can be obtained. Here we only summarize the main requirements, discuss the precautions taken in the design of the relevant optical setup and explain the beam alignment procedures followed to optimize the interference amplitude.

The interference in the excitation rate is of the form:

$$W_i = 4\eta J_1(m) E_{\omega}^2 E_{2\omega} A_{2p} A_w \sin(\varphi_s) \tag{3.8}$$

where φ_s is the slowly swept 540 nm phase, and η is the overlap factor, which results from integrating the interference term over the volume of the interaction region. It accounts for non-optimal beam shapes and sizes or alignment. Under optimal conditions, η=1.

Proper beam overlapping requires that the IR to green beam waist ratio is $\sqrt{2}$. This condition is satisfied for the beams exiting the frequency doubling crystal. Preservation of the $\sqrt{2}$ factor until the interaction region is possible if both beams are very well collimated while propagating towards the chamber. This is feasible in the

absence of any thermally induced lenses. Collimation after the ppLN crystal is done with a f=15 cm silver-coated concave mirror, on which the two beams reflect upon exiting the frequency doubler. To optimize collimation, the beams profiles are observed at a large distance (~ 5 m) from the mirror, while making fine translations of the mirror position. Due to heating in the ppLN crystal, occurring from IR (primarily) and green light absorption, the two beam sizes may vary slightly, depending on the IR power going through the crystal. For this reason, the collimation is always done at maximum IR power, of same level as in actual experiment.

To avoid thermal lensing due to absorption of the high power IR, the number of refractive elements in that beam path was kept to a minimum. For the same reason, the window that admits the two beams in the vacuum chamber is made from UV fused silica, which has a lower refractive index dependence on temperature than the more commonly used BK7 glass.

Astigmatism introduced by the two concave mirrors in the path of the beams (the f=15 cm collimating mirror and f=50 cm focusing mirror, figure 3.26), needs to be minimal. For this reason, the angles of incidence on the two concave are kept small (~10^{o} or less). In addition, by using a mirror to focus beams to the interaction region instead of a lens, we avoid introducing chromatic aberrations to the beams that could have an effect on the beam overlap.

Ideal beam alignment requires that the beam axes of propagation be perfectly matched. Any offset or non-zero crossing angle between the axes, results in a decrease in η. This requirement can be quite time-consuming to achieve, and some effort is required to optimize the beam overlap. Since optimizing the interference ultimately relies on looking at the interference signal and tweaking beam alignment, obtaining the two-photon signal at the beginning of the process is necessary. This is why the IR beam alignment through the electric field plates in the chamber is done first. After this, the green beam needs to be nominally overlapped with the 1079 beam. This is done by visually overlapping the beams at two distant points (~ 5 meter away). This can be done at low power, or at full IR power, by picking off a small fraction of the beams. No repetition of this step is required, unless major changes have been made in the setup.

Finally, to maximize the interference amplitude, fine alignment is required. This is done on a daily basis before data acquisition starts. The interference signal is observed at a high Stark-field (~300 V/cm), for which the two-photon Stark-induced interference produces a large modulation. The alignment involves fine-tuning of the 540 nm beam using one (or sometimes two) of the Mach-Zehnder mirrors. As discussed in section 4.3, it may be necessary to slightly adjust the mirror that focuses both the IR and green beams to the interaction region, in order to null a Doppler-shift of the 6S→7S resonance present in the atom beam. Since both beams are walked together, this procedure does not affect the beam overlap.

We have been able to measure the overlap factor η using an electric field geometry different from that of the M_1 experiment. Measuring η is not possible under the conditions of the M_1 experiment, since this requires knowledge of the weak amplitude rate. Even at the highest electric field obtainable, the β-Stark rate is too small to be directly observed. To measure η, we employed the stronger α-Stark induced transitions ($\alpha/\beta \approx 10$) along with a different set of electric field plates that produces a large E_z field (up to 5 kV/cm). This field, combined with z-polarization for the 540 nm beam, induces transitions, whose rate is $\sim 2 \cdot 10^4$ times stronger that of the β-Stark rate in the M_1 experiment, allowing direct observation of the one-photon rate. From observations of the two-photon and α-Stark rates, and the measured interference amplitude, we determine a value of $\eta \approx 0.75$. This is adequate for the M_1 experiment, with about ¼ of the signal being lost. Some variation in η is expected of course, since the value depends on the daily beam overlap optimization procedure. Because of the different optical setup requirements in the future PNC experiments, a higher η value will likely be achieved there.

3.17 Instabilities in the interference amplitude

An unwanted fluctuation in the amplitude of interference occurs due to the high IR intensity present in the experiment. Measurements of the interference amplitude at different times (at high electric fields), showed a ~ 5% variation in the amplitude, that could not be explained by Cs density drifts, IR / green power fluctuations, or statistical

noise. This observation, along with a smaller fluctuation seen in the two-photon rate, also inconsistent with atom density and power drifts, suggested that there must be some instability in the IR-green overlap, the IR beam waist, and possibly in the green beam waist too. Any of these three possibilities results in variation in the overlap factor η (3.8). Such variations can lead to a systematic error in the M_1 measurements, if not treated properly.

In order to characterize this effect, we have looked for variations in green-green optical interference, using our Mach-Zehnder interferometer. This allowed us to work with different combinations of IR and green power levels, something that would not have been feasible in atomic interference studies, due to a greatly reduced signal for low IR or green power. The setup used is similar to the interferometer of figure 3.26. Some of the optics were removed or replaced in order to allow some green light leakage in the IR arm (which is interfered with the main green beam on a photodiode), and in order to block any IR light from reaching the photodiode. In addition, different attenuators were used in the path the green beams, depending on power levels.

The measurement procedure is as follows: we record the small interference signal, detected with the lock-in amplifier, as the galvo-plate slowly scans the green beam phase (20 cycles in ~ 60 sec). This is done at different times, within a ~ 35 min interval. We show a typical interference signal in figure 3.28 a) . A Fast Fourier Transform (FFT) of the lock-in output provides amplitude that is plotted as a function of time. Figures 3.28 b), 3.28 c), 3.28 d) show the normalized FFT amplitude vs. time, in three different cases b) high IR power through the crystal and high green power produced, c) high IR but low green power (the ppLN crystal is temperature detuned to decrease conversion efficiency), d) low IR power input to the crystal and low green power generated.

The cause of the instability, as determined from the measured variation of the interference amplitude, must be related to the high IR power. The fluctuations for the high power data are about 9 %. The instability is most likely generated in the frequency doubling crystal, where the ~ 10 W of IR light is focused to a ~ 45 μm waist (radius), resulting in a very large intensity. Another possibility is the thermal lensing present in the

12.5 cm lens that focuses the IR beam to the ppLN crystal. At low IR power, the variation is about 4 times smaller. Based on the latter, we can eliminate mechanical instabilities in the optical setup as a possible cause. At high IR, but low green power, the variation is about 6%. This decrease observed for a smaller green power, could be due to a decreased Green-Induced IR absorption effect (GRIIRA), which may be present in the crystal at high the green power. There are two mechanisms that could be causing the IR power-dependent instabilities in the ppLN crystal: thermal lensing and photo-refraction occurring at high power. We must note however that regardless of the nature of the effect, it is the variation in the strength of effect under steady state conditions that creates the unwanted instabilities.

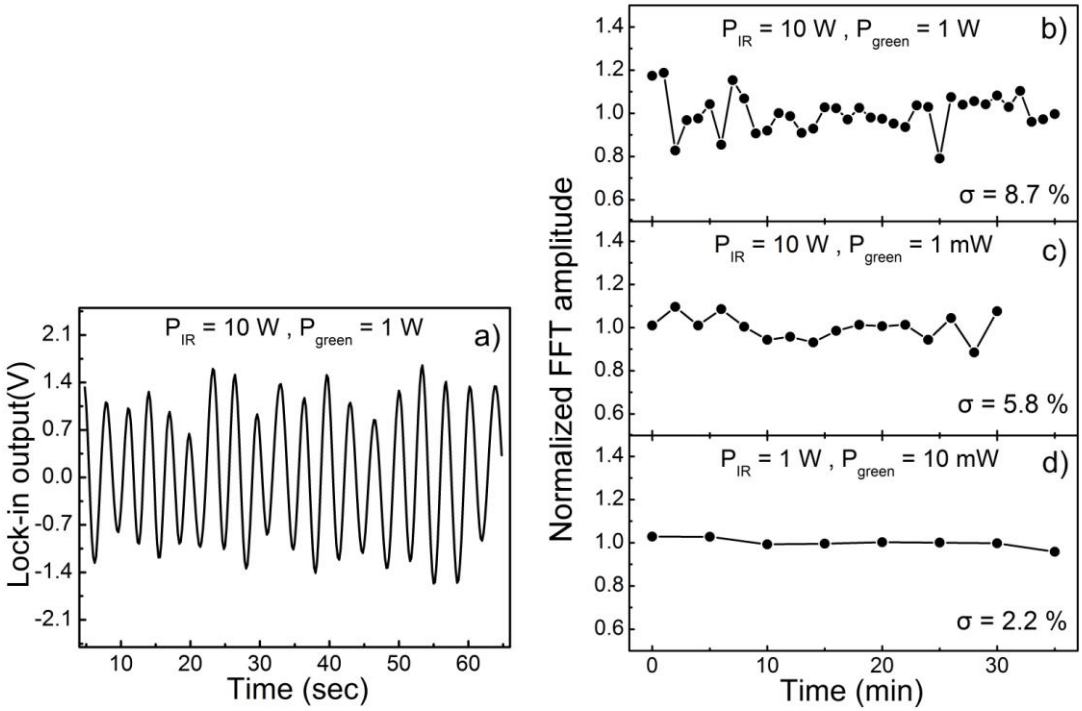

Figure 3.28: Green-green interference waveform (a) and amplitude of interference as a function of the IR power through the frequency doubling crystal and produced second harmonic (b,c,d). The parameter σ in the graphs on the right represents the standard deviation of the data points.

Although we have found that the high IR intensity is somehow responsible for the observed instabilities, we do not have a good way to reduce their level. The interference variations at half the IR power (~5W), did not show much improvement. Working at even lower IR power is inconvenient; lowering the power would decrease the SNR in the M_1 measurements considerably. Having a weaker focus in the ppLN could provide some improvement, at the expense of the available green power, but there is a limitation to how large the IR waist can be (unless the beam focus is tight, the beam gets clipped) and with the 12.5 cm lens used to focus the beam to the crystal, we are not far from it. The approach taken was to design the data acquisition routine of the experiment in such a way, so that the observed effect's influence on the measurements is reduced. This is described in section 4.1.

4. M_1 MEASUREMENTS AND RESULTS

4.1 Data acquisition scheme in the M_1 experiment

The M_1/β measurement principle was introduced in chapter 2. The 6S→7S excitation rate consists of a large two-photon rate and a small contribution owing to the two-photon and one-photon interfering pathways of the transition. This contribution appears as a modulation in the 6S→7S rate, observed as we sweep the optical phase delay between the two optical fields driving the interfering pathways of the transition. The small modulation is extracted from the overall 6S→7S signal using phase-sensitive detection, and has amplitude:

$$K(E_y) \sim 2\eta \left| A_{2PA} \right| C_{F,m}^{F,m} \varepsilon_x^{\omega_1} \sqrt{M_1^2 + \left(\beta E_y\right)^2} \tag{4.1}$$

Measurements of this amplitude at different electric fields E_y, allow a determination of M_1/β.

There is a key consideration related to the design of the data acquisition scheme. Interference data have to be acquired in such a way so that factors such as Cs density drifts, laser power fluctuations, as well as the instability in the overlap factor described earlier, have minimal influence on the measurements. Although it is possible to monitor the 540 and 1079 nm powers, calibrate the atom density, and then apply an overall correction factor to the recorded modulation, the issue of the overlap factor instability remains. This led us to the approach of using the observed interference itself as a means of calibrating the signal. To achieve this, we measured ratios of interference amplitudes, using sets of two interference scans, one taken at the electric field of interest, and another at E_y=0. The measured quantity is the ratio:

$$\frac{K(E_y)}{K(0)} = \sqrt{1+\left(\frac{\beta}{M_1}\right)^2 \left(E_y\right)^2} \qquad (4.2)$$

which does not depend on laser powers, Cs density or the beam overlap factor. As long as the set of the two scans is recorded sufficiently fast, the influence of drifts on the ratio is expected to be minimal. In addition, we expect these drifts to appear as a random fluctuation in the ratio, and not as a systematic effect. In the experiment, each pair of scans requires 20 sec (10+10), and the sequence of the electric field value is random.

4.2 Data acquisition routine and $K(E_y)/K(0)$ ratio measurements

In this section we discuss the data acquisition routine we have implemented for making an M_1/β determination. We describe in detail the signal processing performed by the program controlling the DAQ system, in order to obtain a $K(E_y)/K(0)$ from the raw modulation waveforms, the time sequence for repeated measurements of the ratio $K(E_y)/K(0)$, as well as the sequence of measurements at different electric field values that altogether combine to yield an M_1/β value.

A determination of the M_1/β ratio for a particular $(F,m_F)\rightarrow(F,m_F)$ transition consists of measurements of the ratio of (4.2) at 6 different electric field values, $\pm E_1$, $\pm E_2$ and $\pm E_3$. Approximately 24 min of total integration time is required for the run (a total of 30 min with a ~ 80% duty cycle), corresponding to 180 interference waveforms recorded, half of which are at zero field and the other half at $E\neq0$.

The sequence of the data acquisition routine yielding a single M_1/β determination is as follows: For each electric field value ($+E_1$ for instance) the field alternates between E_1 and 0 a total of 10 times, and five sets of interference waveforms are recorded, with each set consisting of an $E\neq0$ and an $E=0$ waveform. We call every such set an iteration. Every iteration yields a ratio $K(E_1)/K(0)$. The block of five iterations has an average ratio value, which is the ratio measurement for the particular block. Each block requires 100 sec, of which approximately 80 sec is acquisition time (~80 % duty cycle). After a block is completed, the field is reversed ($-E_1$) and acquisition of another block of data starts. Then, the field is switched back to $+E_1$ and so forth. A total of 6 $K(E_1)/K(0)$ ratio

measurements are made, three at $+E_1$ and another three at $-E_1$. The above process is then repeated for each of the other two sets of fields, $\pm E_2$ and $\pm E_3$. In the end of the elapsed half hour interval, we have completed 18 blocks of iterations and obtained same number of $K(E_1)/K(0)$ ratios. A least-square fit of Eq. (4.2) to the $K(E_1)/K(0)$ vs. E_y data, yields the M_1/β value for the run. The relevant data analysis is discussed in (4.3).

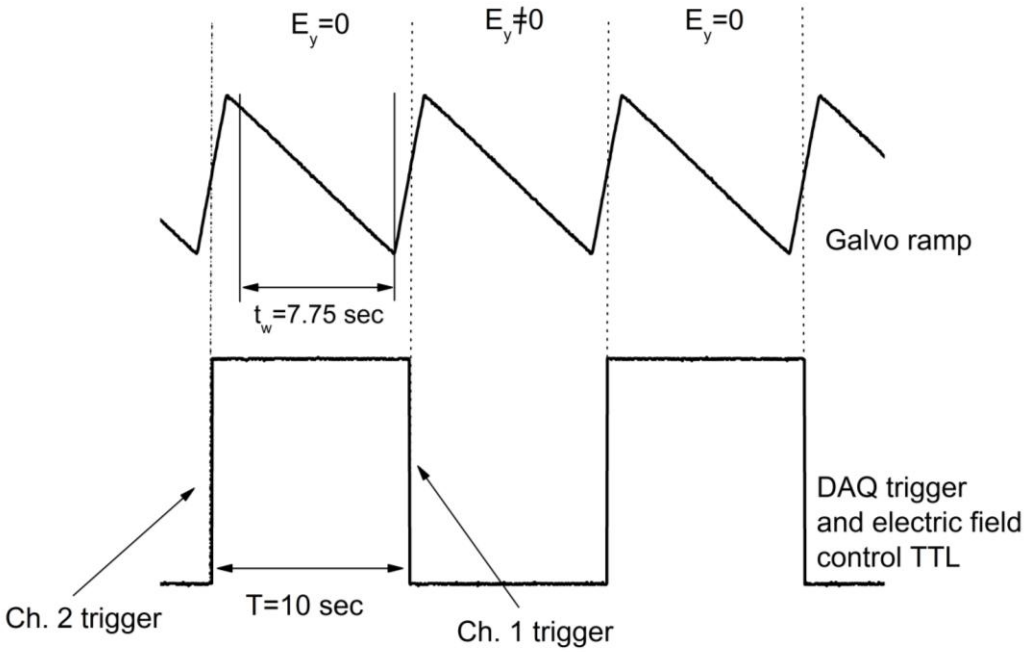

Figure 4.1: Timing sequence for the data acquisition routine

Timing for the data acquisition routine is provided by a TTL sync pulse, phase-locked to the ramp that is sent to the Mach-Zehnder galvo to sweep the 540 nm beam phase. The ramp is produced by a function generator, and the sync TTL is produced by f/2 division of the function generator sync output (using a D-type flip-flop). Figure 4.1, shows the timing sequence of the routine. The TTL controls a set of relays that either ground the plates (TTL-high), or apply voltage to them (TTL-low). One DAQ channel (Channel 1), when triggered by the TTL falling edge, samples the lock-in output and records the interference scan at $E \neq 0$. Another channel (Channel 2) is triggered by the rising edge, and records the scan at E=0. The galvo-ramp period is 10 seconds, with an 8.5 sec corresponding to the negative slope, which is the period over which the data is

acquired. The Labview program that controls the acquisition routine puts a t_w=7.75 sec window on the recorded scans, rejecting the initial 1.25 sec of sampling. This includes the first 0.25 sec of the phase-scan, allowing some time for the lock-in amplifier output to settle, following the ramp (and green beam phase) discontinuity. Sampling is done at a rate of 40 samples/sec for a total of 310 samples. Approximately 20 cycles are recorded in each interference scan (scan rate of 2.5 cycles/sec), corresponding to 16 samples/cycle. The lock-in time constant is 0.1 sec (10 Hz cut-off frequency), small enough so that the attenuation of the 2.5 Hz modulation is not significant. In order to cut down on noise picked up by the lock-in at frequencies very close to the 150 Hz of the 540 nm phase-modulation, the program filters the sampled signal through a 1.5 Hz FWHM bandwidth bandbass filter, centered on the 2.5 Hz frequency of the scan.

The slight non-linearity in the 540 nm phase-scan, (discussed in 3.13), shows up as a non-linearity in the interference scans. Because of this, the scan rates between the two extremes of the spectrum differ by ~ 11%. Following the band-pass filtering of the raw interference waveforms, the program corrects for the non-linearity, by applying a stretching transformation to the sample # n:

$$n \rightarrow n'(n)=n(1-b\cdot n) \tag{4.3}$$

n'(n) is the corrected sample # (no longer an integer), and *b* is an input to the program, that we determine in a separate experiment, by determining the value for which residuals from least square fits of sine functions to high SNR interference data are minimized. Using the same (linearized) data, an accurate measurement of the period of the interference cycles is made. The values we have determined for the 310 sample scan are: $b=1.853\cdot 10^{-4}$ $(\text{samples})^{-1}$ and T=14.729 samples. We show a set of interference waveforms, recorded at E_y=0 and E_y=75.09 V/cm in figure 4.2.

In order to compute the amplitude K of the band-pass filtered and linearized data V(n'), the program performs the Sine and Cosine Fourier Transforms of V(n') at the modulation frequency (2π/T).

$$S = \sum_{n} \mathrm{V(n')}\cdot\sin(2\pi/\mathrm{T}\cdot \mathrm{n'})\cdot\Delta \mathrm{n'} \tag{4.4}$$

$$C = \sum_{n} \mathrm{V(n')} \cdot \cos(2\pi/\mathrm{T} \cdot \mathrm{n'}) \cdot \Delta \mathrm{n'} \tag{4.5}$$

We note that the products of equations (4.5) and (4.6) include the Δn' factor since, because of the stretching transformation of (4.3), the step size in the summation is not unity.

The interference amplitude for a particular waveform is then computed from the amplitudes C and S:

$$K = \sqrt{C^2 + S^2} \tag{4.6}$$

Lastly, the program uses the set of zero and non-zero field amplitudes to compute the ratio $K(E_y)/K(0)$ of a single iteration of the data acquisition routine. The sequence of steps performed in a single iteration is displayed in figure 4.3.

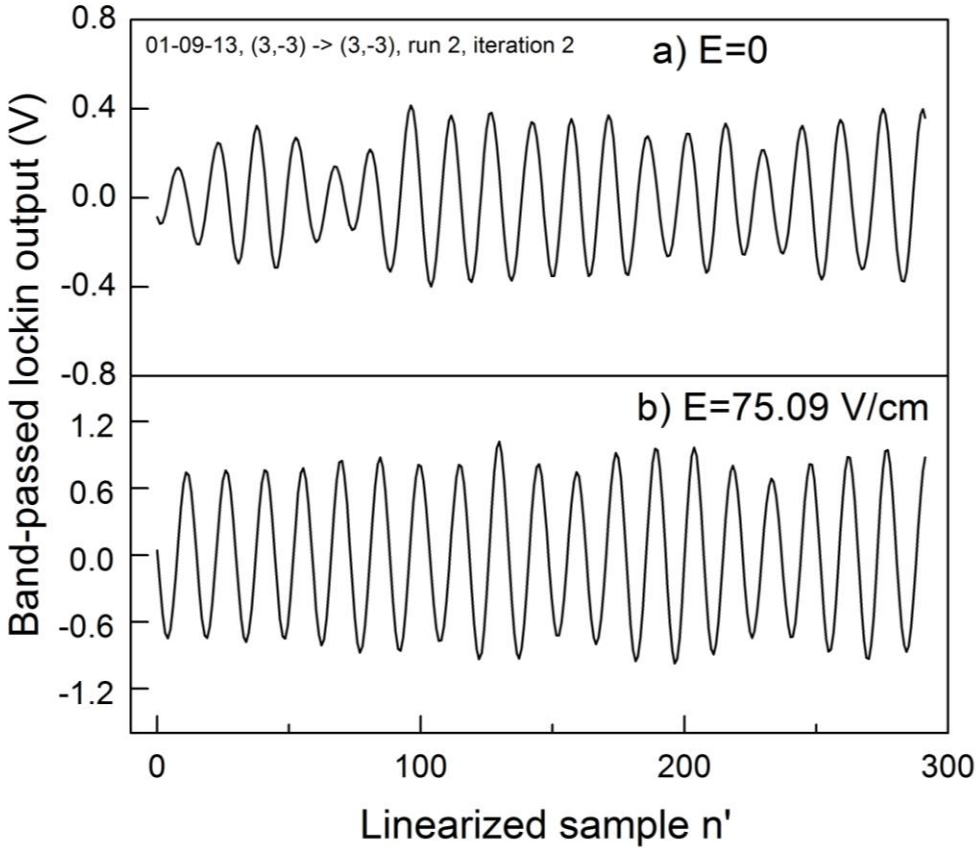

Figure 4.2: Interference waveforms, recorded for the $(F,m_F)=(3,-3)\rightarrow(3,-3)$ transition after band-pass filtering. Data shown for a) zero electric field, b) E=75.09 V/cm field. The x-axis has been linearized.

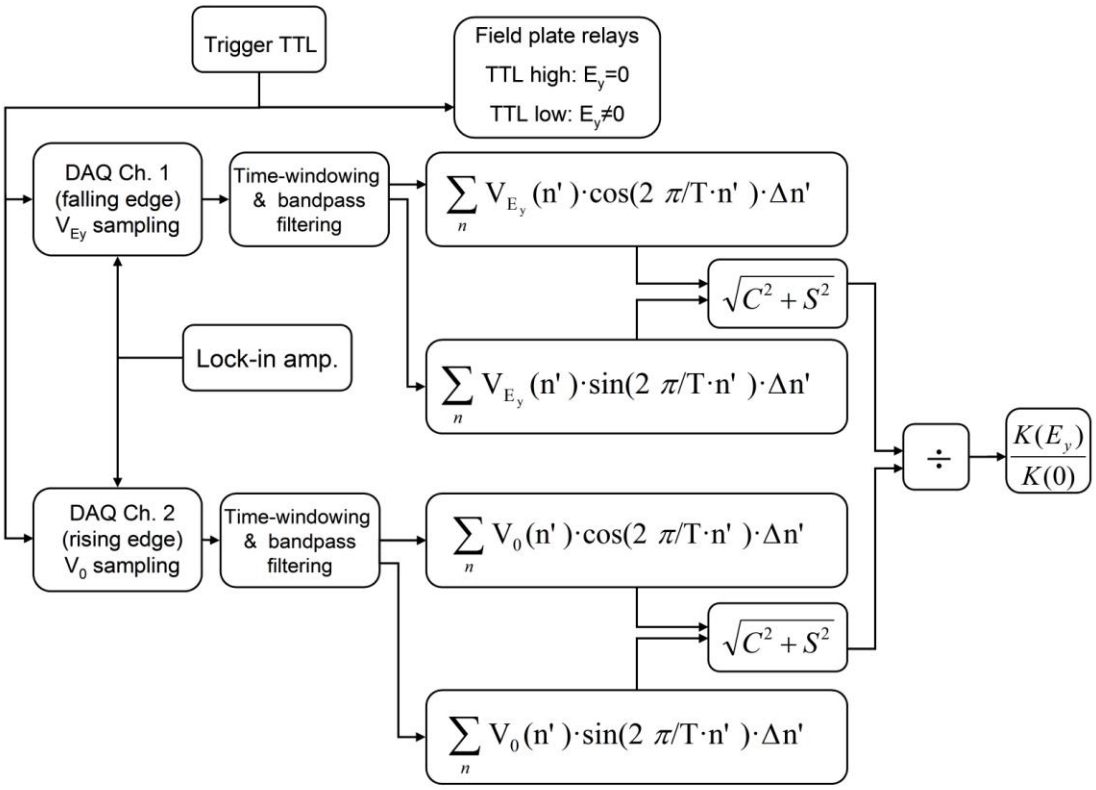

Figure 4.3: The sequence of steps for acquiring a pair of interference waveforms (at zero and non-zero electric field), subsequent signal processing, and computation of interference amplitudes and ratio $K(E_y)/K(0)$.

4.3 Determination of M_1/β

In this section we describe the analysis of data acquired in order to determine the M_1/β ratio. We also present our analysis results and our final determination for M_1/β.

We have made a total of 16 determinations of the M_1/β ratio, in four different days, in the course of two weeks, and for all possible initial states (F,m_F) of the 6S→7S transition. In the first two days of data acquisition, we took interference measurements on the F=3→F=3 component of the transition. In each of these days, we made a total of 4 M_1/β determinations, alternating the initial state of the transition between opposite m_F levels in the following sequence: -3, +3, -3,+ 3. In the last two days of the experiment, we switched to the F=4 initial state, and took another 4 M_1/β runs per day, with the following sequence for the initial state m_F: -4, +4, -4, +4. Each of the 16 runs, as already

mentioned, requires approximately 30 min with the uncertainty in the individual M_1/β determination in the 1-1.5 % range. The approach of making measurements in different days, and under different conditions for the 1079 and 540 nm beam overlap, allowed us to test the stability of the apparatus by verifying agreement between results from different days.

The amplitude of the modulation in the 6S→7S rate, due to the two-photon and weak amplitude interference is:

$$K(E_y) = 2\eta \left| A_{2P} \right| \varepsilon_x^{\omega_1} C_{F,m}^{F,m} \sqrt{\left(M_1 + \alpha E_x / C_{F,m}^{F,m} \right)^2 + \left(\beta E_y \right)^2} \tag{4.7}$$

The α-Stark term $aE_x\varepsilon_x^{\omega_1}$ needs to be retained in the above expression, since its contribution, although small, is not negligible compared to M_1. All other contributions to the overall weak amplitude are products of two or three field misalignments, so their magnitude is negligible. Our data acquisition system measures ratios $K(E_y)/K(0)$, which in this case can be written in the following form:

$$\frac{K(E)}{K(0)} = \sqrt{\left(1 - \frac{aE\sin\xi}{M_1 C_{F,m}^{F,m}} \right)^2 + \left(\frac{\beta}{M_1} E\cos\xi \right)^2} \tag{4.8}$$

In the above ratio, we have expressed the fields E_x and E_y in terms of the true field E, generated by the field plate assembly, and the (small) angle ξ representing the slight misalignment between the 540 nm beam direction of propagation (defining the y-axis) and E. $E=V/d$, where V is the electric field plate voltage and d the plate separation.

The parameter ξ is expected to vary from day to day, due to two reasons. First, some adjustment in the orientation of both optical beams is usually required, in order to minimize the Doppler-offset in the atom beam resonance. This is done with the concave mirror focusing the two beams in the interaction region, while scanning the 1079 nm laser and observing the relative frequency shift between our reference Cs cell and the atom beam resonance. In addition, the overlap of the 540 with the 1079 nm beam needs to be optimized on a daily basis, resulting in a variability of the apparatus y-axis with respect to E.

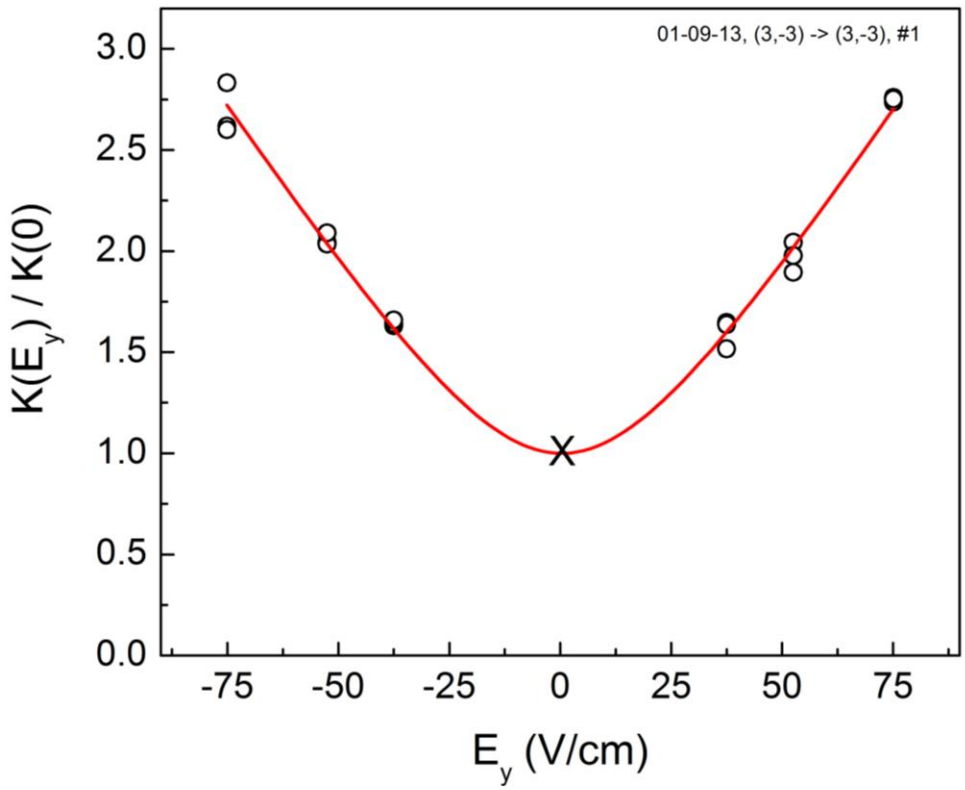

Figure 4.4: Plot of ratio $K(E_y)/K(0)$ vs. E_y. The data run corresponds to one of the 16 determinations of $|M_1/\beta|$ made in the experiment. A hyperbolic function least square fit to the data (solid red curve), yields a determination for M_1/β . For the data shown: $|M_1/\beta|=29.78 \pm 0.29$ V/cm.

A determination of M_1/β for each of the 16 runs of the experiment is obtained through a least squares fit of the hyperbolic function (4.8) to the 18 $K(E)/K(0)$ vs. E data points of the run. The two parameters to be determined by the fitting routine are ξ and $|\beta/M_1|$. We note that the fit yields the absolute value of M_1/β. The sign of this quantity is negative, as determined in a separate experiment, described in section (4.4). The fit parameter $\alpha / M_1 C_{F,m}^{F,m}$ is fixed, but its value varies between the different initial (F,m_F) states. $C_{F,m}^{F,m} = -m_F / 4$ for F=3 and $+m_F / 4$ for F=4. Using our best estimate for the distribution of atoms among the various m_F levels (92% in the extreme m, 5% in the m_F-1, 3% in the m_F-2), we compute an average value: $C_{F,m}^{F,m} = \mp 0.72$ for the initial (3,±3) states, and $C_{F,m}^{F,m} = \pm 0.97$ for the (4,±4) states. In addition, we use an approximate value

for $M_1/\beta \approx 29.5$ V/cm and the known ratio $\alpha/\beta \approx 9.9$, to obtain $\alpha / M_1 C_{F,m}^{F,m} = \mp$ 0.467 for (3,±3) and $\alpha / M_1 C_{F,m}^{F,m} = \pm$ 0.346 for (4,±4). An example of a set of K(E)/K(0) ratio data from a single run of the experiment along with the corresponding least square fit is shown in figure 4.4. Figure 4.5 is a plot of all the obtained $|M_1/\beta|$ determinations.

We show in table 4.1 the average values of M_1/β, as determined for each of the four initial states (F,m_F) of the 6S→7S transition. The χ^2 for each of these values is ~ 1, indicating that the four measurements of each initial state are consistent with each other. We obtain the value of - 29.55 ± 0.10 V/cm as our overall determination for M_1/β. The χ^2 for this value is 1.04, which corresponds to a ~ 40% probability that the sample of 16 M_1/β measurements comes from a random distribution. The statistical uncertainty of 0.10 V/cm or ~ 0.3 % is larger than the combined systematic uncertainty of 0.05 V/cm. The average values of the other free parameter of the fit, the angle ξ, are also listed in Table I. The overall average value $\bar{\xi} = -3.2$ *mrad*, is indicative of the accuracy with which the field plate assembly is oriented with respect to the atom beam direction of propagation. The 1.6 mrad variation in $\bar{\xi}$ corresponds to a Doppler-shift of ~ 1 MHz, and reflects the limit of precision in the procedure of nulling the Doppler-shift of the atom beam resonance.

Table 4.1: Averaged results and statistical uncertainties of the M_1/β measurements for the four different initial states, and of the combined set.

(F,m)	M_1/β (V/cm)	χ^2	ξ (mrad)
(3,-3)	-29.76 (18)	0.87	-2.41 (0.85)
(3,+3)	-29.40 (19)	0.96	-5.13 (0.97)
(4,-4)	-29.65 (25)	1.18	-0.93 (1.64)
(4,+4)	-29.31 (23)	1.12	-2.76 (1.56)
All	-29.55 (10)	1.04	-3.2 (1.6)

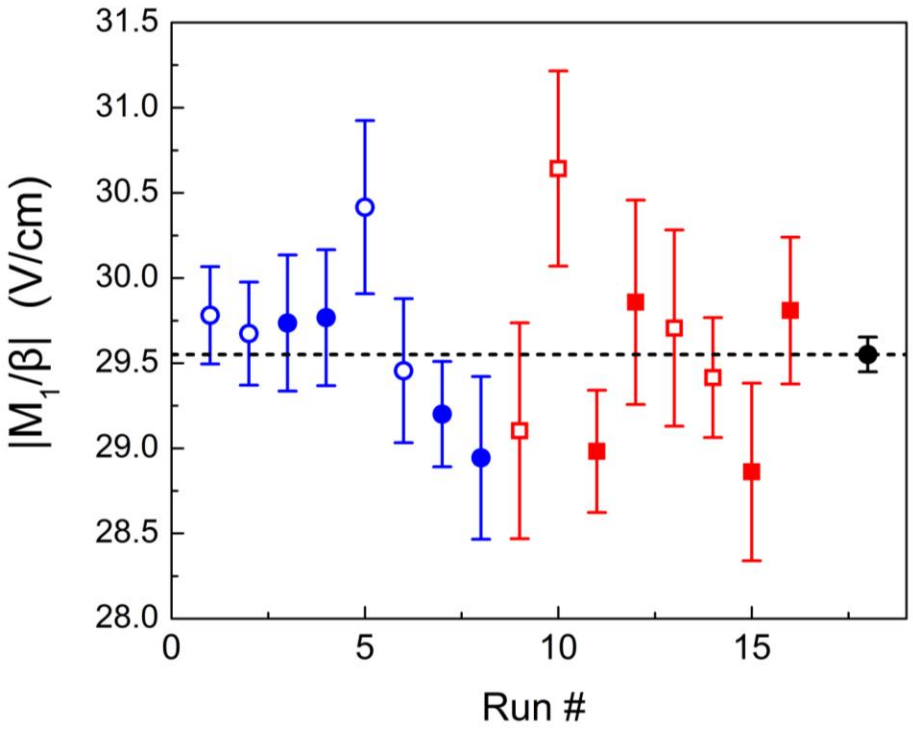

Figure 4.5: The 16 determinations of $|M_1/\beta|$. The dashed line represents the weighted average, also indicated by the solid black circle on the far right. Open circles represent measurements on the $(F,m_F)=(3,-3)$ initial state and closed circles on the $(3,+3)$ state. Open squares are measurements on the $(F,m_F)=(4,-4)$ initial state and closed squares on the $(4,+4)$ state. The error bars indicate the 1σ uncertainty.

4.4 Determination of the sign of M_1/β

The sinusoidal modulation observed in the 6S→7S excitation rate has an overall phase determined by two contributions. The first is the weighted optical phase-difference between the phase-coherent fields driving the interfering path ways of the transition. The second is a phase factor determined by the relative amplitudes of the in-phase and out-of phase component of the weak amplitude of the transition. This phase factor is a function of the Stark-field applied to the atoms. The overall phase of modulation is:

$$\varphi = \Delta\varphi + \delta\varphi(E_y) \tag{4.9}$$

where

$$\Delta\phi = 2\phi^{\omega_2} - \phi^{\omega_1} \tag{4.10}$$

and $$\delta\varphi(E_y) = \tan^{-1}\left[\frac{\beta E_y}{M_1 + aE_x / C_{F,m}^{F,m}}\right] \quad (4.11)$$

are the weighted optical phase difference and the Stark-dependent phase-shift, respectively. Sweeping the phase-difference $\Delta\varphi$ has allowed us to make observations of the modulation in the 6S→7S rate, as a means of determining the magnitude of M_1/β. In this section we describe a supplemental experiment, in which we make measurements of $\delta\phi(E_y)$ *vs.* E_y, as a means of determining the sign of M_1/β.

The method of measuring $\delta\phi(E_y)$ relies on recording sets of two interference waveforms, one at $E_y=0$ and another at $E_y\neq0$, and determining the relative phase-shift between the two. The experimental procedure is as follows: We ramp the 540 nm beam phase (at a rate of ~ 0.3 Hz) and record a total of 40 waveforms, alternating between zero and non-zero electric field. Each waveform consists of approximately 3 cycles of modulation. The data acquisition program averages the 20+20 waveforms to obtain a set of two high SNR waveforms. We show an example of such a set in figure 4.6. The process is then repeated for another E_y , for a total of 13 different electric fields, of both positive and negative value.

The analysis of the recorded data is straightforward. We fit a sine function to each of the two averaged waveforms corresponding to a particular E_y, through which we determine the relative phase-shift $\delta\phi(E_y)$. We show a plot of the 13 $\delta\phi(E_y)$ vs. E_y data points in figure 4.7. Based on equation (3), we expect $\delta\phi(E_y)<0$ for $E_y>0$ and $\delta\phi(E_y)<0$ for $E_y<0$, if $M_1/\beta<0$. Opposite signs for $\delta\phi(E_y)$ are expected if $M_1/\beta>0$. As it is clearly determined from the plot, M_1/β is a negative quantity.

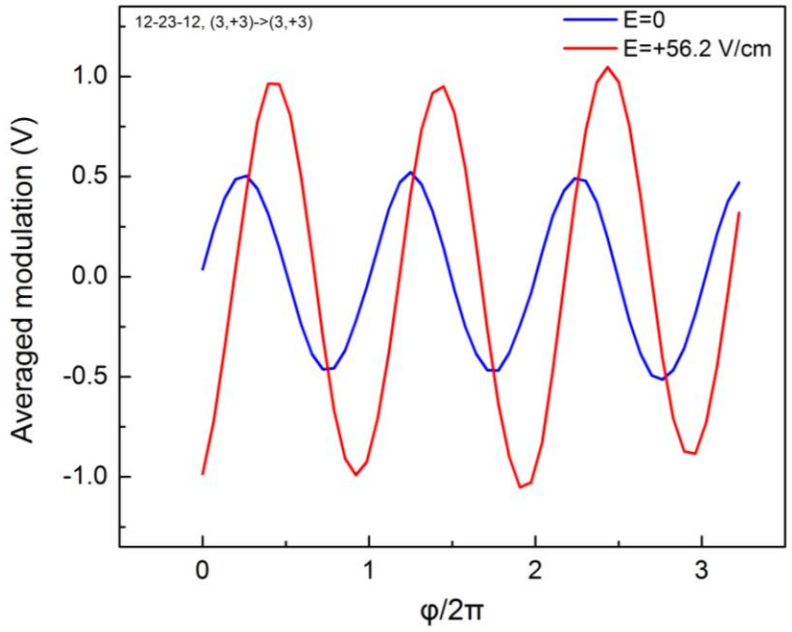

Figure 4.6: A set of averaged interference waveforms, obtained for $E_y=0$ and $E_y\neq0$. List square fits of sine functions to the data are used to determine the phase-shift $\delta\varphi(E_y)$ vs. E_y.

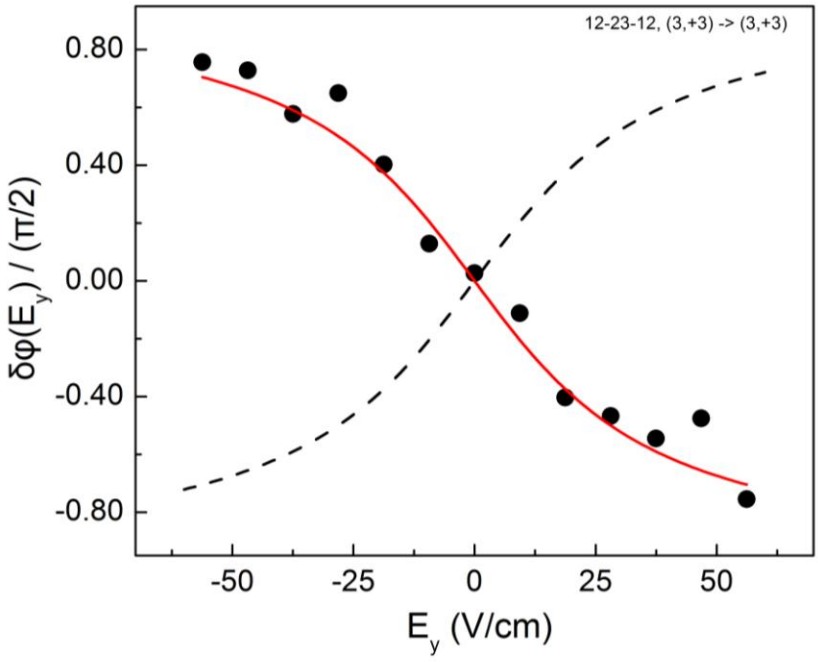

Figure 4.7: Plot of the measured phase-shifts $\delta\varphi(E_y)$ vs. E_y. The red solid curve is an inverse tangent fit to the data of the form of Eq. (4.11), neglecting the small αE_x term. The dashed curve is a simulation of the same function for the case of $M_1/\beta > 0$.

4.5 Final result for M_1

In this section we compare our M_1/β result to previous determinations, provide our result for the magnetic dipole moment and compare this to other determinations of the same quantity.

On table 4.2 we compare our M_1/β measurement to previous determinations of the same quantity. Each of these determinations was made on the F=3→4 and F=4→3 transitions, while in this work we employed the F=3→3 and F=4→4 transitions. With the exception of the value reported in [30], there is very good agreement between the existing measurements and ours.

Table 4.2: Comparison of our M_1/β result to existing determinations. The error in our value is the combined systematic and statistical uncertainty.

Group	M_1/β (V/cm)
Hoffnagle *et al.*, ref [30][a]	26.2 (1.7)
Bouchiat *et al.*, ref [29]	-29.55(45)
Gilbert *et al.* , ref [28]	-29.73(34)
Bennett *et al*, ref [23]	-29.48(7)
Present work	-29.55(11)

[a]Measurement of the M_1/β magnitude

The value of the magnetic dipole transition moment M_1 is obtained using our M_1/β result and the known vector polarizability $\beta=26.99(5)\ \alpha_0^3$. We obtain $M_1=-4.251(16)\cdot10^{-5}$ $|\mu_B/c|$. As a comparison of this determination to previously made ones, we list in table 4.3 all the M_1 measurements obtained from the M_1/β values of table 4.3. We also include in table 4.3, a pair of two earlier determinations, one coming from a measurement of the M_1/α ratio[27] and another, direct (i.e. non interfering) determination of M_1[30]. Table 4.3 also lists two calculations for the magnetic dipole moment. The most recent of these predicts a value of $M_1= -\ 3.58\cdot10^{-5}$ $|\mu_B/c|$. Since the calculation of this moment is challenging, this value is in reasonable agreement with the weighted average of the four most recent laboratory determinations (including ours), which is $M_1=-4.245(8)\cdot10^{-5}$ $|\mu_B/c|$.

Table 4.3: Comparison of the M_1 result of the present work to existing determinations. The error in our value is the combined systematic and statistical uncertainty.

Group	M_1 (10^{-5} $\lvert\mu_B/c\rvert$)
Laboratory measurements	
Bouchiat *et al.*, ref[27][a]	3.7(3)
Hoffnagle *et al*., ref[30][b]	3.77(24)
Gilbert *et al.* , ref [28]	-4.277(49)
Bouchiat *et al.*, ref[29]	-4.251(54)
Bennett *et al*, ref[23]	-4.241(10)
Present work	-4.251(16)
Theory	
Dzuba *et al*., ref [25]	-5.6
Sakunov *et al.*, ref[26]	-3.58

[a] Determined through a measurement of M_1/α
[b] Direct measurement of M_1

4.6 Signal to Noise Ratio and statistical uncertainty of the M_1/β measurement

The combined uncertainty in the M_1/β determination (systematic and statistical) of ~ 0.37% is dominated by the statistical contributions (0.33%). The systematic uncertainty (~0.16%) contributes significantly less to the overall error of the determination. In this section we make estimates for the Signal to Noise ratio (SNR) in the detection of the interference signal, and show that the projected statistical uncertainty for the M_1/β determinations for the given amount of integration time is in reasonable agreement with the actual statistical errors of the determinations.

The modulation in the 6S→7S rate due to the two-photon-M_1 interference is approximately $2\cdot10^{-4}$ of the two photon rate. In the F=3→3 transition, the observed modulation amplitude is about 130 μV on top of a ~700 mV two-photon background, and in the F=4→4 transition the modulation amplitude is ~55 μV with on top of a ~ 250 mV two-photon rate. The ratio of this amplitude to the overall noise, measured (in units μV/√ Hz) at the frequency at which the lock-in detection of the modulation is done, is a

measure for the SNR in one second of integration(in √ Hz). Since the detected signal is sinusoidaly varying, we use the rms amplitude of the modulation (amplitude/√2) for estimating the SNR.

The estimated SNR in the modulation detection can be used to make a prediction for the expected measurement uncertainty after a given integration time *t*. The SNR grows as $\sqrt{t}$, and therefore the projected uncertainty goes as SNR/$\sqrt{t}$. Our apparatus measures ratios of waveform amplitudes at both zero and non-zero electric fields (with 50% of integration time spent on E=0 and the other 50% on one of three different field values). For this reason, in the present analysis we will start with the SNR of a single ratio measurement, and use the $\sqrt{n}$ dependence of the cumulative SNR on the number of ratio measurements *n*, to predict the final SNR of the M_1/β measurement. We will do this separately for the 720 ratio measurements made on the F=3→3 transition and the 720 made on the F=4→4. The SNR of a single ratio is essentially the inverse of the uncertainty in the ratio:

$$SNR_{Ratio} = \frac{1}{\sigma_{Ratio}} = \frac{1}{\sqrt{\left(1/SNR_{E=0}\right)^2 + \left(1/SNR_{E\neq 0}\right)^2}} \tag{4.12}$$

where $SNR_{E=0}$ and $SNR_{E\neq 0}$ are the SNRs obtained for the measurement of the K(0) and K(E≠0) amplitudes, respectively. Each of these is $\sqrt{8\text{sec}}$ times the SNR obtained in 1 sec of integration (8 seconds is the duration of each waveform scan). We make measurements at different electric fields, so the value of (4.12) varies slightly, but it is on average $\sim 0.9 \cdot SNR_{E=0}$. SNR_{Ratio} is only slightly lower than $SNR_{E=0}$, which is reasonable, since the E≠0 waveforms have larger SNRs, and therefore do not contribute significantly to the ratio uncertainty.

Table 4.4 lists separately for the F=3→3 and F=4→4 transitions the predicted uncertainty in the M_1/β measurements (estimated from the projected overall SNRs for these), as well as the actual uncertainty of the measurements. The actual error is about 30 % greater that the prediction of our SNR analysis, which is reasonable agreement, considering that some drifts between the various measurements are not unreasonable to expect. One source of such drifts could be for instance the slight instability of the 1079

and 540 nm beam overlap in the interaction region (discussed in 3.17), which is hard to quantify and include in the SNR analysis.

Table 4.4: Predicted vs. actual M_1/β statistical uncertainty, listed separately for the measurements made on the F=3→3 and F=4→4 transitions. The estimation of the overall SNR for the two determinations follows the discussion of this section.

Day & transition	Day 1 F=3→3	Day 2 F=3→3	Day 3 F=4→4	Day 4 F=4→4
RMS amplitude of modulation (μV)	90	105	39	36
Noise level (μV/√Hz)	24	21	12	11
Measured SNR in 1 sec (√Hz)	3.8	5	3.3	3.3
<SNR> in 1 sec (√Hz)	4.4		3.3	
Estimated <SNR> for a ratio measurement	11.2		9.3	
Total number of ratio measurements *n*	720		720	
Predicted SNR after *n* measurements	303		225	
Predicted M_1/β uncertainty	0.33%		0.44%	
Actual statistical uncertainty	0.44%		0.57%	

4.7 Systematic contributions to the measurement uncertainty

The potential systematic contributions to the overall error of the M_1/β measurement fall into three categories. The first includes instrumental errors, such as these related to the error in the determining the electric field applied to the atoms, instrumental uncertainties in measuring the modulation waveforms, etc. This class of errors contributes by the largest proportion to the overall systematic uncertainty. The second includes potential errors related to unwanted contributions to the amplitude of the modulation signal, arising from stray static fields, imperfections in the optical and static field alignment etc. The third includes potential contributions to the signal from a small amplitude modulation present in the 540 nm field, introduced by the galvo-plate. In the following sections we discuss the contributions of each of these categories. We show that

the errors of the second and third categories do not contribute significantly to the uncertainty of the M_1 measurement. Table 4.5 lists the main sources of systematic uncertainty in the measurements and the contribution of these to the combined systematic error.

Table 4.5: List of main sources of systematic uncertainties and their contribution to the overall systematic error.

Source of uncertainty	Relative error
Field plate spacing	0.14%
Voltage measurement	0.035%
DAQ input channels nonlinearity	0.07%
All	0.16%

4.7.1 Instrumental uncertainties

The largest contribution of this class comes from the uncertainty in the knowledge of the Stark field applied to the atoms. There are two factors contributing to this: The finite accuracy with which the plate separation is measured, and the instrumental error in measuring the voltage applied to the plates. The plate spacing was measured with calipers, and the combined error due to the measurement variability and the calipers uncertainty is 0.14%. The voltage uncertainty is a few times smaller. It is mainly due to the slight fluctuations in the field-plate voltage (0.034 %) and also due to the error in measuring the voltage. The Agilent 34401A digital multimeter used for this has a specified uncertainty of ~ 0.01 % for the range of applied voltages in the experiment.

The second largest instrumental contribution is due to the error in recording the modulation waveforms at E=0 and E≠0. Since each of these waveforms is recorded by a different channel of the data acquisition system, and because the experiment measures the amplitude ratio of the two waveforms (K(E)/K(0)), variations in the level recorded by the two channels, will introduce an error in the ratio. We have studied these variations by measuring with each DAQ channel the amplitude of a stable and well known DC level V,

for a range of V values. This allows us to establish a calibration curve $V_1(V)$ and $V_2(V)$ for the channels 1 and 2 respectively. We find that for the range of voltages V_i inputted to channel 1 and V_j inputted to channel 2 in the experiment, the ratio $V_1(V_i)$ / V_2 (V_j) is always equal to V_i /V_j to within less than 0.07%. We conservatively consider this value to be the systematic error in the M_1/β measurement due to the relative variations between the two channels.

4.7.2 Effect of stray fields and field misalignments

In this section we study the systematic contributions to the M_1/β measurements arising from stray DC electric and magnetic fields present in the interaction region, as well as from misalignment of the DC fields or the optical polarization $\varepsilon^{\omega 1}$ with respect to the coordinate system of the experimental apparatus. We show that these contributions are negligible at the level of accuracy achieved in the experiment. In order to be systematic in this study, we develop a formalism that can be applied to the analysis of the systematic errors of the M_1 experiment, as well as to the future PNC work.

We express the total transition amplitude in the following general form:

$$\sum \mathrm{A} = A_{2P} + \{a_R + b_R V\} + i\{a_I + b_I V\} \tag{4.13}$$

To determine the coefficients α_R, b_R, α_I, b_I of the total weak amplitude we need to return to the expressions we introduced in (2.2) for the M_1, Stark and PNC amplitudes. Eq. (4.13) involves components depending on the voltage V that creates the Stark field applied to the atoms, as well as terms independent of V. The total electric field in the interaction region is of the form $E=\Delta E_i + \kappa_i V/d$, where i can be x,y, or z. ΔE_i represent components of any stray electric field present (no dependence on V). This field can be for instance due to patch effects in the field plates. The coefficients κ_i quantify the misalignments in the electric field. For the M_1 geometry, in the absence of any misalignments $\kappa_y=1$ and $\kappa_x=\kappa_z=0$. Although we work with linear polarization for the $\varepsilon^{\omega 1}$ driving the weak transitions, we write the optical field (dropping the superscript) in its

most general form ε'+iε'', in order to include the effect of a slight ellipticity in the beam polarization.

In the expression for the interference signal that we used in our data analysis (4.7,4.8), we did not consider a possible misalignment of the field **B** with respect to the apparatus z-axis. Such a misalignment is responsible for mixing between adjacent magnetic sublevels, through the components B_x and B_y. The additional terms introduced to the weak amplitude are not of significant magnitude at the level of accuracy achieved in the M_1 measurement, so the approximation of perfect **B** alignment is valid, but we are now going to include these terms in the expression for the total amplitude. To derive these terms, we need to consider the mixing of adjacent m_F components through the Zeeman splitting $\Delta E = g_F m_F \mu_B B$, induced by the B_x and B_y fields:

$$\left|\overline{ns^2 S_{1/2},F,m}\right\rangle = \left|ns^2 S_{1/2},F,m_F\right\rangle + \frac{B_x + iB_y}{g_F} C_{F,m}^{F,m-1}\left|ns^2 S_{1/2},F,m_F - 1\right\rangle + \frac{B_x + iB_y}{g_F} C_{F,m}^{F,m+1}\left|ns^2 S_{1/2},F,m_F + 1\right\rangle \tag{4.14}$$

where g_F is the Lande factor and the coefficients $C_{F,m}^{F,m\pm1}$ are defined in [17]. The above expression includes mixing between m_F levels, but not between different hyperfine levels F, an approximation which is valid for the modest magnetic field present in these experiments.

The coefficients α_R, b_R, α_I, b_I, can be shown to be in their most general form:

$$\begin{aligned}\alpha_R = {} & \alpha\left(\Delta E_x\varepsilon_x' + \Delta E_y\varepsilon_y' + \Delta E_z\varepsilon_z'\right) - \beta\left(\Delta E_x\varepsilon_y'' - \Delta E_y\varepsilon_x''\right)C_{F,m}^{F,m} \\ & - M_1\left(k_x\varepsilon_y' - k_y\varepsilon_x'\right)C_{F,m}^{F,m} + \frac{B_y}{B_z}C_{F,m}^{F,m}\left[-\beta\left(\Delta E_y\varepsilon_z' - \Delta E_z\varepsilon_y'\right) - M_1\left(k_x\varepsilon_z'' - k_z\varepsilon_y''\right)\right] \\ & + 8\frac{B_x}{B_z}\left[\left(C_{F,m+1}^{F,m}\right)^2 + \left(C_{F,m-1}^{F,m}\right)^2\right]\left[-\beta\left(\Delta E_y\varepsilon_z'' - \Delta E_z\varepsilon_y''\right) - M_1\left(k_y\varepsilon_z' - k_z\varepsilon_y'\right)\right]\end{aligned} \tag{4.15}$$

$$\begin{aligned}b_R = {} & \left\{a\left(\kappa_x\varepsilon_x' + \kappa_y\varepsilon_y' + \kappa_z\varepsilon_z'\right) - \beta\left(\kappa_x\varepsilon_y'' - \kappa_y\varepsilon_x''\right)C_{F,m}^{F,m}\right. \\ & \left. - \beta\left(\kappa_y\varepsilon_z' - \kappa_z\varepsilon_y'\right)\frac{B_y}{B_z}C_{F,m}^{F,m} - \beta\left(\kappa_y\varepsilon_z'' - \kappa_z\varepsilon_y''\right)8\frac{B_x}{B_z}\left[\left(C_{F,m+1}^{F,m}\right)^2 + \left(C_{F,m-1}^{F,m}\right)^2\right]\right\}d^{-1}\end{aligned} \tag{4.16}$$

$$
\begin{aligned}
a_I = {} & a\left(\Delta E_x \varepsilon_x^{''} + \Delta E_y \varepsilon_y^{''} + \Delta E_z \varepsilon_z^{''}\right) + \beta\left(\Delta E_x \varepsilon_y^{'} - \Delta E_y \varepsilon_x^{'}\right) C_{F,m}^{F,m} \\
& - M_1\left(k_x \varepsilon_y^{''} - k_y \varepsilon_x^{''}\right) C_{F,m}^{F,m} + \mathrm{Im}(E_{PNC}) \varepsilon_z^{'} C_{F,m}^{F,m} \\
& + \frac{B_y}{B_z} C_{F,m}^{F,m}\left[-\beta\left(\Delta E_y \varepsilon_z^{''} - \Delta E_z \varepsilon_y^{''}\right) - M_1\left(k_x \varepsilon_z^{'} - k_z \varepsilon_y^{'}\right)\right] \\
& + 8\frac{B_x}{B_z}\left[\left(C_{F,m+1}^{F,m}\right)^2 + \left(C_{F,m-1}^{F,m}\right)^2\right]\left[\beta\left(\Delta E_y \varepsilon_z^{'} - \Delta E_z \varepsilon_y^{'}\right) - M_1\left(k_y \varepsilon_z^{''} - k_z \varepsilon_y^{''}\right)\right]
\end{aligned}
\tag{4.17}
$$

$$
\begin{aligned}
b_I = {} & \left\{a\left(\kappa_x \varepsilon_x^{''} + \kappa_y \varepsilon_y^{''} + \kappa_z \varepsilon_z^{''}\right) + \beta\left(\kappa_x \varepsilon_y^{'} - \kappa_y \varepsilon_x^{'}\right) C_{F,m}^{F,m}\right. \\
& \left. + \beta\left(\kappa_y \varepsilon_z^{''} - \kappa_z \varepsilon_y^{''}\right)\frac{B_y}{B_z} C_{F,m}^{F,m} + \beta\left(\kappa_y \varepsilon_z^{'} - \kappa_z \varepsilon_y^{'}\right) 8\frac{B_x}{B_z}\left[\left(C_{F,m+1}^{F,m}\right)^2 + \left(C_{F,m-1}^{F,m}\right)^2\right]\right\} d^{-1}
\end{aligned}
\tag{4.18}
$$

It is useful to place some limits on some of the quantities appearing in (4.15-4.17). For instance, although we define the y-axis as the direction propagation of the optical field, we allow the wavevector **k** to have k_x and k_z components, to include the effect of beam divergence. It happens that k_z is not present in the expressions (4.15-4.17), since it does not contribute for the $\Delta m_F=0$ transitions we work with. We can however place an upper limit on the value of k_x, based on an estimate for the maximum half-angle beam divergence ($\lambda/\pi w_0$), where w_0 =130 μm is the beam waist at the beam focus. This half-angle is ~1.3 mrad, and we can therefore allow a maximum of $1.3\cdot10^{-3}$ for the k_x component. The optical field in the *M_1* experiment is primarily in the x-direction. But due to the effect of focusing, a small ε_y component should be present as well. We can place a constraint on this, using the minimum radius of curvature of the wavefronts within the ~ 1 cm interaction region, which we estimate to be R ~ 2 m. Based on this, we can place the limit $\varepsilon_y/\varepsilon_x < (w_0/R)=10^{-4}$. The ε_z component of the field can be greater, since its value depends on how carefully the polarization axis of the beam is aligned with the x-axis of the coordinate system, and we find it reasonable to use an estimate of $\varepsilon_z/\varepsilon_x=0.01$ for the present analysis. In the future PNC work, more careful alignment can constrain ε_z even further. Finally, we require estimates for the coefficients κ_i, which represent the alignment between the Stark-field and the optical beam direction of propagation. Since

the y-axis is the beam propagation axis, $\kappa_y \approx 1$. In addition, κ_x is essentially the angle ξ used in the hyperbolic function fits of (4.8) which we determined to be on average -3.2 mrad. As for the κ_z parameter, this cannot be determined from the data, but we can use a reasonable estimate of 0.01 for the present analysis.

The lock-in detection process in the experiment detects the interference of the two-photon with the net weak amplitude, which has amplitude:

$$K(V) = A_{2P}\left[\left(a_R + b_R\right)^2 + \left(a_I + b_I V\right)^2\right]^{1/2} \tag{4.19}$$

The vertex of K(V) is at:

$$V_{\min} = -\frac{a_R b_R + a_I b_I}{b_R^2 + b_I^2}\ ,\ K_{\min} = A_{2P}\frac{\left|a_I b_R - a_R b_I\right|}{\sqrt{b_R^2 + b_I^2}}$$

K(V) can be written in terms of V_{min}, K_{min} as:

$$K(V) = \left[A_{2P}\left(b_R^2 + b_I^2\right)\left(V - V_{\min}\right)^2 + K_{\min}^2\right]^{1/2} \tag{4.20}$$

In the absence of any field misalignments or stray fields, $K \sim \sqrt{M_1^2 + \left(\beta E_y\right)^2}$ and M_1/β can be obtained as the ratio of the minimum K (for E=0) to the slope of K at high electric fields. In the more general case, described by (4.20), we can use the same ratio to obtain an approximate value of M_1/β :

$$R = \frac{K_{\min}}{\lim\limits_{V\to\infty}\frac{dK}{dV}d} = \frac{\left|a_I b_R - a_R b_I\right|}{\left(b_R^2 + b_I^2\right)d} \tag{4.21}$$

As intuitively expected, the smaller the contributions to K(V) due to the unwanted effects, the better the approximation will be. We can write R in the following form:

$$R = \frac{\left|a_R\right|}{\left|b_I\right|d}\left[\frac{1 - \left|a_I b_R / a_R b_I\right|}{1 + b_R^2 / b_I^2}\right] \tag{4.22}$$

α_R and b_I include the dominant terms M_1 and βE_y. A measurement of R can be precisely matched to M_1/β as long as the secondary contributions in α_R and b_I are negligible and the ratio in the bracket is unity. These conditions can be expressed as:

1. $b_R^2 / b_I^2 << 1$
2. $\left|a_I b_R / a_R b_I\right| << 1$

3. $\beta\varepsilon_x^{'}C_{F,m}^{F,m}d^{-1} >>$ all other terms in b_I

4. $M_1\varepsilon_x^{'}C_{F,m}^{F,m}d^{-1} >>$ all other terms in α_R.

We now examine the above conditions, keeping in mind that the primary field components are E_y, B_z, and $\varepsilon_x^{'}$. We also assume that the optical field ε_x has no out-of-phase component ($\varepsilon_x^{"} = 0$).

1. The primary contribution to b_I is $\beta\kappa_y\varepsilon_x^{'}C_{F,m}^{F,m}d^{-1} \sim \beta\varepsilon_x^{'}d^{-1}$ and the largest term in b_R is $a\kappa_x\varepsilon_x^{'}d^{-1}$.Therefore $b_R^2 / b_I^2 = (a/\beta)^2(\kappa_x/\kappa_y)^2 / \left(C_{F,m}^{F,m}\right)^2 \approx 10^{-3}$. This 0.1% contribution of the b_R^2 / b_I^2 term does not contribute significantly to M_1/β determination, at the ~0.37 % level of the overall accuracy achieved in the experiment.

2. To make an estimate for the quantity $|a_I b_R / a_R b_I|$, we consider the ratios b_R / b_I and a_I / a_R separately. As discussed in 1, $b_R^2 / b_I^2 \sim 10^{-3}$ and so $b_R / b_I \sim 0.03$. Regarding a_I / a_R, we expect that the largest contribution in α_I comes from $\beta\Delta E_y\varepsilon_x^{'}C_{F,m}^{F,m}$ while the dominant term in α_R is $M_1\varepsilon_x^{'}C_{F,m}^{F,m}$. Therefore $a_I / a_R \sim \Delta E_y / (M_1/\beta)$. In the discussion of condition 4, we use experimental data to make an estimate of ~ 10 mV/cm for stray fields in the interaction region. We use this value to obtain an estimate of $\sim 3\cdot 10^{-4}$ for a_I / a_R. Combining the two ratio values we discussed, we conclude that $|a_I b_R / a_R b_I| \sim 10^{-5}$ and so condition # 2 is easily satisfied.

3. The terms in b_I with the larger potential magnitude, aside from $\beta\varepsilon_x^{'}C_{F,m}^{F,m}d^{-1}$, are the ones proportional to α. These terms arise in the presence of a small ellipticity in the optical polarization, expressed by the components ε''. These components though are expected to be much smaller than the in-phase amplitudes ε' by $\sim 10^{-4}$, since we work with linear polarization. Therefore the secondary contributions to b_I are less than 10^{-4} in magnitude compared to the main term $\beta\varepsilon_x^{'}C_{F,m}^{F,m}d^{-1}$ and condition # 3 is satisfied.

4. We expect that the larger term in α_R aside from the dominant $M_1\varepsilon_x' C_{F,m}^{F,m} d^{-1}$ is $\alpha\Delta E_x\varepsilon_x'$, whose origin is a stray field ΔE_x. The amplitude of the signal detected in the presence of this term is $\sqrt{\left(M_1 - \alpha\Delta E_x / C_{F,m}^{F,m}\right)^2 + \left(\beta E_y\right)^2}$ and the stray field is expected to shift the apparent M_1 value. Fortunately, the term switches sign under m_F reversal, since $C_{F,m}^{F,m} = \pm m_F / 4$ (+ for F=4, - for F=3). This allows us to estimate ΔE_x by comparing M_1/β measurements taken for opposite m_F levels. The difference should be equal to $2\alpha\Delta E_x / \beta \left| C_{F,m}^{F,m} \right|$. Using the data of table 4.1, we obtain ΔE_x=+14(9) mV/cm for the F=3→3 transitions, and ΔE_x=-17(17) mV/cm for the F=4→4 transitions. Combining these values we obtain an average of +7(8) mV/cm. This stray field is sufficiently small, so that it doesn't contribute to the α_R term, in comparison with $M_1\varepsilon_x' C_{F,m}^{F,m} d^{-1}$.

To conclude the above analysis, we have shown that the systematic contributions of unwanted effects to the M_1/β measurements appear to be insignificant at the level of accuracy achieved in our experiment. Such contributions will become much more important and necessary to address in the PNC measurements. The type of analysis presented in this section will be applicable in these experiments as well.

4.7.3 Effect of amplitude modulation in the 540 nm field

The galvo-plate sweeping the 540 nm phase in the Mach-Zehnder interferometer creates an unwanted amplitude modulation in the 540 nm optical field. As discussed in section 3.13, this is due to an etalon effect present in the plate and results in a sinusoidal variation of the green power level as the galvo-plate is scanned. The amplitude of this modulation is 0.4% of the mean power, or 0.2 % in the field amplitude. Because of the dither in the galvo-angle imposed as part of the lock-in detection of the interference signal, a slight amplitude modulation is present at the dither frequency as well. Both types of the amplitude modulation (slow modulation due to the galvo sweep and fast dither of the amplitude) could introduce a systematic error in the determination of the amplitude of the recorded waveforms. In this section we study this effect and show that its contribution to the signal is negligible.

In the presence of both phase and amplitude-modulation, the interference term in the excitation rate takes the form:

$$W_i = K\left[1 + r\cos\left[m_a\cos\left(\omega_m t + \varphi_0\right) + \lambda\omega_g t + \varphi_1\right]\right]\cos\left[m_p\cos\left(\omega_m t\right) + \omega_g t\right] \qquad (4.23)$$

In the above expression K is an overall constant factor that includes the amplitude of modulation K(E_y) that we seek to measure. r=0.002 is the fractional modulation of the 540 nm field amplitude, ω_m is the dither frequency(~$2\pi\cdot$150 Hz) , m_a and m_p are the (not necessarily equal) depths of modulation entering the expressions for the amplitude and phase dither respectively, and φ_o and φ_1 are undetermined phases. $\omega_g t$ represents the sweeping phase delay in the 540 nm field, imposed by the rotating galvo plate (for our conditions $\omega_g \approx 2\pi\cdot$2.5 Hz). The parameter λ is included to account for the possibility of unequal number of modulation cycles in the green beam amplitude and phase for a given rotation of the galvo plate. This possibility arises since amplitude modulation involves phase-shifts internal to the galvo-plate, while the overall green beam phase delay involves shifts both internal to the plate and shifts occurring due to the changing path around the plate. In practice, we observe approximately equal number of phase and amplitude cycles for a given angle sweep, so $\lambda \approx 1$, but we nevertheless include λ in the analysis. It is convenient to express W_i in terms of the following two quantities:

$$P = \cos\left[m_p\cos\left(\omega_m t\right) + \omega_g t\right] \qquad (4.24)$$

$$A = \cos\left[m_a\cos\left(\omega_m t + \varphi_0\right) + \lambda\omega_g t + \varphi_1\right] \qquad (4.25)$$

Using these, the interference term can be written as:

$$W_i = K\left[1 + rA\right]P \qquad (4.26)$$

In the absence of any amplitude modulation r=0, and the only modulation in W_i is the phase modulation, expressed by the P term. P and A can be expanded in a harmonic

series using expansions formulas for cos(mcos(*x*)) and sin(mcos(*x*)) that involve Bessel functions (Eq. 3.5,3.6). P and A can be expressed as:

$$P = \sum_{n=0}^{\infty} P_n \cos\left(n\omega_m t\right) \tag{4.27}$$

$$A = \sum_{k=0}^{\infty} A_k \cos\left(k(\omega_m t + \varphi_0)\right) \tag{4.28}$$

The first few coefficients of the above expansions are:

$$P_0 = J_0(m_p)\cos(\omega_g t),\ P_1 = -2J_1(m_p)\sin(\omega_g t),\ P_2 = -2J_2(m_p)\cos(\omega_g t),\ P_3 = +2J_3(m_p)\sin(\omega_g t)$$

and:

$$A_0 = J_0(m_a)\cos(\lambda\omega_g t + \varphi_1), A_1 = -2J_1(m_a)\sin(\lambda\omega_g t + \varphi_1), A_2 = -2J_2(m_a)\cos(\lambda\omega_g t + \varphi_1)$$
$$A_3 = +2J_3(m_a)\sin(\lambda\omega_g t + \varphi_1)$$

The lock-in amplifier mixes W_i with the phase reference $\cos(\omega_m t+\varphi_{ref})$ (so that the 1st harmonic of the modulation is detected) and low-passes their product. φ_{ref} represents the relative phase between the first harmonic in the expansion of the P term, (which is of the form $P_1\cdot\cos(\omega_m t)$) and the lock-in phase reference. To obtain optimum signal this phase is adjusted so that $\varphi_{ref}\approx 0$. We now compute the product $W_i\cdot\cos(\omega_m t)$, whose DC component is the lock-in output. Our goal is to examine the contributions present in the lock-in output when $r\neq 0$. Inserting the expansions for P (4.27) and A (4.28), $W_i\cdot\cos(\omega_m t)$ becomes:

$$W_i\cos(\omega_m t) = K\left[1 + a\left[\sum_{k=0}^{\infty} A_k \cos\left(k(\omega_m t + \varphi_0)\right)\right]\right]\left[\sum_{n=0}^{\infty} P_n \cos\left(n\omega_m t\right)\right]\cos(\omega_m t) \tag{4.29}$$
$$= K\left[\sum_{n=0}^{\infty} P_n \cos\left(n\omega_m t\right)\right]\cos(\omega_m t) + Ka\left[\sum_{k=0}^{\infty} A_k \cos\left(k(\omega_m t + \varphi_0)\right)\right]\left[\sum_{n=0}^{\infty} P_n \cos\left(n\omega_m t\right)\right]\cos(\omega_m t)$$

The first term of the sum has a single DC component $(K/2)P_1$ or $(K/2)J_0(m_p)\cos(\omega_g t)$. This term is responsible for the observed modulation in the excitation rate, occurring as the 540 nm phase $\omega_g t$ is scanned. The second term, proportional to *r*, gives rise to the unwanted contributions to the modulation waveforms. Calling this term S_A, we have:

$$S_A = \frac{Ka}{4}\left[\sum_{k=0}^{\infty} A_k \cos\left(k(\omega_m t + \varphi_0)\right)\right]\left[\sum_{n=0}^{\infty} P_n \cos\left(n\omega_m t\right)\right]\cos(\omega_m t) \tag{4.30}$$

$$= \frac{Ka}{4}\sum_{k,n} P_n A_k \cos\left(n\omega_m t\right)\cos\left(k(\omega_m t + \varphi_0)\right)\cos\omega_m t$$

$$= \frac{Ka}{4}\sum_{k,n} P_n A_k \left\{\cos\left((n+k+1)\omega_m t + k\varphi_0\right) + \cos\left((n+k-1)\omega_m t + k\varphi_0\right)\right.$$

$$\left. + \cos\left((n-k+1)\omega_m t - k\varphi_0\right) + \cos\left((n-k-1)\omega_m t + k\varphi_0\right)\right\}$$

The DC terms of S_A are these which satisfy the conditions $n+k=1$ or $|n-k|=\pm 1$. The DC part of the series is of the form:

$$S_A^{DC} = \frac{Ka}{4}\left(2P_0A_1\cos\varphi_0 + 2P_1A_0\cos\varphi_0 + P_2A_1\cos\varphi_0 + P_1A_2\cos 2\varphi_0\right. \tag{4.31}$$

$$\left. + P_3A_2\cos 2\varphi_0 + P_2A_3\cos 3\varphi_0 + \ldots\right)$$

The terms of S_A^{DC} are products of coefficients P_i and A_j, which are 1st order harmonics of $\omega_g t$ and $\lambda\omega_g t$ respectively. Therefore, each of the $P_i \cdot A_j$ products in S_A^{DC} oscillates at the sum and difference frequencies: $\omega_g(\lambda \pm 1)$, and since $\lambda \approx 1$, these frequencies are approximately 0 and $2\omega_g$. We therefore conclude that the effect of the amplitude modulation in the 540 nm field is to introduce small amplitude (because r is small) harmonics (with frequencies ≈ 0 or $\sim 2\omega_g$) to the interference waveforms. These harmonics lie on top of the signal due to the much larger modulation at ω_g.

There are quite a few reasons for why the effect of the amplitude modulation is negligible. First, since r is small, the amplitude of all the $\omega_g(\lambda \pm 1)$ harmonics will also be small, compared to the amplitude of the $\omega_g = 2\pi \cdot 2.5$ Hz modulation. In addition, the signal processing of the recorded waveforms includes a bandbass filter than rejects frequencies outside the 2.5 ±0.75 Hz range, followed by a Fourier transform at 2.5 Hz, that further attenuates the $2.5(\lambda \pm 1)$ Hz components. Finally, any residual contribution of these harmonics to the Fourier transform will simply add by a small amount to an overall

multiplicative factor in the amplitude $\sqrt{M^2+\left(\beta E_y\right)^2}$ measured in the experiment. Since we perform ratio measurements $K(E_y)/K(0)$, and the multiplicative factor is common to both amplitudes, the measurement is unaffected.

5. FUTURE DIRECTIONS TOWARDS A PNC MEASUREMENT

5.1 Introduction

The M_1 experiment presented in the previous chapters showed that our Coherent Control detection technique is suitable for weak moment measurements. The effort initiated with the demonstration of the weak signal amplification in M. Gunawardena's thesis [48], and continued here with measurement of the magnetic dipole transition moment, will now focus on a new determination of the extremely weak PNC moment in Cs. In this last chapter, we discuss the future directions of the project, as it moves towards the measurement of the PNC effect in the 6S→7S transition. We start with a discussion of the possibilities for enhancing the apparatus detection sensitivity, in order to reach the SNR level required for a successful PNC measurement. Then, we discuss the anticipated systematic contributions to the PNC signal, and lay out a scheme for addressing the systematic that we expect to contribute the most to the measurement. Finally, we propose an alternative PNC measurement on $6S_{1/2}\rightarrow 5D_{3/2}$ transition, for which the PNC moment is expected to be larger than the 6S→7S moment.

5.2. Enhancing the Signal to Noise Ratio

The M_1 experiment has a signal to noise ratio of about $4\ \sqrt{\text{Hz}}$. The size of the E_{PNC} is $\sim 5\cdot 10^{-5}\cdot M_1$. In its present state, our apparatus would achieve a PNC SNR of $\sim 2\cdot 10^{-4}\sqrt{\text{Hz}}$. A substantial SNR increase is necessary for the PNC experiment to be feasible. In this section we present various possibilities that we have identified for enhancing the atom beam apparatus detection sensitivity.

5.2.1 Power buildup cavity to enhance 540 nm power

The largest increase in the weak signal amplitude will come from enhancing the power of the 540 nm light in the interaction region, with the use of a power buildup cavity. Since the weak signal is linear in the 540 nm field amplitude, the signal enhancement goes as the square root of the intra-cavity circulating intensity. A large

power buildup is required in order to significantly enhance the PNC signal. For this purpose, a build-up cavity was employed in the Cs Boulder experiments [5,11,49], as well as in the Berkeley Yb experiment [50]. In these experiments, the cavity was a standing-wave design. In our experiment, in order to be able to control the 1079 and 540 nm phase-difference, it is necessary to work with a traveling wave cavity.

A power buildup cavity is a Fabry-Perot interferometer, designed specifically to maximize the power circulating in it. The buildup cavity finesse F, and the associated power buildup factor (defined as the ratio of the power circulating in the cavity to the power incident to it), need to be as high as possible in order to obtain a large PNC signal, which is proportional to the 540 nm field amplitude. The latest Cs experiment incorporated a cavity with F=100,000 which corresponds to a 30,000 buildup of power ($\approx F/\pi$), where as in the Yb experiment, an F=9,000 cavity was used. Such finesse values are possible through advances in dielectric coating technology, that allow fabrication of mirror coatings with reflectivities greater than 99.999% and absorption and scattering losses that can be at the sub-part per million level. One downside of working with higher finesses is that the cavity resonance frequency is more sensitive to external perturbations, so an elaborate mechanical and laser lock design is required to obtain mechanical isolation from its environment and good frequency stability, respectively. Nevertheless, since a large SNR improvement is required in order to bring the possibility of a PNC experiment within reach, an effort should be made to maximize the buildup for the 540 nm light. Assuming a buildup factor similar to the one of the Boulder experiment can be achieved, the SNR enhancement factor in the PNC signal will be ~170.

Figure 5.1 shows the geometry of a simple traveling wave cavity that could be used to enhance the 540 nm laser power. It consists of two concave and a plane mirror. The mirrors are highly-reflective at 540 nm but not at 1079 nm, since no buildup of power is required for the IR. A relatively small angle of incidence for the 540 nm beam at the concave mirrors is necessary in order to minimize astigmatism which will make the beam slightly elliptical and affect the overlap efficiency with the IR beam in the interaction region. The angle of incidence will be limited by the electric field plates in the interaction region, also shown in figure 5.1. Understanding the effect of the astigmatism on the green and IR overlap efficiency should be among the first steps in the cavity geometry design.

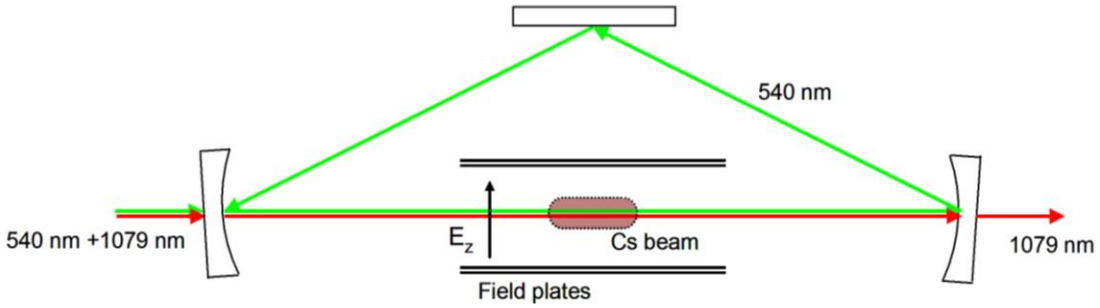

Figure 5.1: Proposed power build-up cavity for enhancing the weak signal in the PNC experiment.

5.2.2 Increasing the atom beam density

The PNC signal to noise ratio could be increased with a higher atom beam density. The M_1 experiment is not shot-noise limited, so increasing the density would not improve the SNR substantially, but assuming shot-noise limit is reached in the PNC experiment, then SNR would increase with density (it increases as the square root of density).

In the present experiment, the estimated density of $5\text{-}10 \cdot 10^{+9}$ cm^{-3} is at a level that seems to be affecting the degree of spin-polarization of the atoms. Presently, about 92% of atoms can be pumped to the extreme Zeeman sublevel, a fraction that increases at lower beam densities. The PNC experiment using the α-Stark transition (see discussion in 2.3.2) relies on an accurate measurement of the average m_F level of the population. The fewer the atoms in the extreme level, the higher the precision required in measuring the different m_F populations, to obtain a given accuracy in $\langle m_F \rangle$. So, although a further increase in the beam density would help with SNR, it would at the same time result in an increased error in $\langle m_F \rangle$. Therefore, the possibility of increasing the atom beam density should be studied in parallel with efforts to increase the degree of spin-polarization. If the latter can be further improved, then working with higher beam fluxes is meaningful.

It would be interesting to investigate by how much the degree of spin-polarization can be increased using a Zeeman clean up beam. The Zeeman beam would need to overlap the hyperfine cleanup, as it does in the optical pumping region. The process would ideally take place close to the interaction region, as close as the available optical access permits. Since the Zeeman pumping (see section 3.8) requires

Δm=+1 or -1 transitions, the two optical beams would have to propagate in the z-direction (vertical), parallel to the local magnetic field. No major modifications to the apparatus are required for this, except for adding an optical window to the chamber lid, through which the two beams can enter the chamber, pointing in the vertical direction.

If a larger fraction of atoms can be put into the extreme m_F level, then the accuracy requirement in measuring the population distributions with the Raman laser will become less severe. This might also allow us to increase the Cs density and enhance the weak signal measurement. A density increase by a factor of 2, would result in an SNR increase (in a shot-noise limited detection) by a factor of $\sqrt{2}$.

5.2.3 Possibility of improving the atom beam collimation

The 6S→7S resonance width in the atom beam is approximately 14 MHz, limited by Doppler-broadening due to the slight transverse velocity of the Cs atoms. The broadening results in a decrease of the effective Cs density in the interaction region, since only the fraction of atoms with Doppler-shifts within the transition natural linewidth Γ≈3.3 MHz can undergo excitations. It is desired to increase this fraction, by improving the atom beam collimation. In the M_1 experiment, a more collimated beam would provide a resonance width closer to the natural linewidth. In the presence of a buildup cavity however, as the case will be in the PNC experiment, the gain in signal would be limited. This is because the presence of the intense intracavity field is going to cause broadening of the transition through the ac-Stark effect. Therefore, even a perfectly collimated beam, will have a resonance linewidth greater than Γ. In the Boulder experiment, the ac-Stark effect was a limiting factor for the transition linewidth. It is not easy to predict how large the broadening will be in our PNC apparatus. This will depend on the intracavity field intensity. Therefore, it is worth considering possible options for improving the collimation of the atom beam.

An efficient means of beam collimation is by transverse laser cooling of the atoms. This is a process similar to slowing atoms in an optical molasses, where repeated absorption cycles force atoms to slow down. However, due to the amount of fluorescence emitted from the cooling process, using on-resonant light would affect the spin-polarization of atoms. S. Bennett's Thesis [51] includes a demonstration of the transverse cooling of the Boulder experiment Cs beam, by use of an intense

standing wave field at 852 nm, off-resonant from the D_2 line. Most of the atoms are cooled to within the 3.3 MHz of the natural linewidth. In that experiment, the gain due to cooling was limited due to the broadening caused by the ac-Stark effect. Although the optical setup involves a buildup cavity for the cooling light, this possibility might be interesting for our apparatus. As in the Boulder experiment, the overall gain in the effective density will depend on the level of the ac-Stark broadening.

The degree of beam collimation in our apparatus is primarily determined by the oven nozzle. A different nozzle would offer a different degree of collimation. The nozzle is a pack of hypodermic tube needles, which are ~ 1cm long, and ~0.8 mm in internal diameter. This corresponds to a 12.5 length-to-diameter aspect ratio. The authors of [52] reported on an experimental and theoretical comparison of the degree of collimation and density in a Cs beam between nozzles of different aspect ratios. They show that the higher aspect ratios provide tighter collimations, but lower beam densities (and vice versa). In order to recover the same level of beam density, an increase in the oven temperature is necessary, which results in a greater beam divergence, and so the gain from the higher aspect ratio is decreased. Therefore, trying a nozzle with higher aspect ratio in our apparatus would probably not increase the effective density by a whole lot.

We have attempted to improve collimation using two different collimators. These collimators were made of microscope cover slips (thickness ~ 0.15 mm) and were placed approximately 10 cm downstream from the oven nozzle. In one of these, the cover slips spacing was ~0.2 mm and in the other 0.5 mm. The narrow collimator did provide a much narrower beam divergence (6 MHz linewidth,) but it also decreased the beam density by a factor of 5-6, so there was no actual gain from the collimation. The less narrow collimator resulted in a slight decrease in the beam density, without any observable improvement in the resonance linewidth. As a conclusion, there seems to be no gain in the effective Cs density by using a collimator.

5.2.4 Reducing the 6S→7S detection noise

Aside from enhancing the weak signal amplitude, it is equally important to reduce the noise in the detection of the signal. In the M_1 experiment, the noise level in

the detection has roughly the same contributions of shot noise due to the two-photon rate, and technical noise from the lasers (mainly frequency noise) as well as noise from the background of atoms in the state the detection takes place. Since the measurement accuracy increases as the square root of integration time, it is important in the PNC experiment to work with shot-noise limited detection. This will require the total reduction in combined noise due to the lasers and the background by a factor of 2-3. With shot-noise limited detection, the total improvement in noise level will be a factor of 2.

The requirement for a quiet 1079 nm laser will be satisfied by locking the 540 nm light (generated by frequency doubling of 1079 nm) to the high finesse build-up cavity. One convenient possibility is a triple stage lock, with optical feedback from a Fabry-Perot to narrow the 1079 linewidth to the ~10 kHz range [40], and electronic feedback to the laser current (or to an AOM that frequency-shifts the laser output), to stabilize the generated 540 nm field to the cavity resonance. The cavity in turn would be stabilized to the Doppler-free resonance in the reference cell. Since this cavity will have a very narrow linewidth (kHz level) and the atomic resonance is on the order of 15 MHz, we expect that the laser frequency noise contribution to the 6S→7S noise will be negligible. Already through the single stage lock of the laser to the ~ 6 MHz Doppler-free two-photon resonance in a cell, the lock is quiet enough, so that no changes in the 6S→7S detection noise are observed when the (fast) current feedback to the laser is disengaged. This fact permits us to be able to project that the 1079 nm laser noise will not contribute to the noise level. Finally, the 4 ppm√Hz 1079 nm amplitude noise (whose contribution to the 6S→7S noise is ~ 8 ppm√Hz), is at a level (1/2 of shot noise) where it probably does not need to be addressed.

The 852 nm detection laser frequency noise (~15 ppm√Hz at 150 Hz) is the largest contributor to the 6S→7S noise identified in the M_1 experiment. A better lock to the saturation absorption (SA) signal is required to reduce this level. A minimum of a factor of 2 improvement is necessary to make the noise level small compared to the 6S→7S shot-noise. This will require improving the SNR in the error signal obtained from the spectrum, and probably a faster feedback loop too. The construction of the circuit used in the M_1 experiment (which is almost identical for all 5 lasers), did not include a careful design of the loop's overall gain vs. frequency profile. A more careful design, based on principles described in [53] for instance, ought to provide

better laser noise performance. An alternative to the direct lock to SA peaks could be a dual stage lock, in which the first stage is a lock to a Fabry-Perot cavity, followed by cavity stabilization to the SA spectrum. Since a cavity can provide much narrower linewidths than the ~12 MHz of the SA peaks, significant noise reduction should be expected with the two-stage lock.

Improvement in the hyperfine laser lock may be necessary as well. Although we have not characterized its noise performance, since the overall 6S→7S noise does not change depending on whether the laser lock is tight or not, it is reasonable to think that the laser's contribution to the noise is small. Noise in the hyperfine laser will cause fluctuations in the background of atoms in the almost depleted F state probed by the detection laser. Since this background is a few times smaller than the two-photon rate, the hyperfine laser noise should have a smaller effect than the same noise level present in either the detection of the 1079 nm laser. However, since improvement in the detection laser noise is required anyway, the changes made to the latter could be easily applied to the hyperfine laser as well.

The background of atoms in the nominally depleted F state (~0.15% of the atoms in the beam), contributes somewhat (mainly with its shot noise), to the overall 6S→7S noise. A reduction in this background will help decrease the noise level slightly. The background is primarily due to re-absorption of fluorescence in the optical pumping region. Working with lower Cs densities helps decrease this background, but in a shot-noise limited experiment, a lower density would result in a smaller signal to noise ratio for the weak signal detection. In the M_1 experiment, the large size electric field plates, parallel to the optical windows of the chamber, prevented us from using a second hyperfine clean up beam close to the interaction region, to further reduce the background. Access through this window will probably be possible in the PNC experiment, due to the different plate geometry requirements.

5.2.5 Conclusion

In this section we conclude our discussion about the possibilities of enhancing the detection sensitivity of our apparatus with an estimate for the SNR enhancement we anticipate to achieve, in order to make the measurement of the extremely weak PNC moment feasible.

We list in table 5.1 three sources of improvement that are likely to result in an enhancement of the weak signal detection sensitivity. The first is the 540 nm power build up cavity. Assuming a build up factor of 30,000, the resulting weak signal (and SNR) enhancement is $\sqrt{30,000} \approx 170$. The second source of improvement comes from a reduction in the 6S→7S detection noise, that, as discussed, will result in a shot-noise limited detection and an overall noise reduction by a factor of 2. The last SNR source of improvement we assume is an increased Cs beam density. Assuming a factor of 2 increase, the resulting SNR enhancement will be $\sqrt{2}$. Of course all these enhancements factors are simply estimates. The actual enhancement from each of the sources listed in table 5.1 is yet to be explored. Other potential sources, discussed in the previous sections but not listed here, may also contribute to the detection sensitivity.

Table 5.1: Sources of detection sensitivity improvement and associated SNR enhancement factors.

Source	SNR enhancement
540 nm build up cavity (30,000 enhancement)	170
Detection noise reduction (factor of 2)	2
Atom beam density (factor of 2)	$\sqrt{2}$
Overall enhancement	480

Currently, the average SNR (in 1 sec) in the M_1 signal detection is ~ 3.8 √Hz. The PNC moment is ~ 20,000 smaller than M_1. The projected 480 factor improvement in the apparatus detection sensitivity corresponds to a PNC detection SNR of approximately 0.09 √Hz. At this level, a 1% determination of the PNC moment will require ~ 340 hours of integration time. This is a long time, but not an unrealistic possibility. The 1% determination is sufficient for a check of the Boulder experiment anapole moment result. However, for a more precise determination of the weak charge than that of the Boulder experiment (target accuracy <0.3%), more than 3,000 hrs of integration is required. This is unpractical, and further enhancement of the apparatus sensitivity than our estimate in this section will be required.

5.3 Control of systematics in the PNC signal-Build up cavity as a polarizer

The PNC experiment will be more challenging than the M_1 experiment, with respect to understanding and handling properly the systematic contributions to the weak signal. This is due to the much smaller size of this moment, relative to M_1 ($\sim 5\cdot 10^{-5}$). The systematic contributions to the signal can arise from misalignments of the static electric and magnetic fields present in the interaction fields, stray static fields, and potential misalignment of the 540 nm polarization axis, as well as potential impurities in the nominally linear 540 polarization. An understanding of the relative importance of the anticipated systematic contributions, require us to perform the same analysis presented in section 4.7.2 for the case of the M_1 experiment. Repeating this analysis here is beyond the scope of this discussion, but the analysis shows that for reasonable field misalignments and stray fields, most of the systematic contributions, are of a small enough magnitude so that they do not contribute significantly.

There is a systematic contribution to the PNC signal however that will be challenging to address. It involves the M_1 moment, and it arises from a 540 nm field polarization impurity. In the proposed E_{PNC} measurement scheme (2.3.2), in the absence of any systematic contributions, the amplitude of modulation is:

$$K(E_z) = 2\left|A_{2P}\right|\varepsilon_z^{'}\sqrt{\left(\alpha E_z\right)^2 + \left(Im(E_{PNC})\, C_{F,m}^{F,m}\right)^2} \tag{5.1}$$

$\varepsilon_z^{'}$ is the in-phase component of the 540 nm field, whose polarization is nominally linear and aligned with the z-axis. The presence of an out-of-phase component $\varepsilon_x^{''}$, will introduce a systematic $-M_1 C_{F,m}^{F,m}\varepsilon_x^{''}$ that adds in-phase to the Im(E_{PNC}) term, resulting in an amplitude of modulation:

$$K(E_z) = 2\left|A_{2P}\right|\varepsilon_z^{'}\sqrt{\left(aE_z\right)^2 + \left(Im(E_{PNC}) - M_1\frac{\varepsilon_x^{''}}{\varepsilon_z^{'}}\right)^2\left(C_{F,m}^{F,m}\right)^2} \tag{5.2}$$

Addressing this systematic will require a very high degree of polarization purity. Since Im(E_{PNC}) /M_1 $\approx 5\cdot 10^{-5}$, a ratio $\varepsilon_x^{''}/\varepsilon_z^{'} << 5\cdot 10^{-5}$ will be required to render this systematic insignificant.

We can use the 540 nm power build-up cavity, discussed in 5.2.1, as a high quality polarizer for the 540 nm field, to obtain a highly linear polarization. The idea is to exploit the fact that in a traveling wave cavity, the different phase shifts upon reflection for the s and p modes of the field, result in different resonant frequencies

for the two modes [54]. When one mode is resonant, the other is not. In our case, locking the 540 nm field to the p mode (z-polarization) will result in a very high extinction for the unwanted ε_x'' component, corresponding to the off-resonant s mode.

The degree of extinction for the unwanted polarization is related to the cavity transmission:

$$T(\nu_\Delta) = \frac{T_{\max}}{1+\left(\frac{2F}{\pi}\right)^2 \sin\left(\frac{\pi\nu_\Delta}{FSR}\right)} \tag{5.3}$$

where T_{max} is the resonant transmission, F is the finesse of the mode, ν_Δ is the detuning from resonance and FSR is the cavity free spectral range. The extinction ratio for the electric field is $\approx\pi/(2F)$. The authors of [54] have demonstrated an intensity extinction ratio of 59 dB using a cavity with a finesse F=3825. According to (5.3), the extinction ratio should increase with finesse. The PNC experiment will employ a finesse value of several tens of thousands, which should yield a much higher extinction. We note that in the experiment described in [54], the polarization of the light incident to the cavity input coupler, is at 45^o with respect to the cavity plane, so that equal power is available to both the s and p modes. In our case, the incident polarization will be in the z-direction, therefore, a higher extinction than what was reported in [54] is expected. Assuming a Finesse of 50,000 can be achieved for the p mode of the 540 nm buildup cavity, and an alignment of the input polarization with the p mode at the 0.5% level, then the optimum extinction would be $\sim 1.6 \cdot 10^{-7}$. This would bring the M_1 term to within less than 1% of Im(E_{PNC}). Of course such polarization purity is yet to be demonstrated, and this will be one of the major challenges to overcome in the PNC experiment.

5.4 PNC experiment on the $6S_{1/2}$-$5D_{3/2}$ transition

So far, we have considered extending our technique to measurements of the PNC amplitude on the Cs $6S_{1/2} \rightarrow 7S_{1/2}$ transition. An interesting alternative to this appears to be the electric-dipole forbidden $6S_{1/2} \rightarrow 5D_{3/2}$ transition in the same system. Calculations of the PNC amplitude [55,56] yield a size ~ 4 times larger than that of the 6S→7S transition. A 4 times increase in the signal to noise ratio, corresponds to a 16 times decrease in the amount of integration time required to obtain a particular accuracy, compared to the 6S→7S state. For an experiment that requires very long

integration times, this is a major factor. Since the experiment measures the ratio of the PNC to a Stark-induced amplitude, the larger PNC amplitude makes the measurement less susceptible to stray fields. Finally, a measurement of the PNC effect on a transition other than the 6S→7S employed in the very successful Boulder experiment will provide a more reliable check of the Boulder results.

The one-photon interactions contributing to the $6S_{1/2}\rightarrow 5D_{3/2}$ transition, aside from the PNC, is the Stark-induced transition (E_{St}) and an allowed electric-quadrupole transition (E_2). Figure 5.2 shows a relevant energy level diagram with all the transitions contributing to the 6S→5D transition. Unlike the 6S→7S case, there is no M_1 contribution for excitation to the $5D_{3/2}$ state. This is an important difference, because a significant systematic contribution in the 6S→7S experiment is not present here. However, as discussed in A.D. Cronin's thesis [57], the size of the E_2 amplitude in the 6S→5D is 1000 times larger than that of the M_1 in the 6S→7S transition. Fortunately the E_2 transition does not contribute to $\Delta m_F=0$ transitions. Cronin proposes a PNC measurement based the Stark-PNC interference technique (also employed in the Boulder experiment), using the $\Delta F=1$, $\Delta m_F=0$ $6S_{1/2}$ F=4, $m_F=4 \rightarrow 5D_{3/2}$ F=5, $m_F=4$ transition, in the presence of a 74 G magnetic field. The magnetic field splits the various m_F levels enough so that the $E_{St}\cdot E_2$ interference from $\Delta m_F=+/-1$ transitions is largely attenuated (both the E_{st} and E_2 contribute for $\Delta m_F=+/-1$).

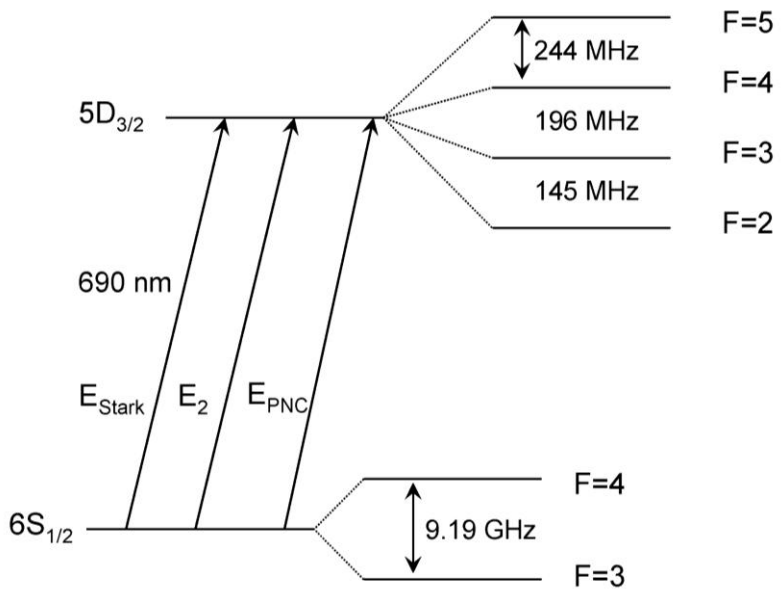

Figure 5.2: Partial energy level showing the hyperfine structure of the $6S_{1/2}$ and $5D_{3/2}$ states, and the possible one-photon transition pathways between these states.

Compared to the Stark-PNC scheme, our Coherent Control scheme offers the advantage that the strong (two-photon) transition is (or can be made to be) active only for $\Delta m_F=0$ transitions [37]. The $\Delta m_F=0$ transition is the only type allowed if the two fields driving the transition are degenerate. In the non-degenerate case, with appropriate selection of the two field polarizations, we can induce $\Delta m_F=0$ transitions and suppress the $\Delta m_F=+/-$ 1 contributions. Therefore, the $A_{2P}\cdot E_2$ interference can be suppressed without the need for a strong magnetic field, that can cause issues through Zeeman mixing of the closely spaced F components the $5D_{3/2}$ state. Potential $A_{2P}\cdot E_2$ contributions could only arise from a misalignment of the magnetic field in the interaction region with the coordinate system, or through stray fields present in the region.

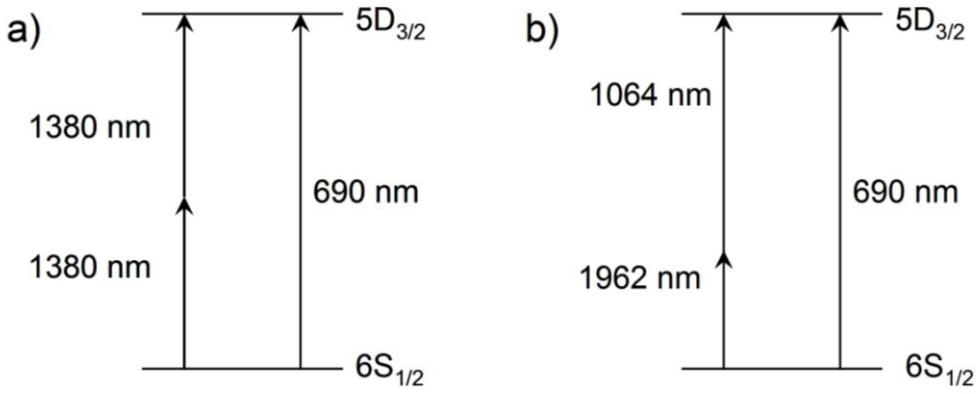

Figure 5.3: Two-pathway excitation of the $6S_{1/2}\rightarrow 5D_{3/2}$ transition, using a) degenerate frequencies to drive the two-photon pathway, b) non-degenerate frequencies.

We show in Figure 5.3 two possible schemes for the two-pathway excitation of the $6S_{1/2}\rightarrow 5D_{3/2}$ transitions. a) is a two-color experiment employing a single IR field at 1380 nm to drive the two-photon pathway. The 690 nm field required for the one-photon transitions can be generated by frequency doubling of the fundamental. Currently, the available sources at 1380 nm do not meet our power requirements for frequency doubling and driving the two-photon transition, since the existing amplifier technology in the 1300-1400 nm region can only offer powers at the 100 mW level. We would need a power of at least a few Watts, to obtain appreciable second harmonic power at 690 nm and a decent two-photon signal from our atom beam. Figure 5.3 b) shows an alternative, three-color scheme, with two non-degenerate IR

fields to drive the two-photon transition. One is at 1064 nm, a wavelength covered by our 12 W fiber amplifier used in the M_1 experiment. The second is at 1962 nm, within the range of available high power 1.9-2.0 μm amplifiers. In the three-color experiment, the 690 nm light can be produced by sum-frequency generation of the two IR fields. In order to select the $\Delta m_F=0$ transitions, the two-field polarizations would need to be parallel.

LIST OF REFERENCES

LIST OF REFERENCES

1. M. Gunawardena and D.S. Elliott, Atomic homodyne detection of weak atomic transitions, Phys. Rev. Lett. 98, 043001 (2007).
2. M. Gunawardena and D.S. Elliott, Weak signal detection using Coherent Control, Phys. Rev. A 76, 033412 (2007).
3. J.S.M. Ginges and V.V. Flambaum, Violations of fundamental symmetries in atoms and tests of unification theories of elementary particles, Physics Reports 397, 63–154, (2004).
4. W. C. Haxton and C. E.Wieman, Atomic Parity Non Conservation and nuclear anapole moments, Annual Review of Nuclear and Particle Science 51:261–93, (2001).
5. C.S. Wood S.C. Bennett, D. Cho, B.P. Masterson, J.L. Roberts, C.E. Tanner, C.E. Wieman, Measurement of Parity Nonconservation and an Anapole Moment in Cesium, Science 275, 1759 (1997).
6. P.A. Vetter, D.M. Meekhof, P.K. Majumber, S.K. Lamoreaux, , E.N. Fortson, Precise test of electroweak theory from a new measurement of parity nonconservation in atomic Thallium, Phys. Rev. Lett. 74, 2658 (1995).
7. M. J. D. Macpherson, K. P. Zetie, R. B. Warrington, D. N. Stacey, and J. P. Hoare, Precise measurement of parity nonconserving optical rotation at 876 nm in atomic bismuth**,** Phys. Rev. Lett. 67, 2784, (1991).
8. D.M. Meekhof, P. Vetter, P.K. Majumber, S.K. Lamoreaux, E.N. Fortson, High-precision measurement of parity nonconserving optical rotation in atomic lead, Phys. Rev. Lett. 71, 3442 (1993).
9. S.J. Phipp, N.H. Edwards, P.E.G. Baird, S. Nakayama, A measurement of parity non-conserving optical rotation in atomic lead, J. Phys. B 29, 1861, (1996).
10. N.H. Edwards, S.J. Phipp, P.E.G. Baird, S. Nakayama, Precise Measurement of Parity Nonconserving Optical Rotation in Atomic Thallium, Phys. Rev. Lett. 74, 2654 (1995).

11. M.C. Nocker, B.P. Masterson and C.E. Wieman, Precision measurement of Parity non Conservation in Cesium: A low energy test of the Electroweak Theory, Phys. Rev. Lett. 61, 310 (1988).
12. S.L. Zhu, C. M. Maekawa, B. R. Holstein, M. J. Ramsey-Musolf, U. van Kolck, Nuclear parity violation in Effective Field theory, Nuclear Physics A 748, 435-498 (2005)
13. S. G. Porsev, K. Beloy and A. Derevianko, Precision determination of electroweak coupling from atomic parity violation and implications for particle physics, Phys. Rev. Lett. 102, 181601 (2009).
14. Ce Chen, Y. Y. Yin and D. S. Elliott, Interference between optical transitions, Phys. Rev. Lett. 64, (1990)
15. P. Brumer and M. Shapiro, Control of unimolecular reactions using coherent light, Chemical Physics Letters, 126, Issue 6, 541–546,(1986).
16. M.A. Bouchiat, J. Guena and L. Pottier, Absolute polarization measurements and natural lifetime in the $7S_{1/2}$ state of Cs, J. Physique Lett. 45, 523-532 (1984).
17. S. L. Gilbert and C. E. Wieman, Atomic beam measurement of parity non-conservation in cesium, Phys. Rev. A 34, 792- 803 (1986).
18. C.S. Wood, Ph.D. thesis, High precision atomic parity nonconservation measurement using a spin polarized cesium beam and the nuclear anapole moment of ^{133}Cs, University of Colorado (1996).
19. M. A. Bouchiat and C. Bouchiat, Parity violation induced by weak neutral currents in atomic physics. part II, Journal de Physique 36, 493-509 (1975).
20. D. Cho, C. S. Wood, S. C. Bennett, J. L. Roberts, and C. E. Wieman, Precision measurement of the ratio of scalar to tensor transition polarizabilities for the cesium 6*S*-7*S* transition, Phys. Rev. A 55, 1007 (1997).
21. A. A. Vasilyev, I. M. Savukov, M. S. Safronova, and H.G. Berry, Measurement of the 6*s*-7*p* transition probabilities in atomic cesium and a revised value for the weak charge Q_W , Phys. Rev. A 66, 020101 (2002).
22. V. A. Dzuba, V. V. Flambaum, and J. S. M. Ginges, High-precision calculation of parity nonconservation in cesium and test of the standard model, Phys. Rev. D 66, 076013 (2002)

23. S. C. Bennett and C. E. Wieman, Measurement of the 6*S*→7*S* Transition Polarizability in Atomic Cesium and an Improved Test of the Standard Model, Phys. Rev. Lett. 82, 2484 (1999).
24. V. V. Flambaum, I. B. Khriplovich, and O. P. Sushkov, Nature of strongly forbidden M1-transitions and of g-factor anomalies in heavy atoms, Phys. Lett. 67A, 177 (1978).
25. V. A. Dzuba, V. V. Flambaum, P. G. Silvestrov and O.P. Sushkov, G-factor anomalies in heavy atoms, Physica Scripta 31, 275 (1985).
26. I. M. Savukov, A. Derevianko, H. G. Berry, and W. R.Johnson, Large Contributions of Negative-Energy States to Forbidden Magnetic-Dipole Transition Amplitudes in Alkali-Metal Atoms, Phys. Rev. Lett. 83, 2914-2918 (1999).
27. M. A. Bouchiat and L. Pottier, J. de Phys. 37, L-79 (1976).
28. S. L. Gilbert, R. N. Watts, and C. E. Wieman, Measurement of the 6*S*→7*S M*1 transition in cesium with the use of crossed electric and magnetic fields, Phys. Rev. A 29, 137 (1984).
29. M. A. Bouchiat, J. Guena and L. Pottier, J. Physique Lettres 45, L61-L67 (1984).
30. J. Hoffnagle, L. Ph. Roesch, V. L. Telegdi, A. Weis, and A. Zehnder, Measurement of the forbidden 6S → 7S transition in cesium with and without an electric field, Phys. Lett. 85A, 143-147 (1981).
31. C. Bouchiat and C. A. Piketty, J. Phys. (France) 49, 1851 (1988).
32. A. Derevianko, M. S. Safronova, and W. R. Johnson, Ab initio calculations of off-diagonal hyperfine interaction in cesium, Phys. Rev. A 60, 1741, (1999).
33. V. A. Dzuba and V. V. Flambaum, Off-diagonal hyperfine interaction and parity nonconservation in cesium, Phys. Rev. A 62, 052101, (1999).
34. M.A. Bouchiat and J. Guena, The E2 6S-7S amplitude in Cesium and its importance in a precise calibration of Epv1, J. Physique France 49, 2037 (1988).
35. B. Cagnac, G. Grynberg, and F. Biraben, J. Phys. (Paris) 34, 345 (1973).
36. G. Grynberg and B. Cagnac, Rep. Prog. Phys. 40, 791, (1977).
37. K. D. Bonin and T. J. McIlrath, Two-photon electric-dipole selection rules, J. Opt. Soc. Am. B 1, 52 (1984).
38. Carl Wieman and Leo Hollberg, Using diode lasers for atomic physics, Rev. Sci. Instrum. 62, 1 , (1991).

39. K.B. MacAdam, A. Steinbach, and C. Weinman, A narrow-band tunable diode laser system with grating feedback, and a saturated absorption spectrometer for Cs and Rb, Am. J. Phys. 60, 1098 (1992).
40. B. Dahmani, L. Hollberg, and R. Drullinger, Frequency stabilization of semiconductor lasers by resonant optical feedback, Optics Letters 12, 876 (1987).
41. G.C. Bjorklund, M.D. Levenson, W. Length and C. Ortiz, Frequency Modulation (FM) Spectroscopy, Appl. Phys. B 32, 145 (1983).
42. Huanqian Loh, Yu-Ju Lin, Igor Teper, Marko Cetina, Jonathan Simon, James K. Thompson, and Vladan Vuletic, Influence of grating parameters on the linewidths of external-cavity diode lasers, Applied Optics 45, 9191 (2006).
43. G.D. Boyd and D.A. Kleinman, Parametric interactions of focused Gaussian beams, J. Appl. Phys. 39, 3597 (1968)
44. Amnon Yariv, Pochi Yeh, Photonics, (Oxford University Press, 2007)
45. V. Gerginov, C. E. Tanner, Fluorescence of a highly collimated atomic cesium beam: theory and experiment, Optics Communications 222, 17, (2003)
46. B.P. Masterson, C. Tanner, H. Patrick and C.E. Wieman, High-brightness, high-purity spin-polarized cesium beam, Phys. Rev. A 47, 2139 (1993).
47. K. Tsigutkin, D. Dounas-Frazer, A. Family, J. E. Stalnaker, V. V. Yashchuk, and D. Budker, Parity violation in atomic ytterbium: Experimental sensitivity and systematics, Phys. Rev. A 47, 032114 (2010).
48. M. Gunawardena, PhD thesis, Homodyne detection of weak atomic transitions, Purdue University (2006)
49. S.L. Gilbert, M.C. Noecker, R.N. Watts, and C.E. Wieman, Measurement of Parity Non Conservation in Atomic Cesium, Phys. Rev. Lett., 55, 2680, (1985)
50. K. Tsigutkin, D. Dounas-Frazer, A. Family, J. E. Stalnaker, V.V. Yashchuk, and D. Budker, Observation of a Large Atomic Parity Violation Effect in Ytterbium, Phys. Rev. Lett. 103, 071601, (2009)
51. Stephen C. Bennett, Ph.D. thesis, High-precision measurements in atomic cesium supporting a low-energy test of the Standard Model, University of Colorado (1998).
52. Kenji Hisadome and Masami Kihara, An atomic beam collimator for Cs beam frequency standards, Jpn. J. Appl. Phys. 31, 1232, (1992)

53. Richard W. Fox, Chris W. Oates, Leo W. Hollberg, Stabilizing diode lasers to high-finesse cavities, Experimental methods in the Physical Sciences 40, (Elsevier Science (USA))

54. Shailendhar Saraf, Robert L. Byer, and Peter J. King, High-extinction-ratio resonant cavity polarizer for quantum-optics measurements, Applied Optics 46, 3850, (2007)

55. V. A. Dzuba, V. V. Flambaum, and J. S. M. Ginges, Calculations of parity-nonconserving *s-d* amplitudes in Cs, Fr, Ba^+, and Ra^+, Phys. Rev. A, 062101, (2001)

56. V. A. Dzuba, V. V. Flambaum, and B. M. Roberts, Parity nonconservation in Ac III and Th IV as tests for new physics, arXiv:1304.7591 [physics.atom-ph]

57. Alexander D. Cronin, Ph.D. thesis, New techniques for measuring Atomic Parity Violation, University of Washington (1999)

VITA

VITA

Dionysios Antypas was born and raised in Kefalonia, Greece. He received his B.S. degree in Physics from the Aristotle University of Thessaloniki, Greece in 2005 and M.S. degree from Purdue University in 2008.